Study of a stroboscopic model of a quantum dot

Alireza Tajic

Study of a stroboscopic model of a quantum dot

PROEFSCHRIFT

ter verkrijging van
de graad van Doctor aan de Universiteit Leiden,
op gezag van de Rector Magnificus Dr. D. D. Breimer,
hoogleraar in de faculteit der Wiskunde en
Natuurwetenschappen en die der Geneeskunde,
volgens besluit van het College voor Promoties
te verdedigen op donderdag 12 mei 2005
te klokke 15.15 uur

door

Alireza Tajic

geboren te Tehran, Iran op 7 mei 1975

Promotiecommissie:

Promotor:	Prof. dr. C. W. J. Beenakker
Co-Promotor:	dr. J. Tworzydło (Universiteit van Warschau)
Referent:	dr. H. Schomerus (Max-Planck-Institut, Dresden)
Overige leden:	Prof. dr. P. H. Kes
	Prof. dr. J. M. van Ruitenbeek
	Prof. dr. ir. W. van Saarloos

Het onderzoek beschreven in dit proefschrift is onderdeel van het wetenschappelijke programma van de Stichting voor Fundamenteel Onderzoek der Materie (FOM) en de Nederlandse Organisatie voor Wetenschappelijk Onderzoek (NWO).

The research described in this thesis has been carried out as part of the scientific programme of the Foundation for Fundamental Research on Matter (FOM) and the Netherlands Organisation for Scientific Research (NWO).

To my parents

Contents

1 Introduction **1**
- 1.1 Classical chaos in billiards . . . 1
- 1.2 Quantum chaos in quantum dots . . . 7
- 1.3 Stroboscopic model of a closed quantum dot . . . 10
- 1.4 Stroboscopic model of an open quantum dot . . . 12
- 1.5 This thesis . . . 13

2 Dynamical model for the quantum-to-classical crossover of shot noise **23**
- 2.1 Introduction . . . 23
- 2.2 Description of the stroboscopic model . . . 24
  - 2.2.1 Closed system . . . 24
  - 2.2.2 Open system . . . 26
- 2.3 Quantum-to-classical crossover of shot noise . . . 27
  - 2.3.1 Quantum mechanical calculation . . . 27
  - 2.3.2 Semiclassical calculation . . . 30
  - 2.3.3 Scattering states in the lead . . . 32
- 2.4 Conclusion . . . 33
- 2.A Floquet matrix in coordinate representation . . . 33
- 2.B Derivation of Eq. (2.7) . . . 36
- 2.C Calculation of the band area distribution . . . 36

3 Quantum-to-classical crossover of mesoscopic conductance fluctuations **41**
- 3.1 Introduction . . . 41
- 3.2 Stroboscopic model . . . 42
- 3.3 Numerical results . . . 44
- 3.4 Interpretation . . . 45
- 3.5 Conclusions . . . 49

4 Weak localization of the open kicked rotator **53**
4.1 Introduction 53
4.2 Time-reversal-symmetry breaking in the open kicked rotator . . . 54
4.2.1 Formulation of the model 54
4.2.2 Three-kick representation 55
4.2.3 One-kick representation 57
4.2.4 Scattering matrix 58
4.3 Relation with random-matrix theory 58
4.4 Numerical results 62
4.5 Conclusions 65
4.A Derivation of the free propagator 67
4.B Classical map 68
4.B.1 Three-kick representation 69
4.B.2 One-kick representation 70
4.C Derivation of Eqs. (4.28) and (4.29) 70
4.D Semiclassical derivation of the weak localization peak 72

5 Exponential sensitivity to dephasing of electrical conduction through a quantum dot **77**

6 Momentum noise in a quantum point contact **87**

Samenvatting **99**

List of publications **101**

Curriculum Vitæ **103**

Chapter 1

Introduction

Mesoscopic systems are intermediate between the macroscopic world of classical mechanics and the microscopic world of quantum mechanics. These two worlds come together in the study of quantum chaos, which is the search for quantum mechanical signatures of classically chaotic dynamics. In this thesis we investigate the quantum-to-classical crossover in a class of chaotic systems called "quantum dots", using a numerical method called "stroboscopic". In the introduction we will explain what these words mean and give some background information.

1.1 Classical chaos in billiards

Chaos in classical mechanics refers to the sensitivity on initial conditions of the time dependence of a dynamical system. No matter how precisely you measure the initial conditions, your prediction of its subsequent motion goes radically wrong after a short time. Characteristically, the predictability horizon grows only logarithmically with the precision of measurement.

A dynamical system need not be complicated to exhibit chaotic dynamics. One of the simplest examples is the ballistic motion of a particle in a box. The two-dimensional version can be thought of as game of snooker (see Fig. 1.1). On a rectangular, pocketless table, the ball follows a trajectory that depends on its initial location and how it gets hit. If there is no friction, it continues bouncing around the table forever. After a slight change in the ball's starting position, a similar hit produces a similar trajectory. The square billiard exhibits linear divergence, which means that the distance that separates the two trajectories increases proportionally to the amount of time that passes. No shot on this table behaves chaotically. Now imagine adding another rail, a circular one placed right in the center of

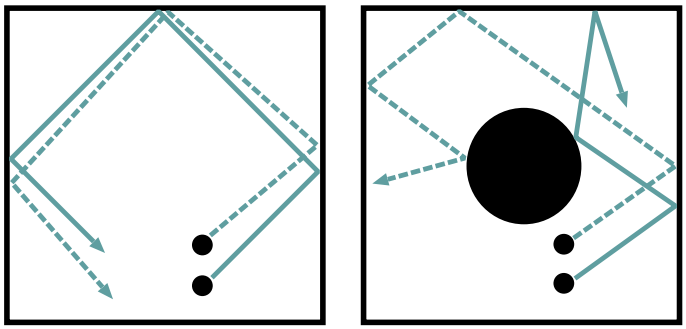

Figure 1.1: Two trajectories of a billiard ball launched with similar initial conditions. In the square billiard (left), these two trajectories do not diverge significantly. In contrast, the two trajectories rapidly diverge in the Sinai billiard (right).

the table. You now have what is called a Sinai billiard [1]. A first shot hits the round rail and then bounces back and forth between the side and center rails a few times. Again, displace the ball slightly from its original position. This time the second trajectory is entirely different from the first. The Sinai billiard exhibits exponential divergence; the two trajectories separate from one another exponentially fast.

The dynamics in a square billiard (with linear, or more generally, power law divergence) is called regular or integrable, while the dynamics in the Sinai billiard (with exponential divergence) is called chaotic [2–6]. In Fig. 1.2 we contrast three shapes of billiards that give rise to regular dynamics with three shapes in which the dynamics is chaotic. A regular billiard has a spatial symmetry that provides a second constant of the motion (in addition to the energy). Since there are two degrees of freedom as well, the dynamics is integrable. A chaotic billiard has no constant of the motion other than the energy.

In the chaotic case, the exponential divergence of initially nearby trajectories, $\Delta(t) = \Delta(0)\, e^{\lambda t}$, is measured by the Lyapunov exponent λ (see Fig. 1.3). Since the volume of a region in phase space (x, p) is conserved (Liouville's theorem), an exponential divergence $\propto e^{\lambda t}$ in one direction is compensated by an exponential convergence $\propto e^{-\lambda t}$ in the orthogonal direction. There is only a single exponent λ in a two-dimensional billiard, while in three dimensions there are two Lyapunov exponents λ_1, λ_2. (The number of independent positive Lyapunov exponents is one less than the number of dimensions, because the conserved energy fixes one exponent at zero.)

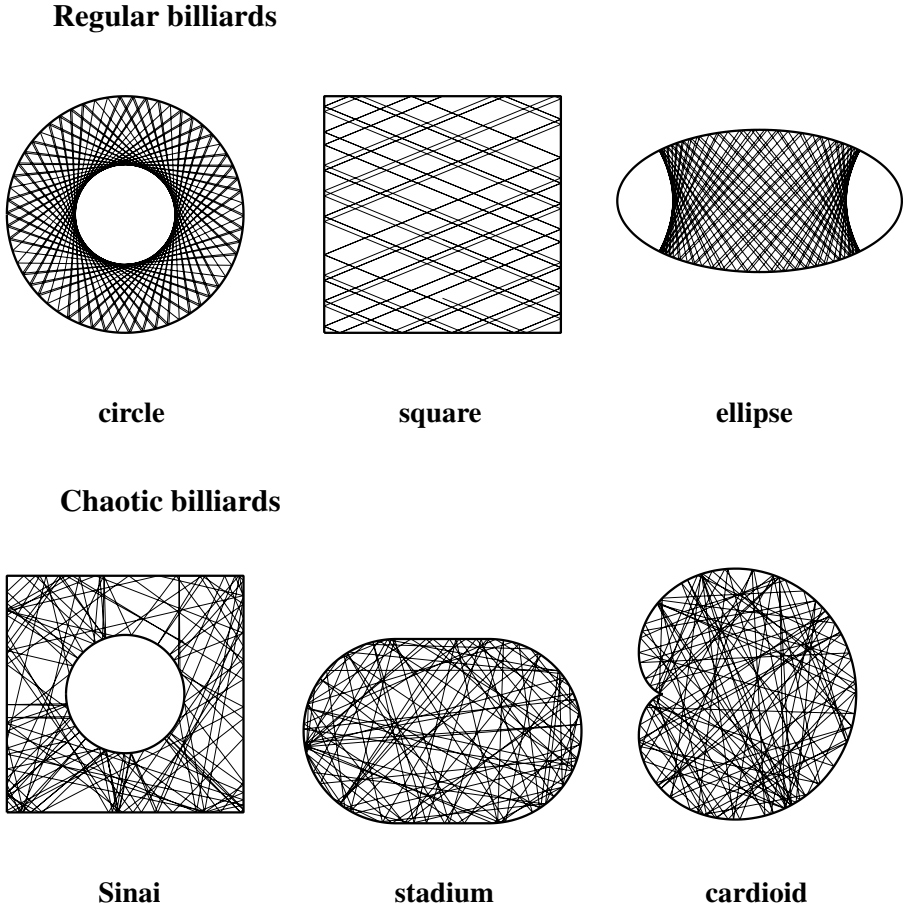

Figure 1.2: A single trajectory in regular and chaotic billiards. Adapted from Ref. [6]

Because it is difficult to visualize the four-dimensional phase space (x, y, p_x, p_y) of a billiard, it is convenient keep track only of the collisions with the boundaries. The trajectory can now be described by just two coordinates, the position $s \in (0, 1)$ along the boundary of the billiard (normalized by the total circumference) and the angle of incidence $\phi \in (-\pi/2, \pi/2)$. The section of phase space $(s, \sin\phi)$ is called the Poincaré surface of section. The map

$$F : (s, \sin\phi) \to (s', \sin\phi') \tag{1.1}$$

that relates subsequent collisions is called the Poincaré map. It is area preserving because of Liouville's theorem.

If the Poincaré map follows a smooth curve in the surface of section, then the system is integrable. If, on the other hand, the Poincaré map reveals an apparently random series of points, then the system is chaotic. Fig. 1.4 shows the Poincaré map of a billiard in which some initial conditions give rise to a regular dynamics and some to a chaotic dynamics. The surface of section shows islands of stability in a chaotic sea.

Maps have been studied independently of billiards as simple examples of nonlinear systems [3–5, 8, 9]. The iteration of a nonlinear map amounts to a stroboscopic description of the linear equations of motion. In the billiard the stroboscopic time interval varies from one collision to the next, but there still is a typical period τ_0 set by the typical linear dimension of the billiard. Ease of visualization is one advantage of the stroboscopic description. Also, the numerical computations can be much faster, since part of the dynamics is effectively done analytically in obtaining the map itself. What we lose is information on the dynamics in between collisions with the boundary, which is in general irrelevant on time scales $\gg \tau_0$.

Every area preserving map F can be associated with a time-dependent Hamiltonian $H(t)$. The stroboscopic period is determined by the periodicity $H(t) = H(t+\tau_0)$ of the Hamiltonian. The phase space of H is two-dimensional, but the dynamics is not integrable because energy is not a constant of the motion. For example, the so-called standard (Chirikov) map [8], transforms the canonically conjugate variables (θ, J) on a cylinder to (θ', J'), where

$$\theta' = \left[\theta + (\tau_0/I_0)J'\right] \quad \text{modulo } 2\pi \ , \tag{1.2a}$$

$$J' = J + (K I_0/\tau_0)\sin\theta \ . \tag{1.2b}$$

This area preserving map, describing a free angular rotation and a kick in momen-

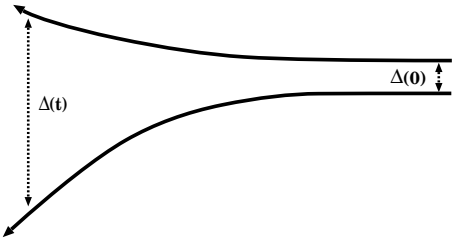

Figure 1.3: Exponential divergence of chaotic trajectories, $\Delta(t) = \Delta(0)e^{\lambda t}$, with a rate set by the Lyapunov exponent λ.

tum, is associated with the time-dependent Hamiltonian

$$H(t) = \frac{J^2}{2I_0} + \frac{K I_0}{\tau_0} \cos\theta \sum_{n=-\infty}^{\infty} \delta(t - n\tau_0) \,, \tag{1.3}$$

known as the kicked rotator. It describes a particle moving freely along a circle, with moment of inertia I_0, being subjected periodically (with period τ_0) to a kick whose strength depends on the angular coordinate θ and a fixed parameter K. By introducing the rescaled variables $x = \theta/2\pi$ and $p = J\tau_0/2\pi I_0$, we can write the dimensionless Hamiltonian

$$H = \frac{p^2}{2} + \frac{K}{(2\pi)^2} \cos(2\pi x) \sum_{n=-\infty}^{\infty} \delta(t - n) \,, \tag{1.4}$$

and its associated map

$$x_{n+1} = \left[x_n + p_{n+1}\right] \text{ modulo } 1 \,, \tag{1.5a}$$

$$p_{n+1} = p_n + \frac{K}{2\pi} \sin(2\pi x_n) \,. \tag{1.5b}$$

We denote by x_n the coordinate at the kick $t = n$ (measured in units of τ_0), and we denote the momentum just before and after the kick by p_n and p_{n+1}.

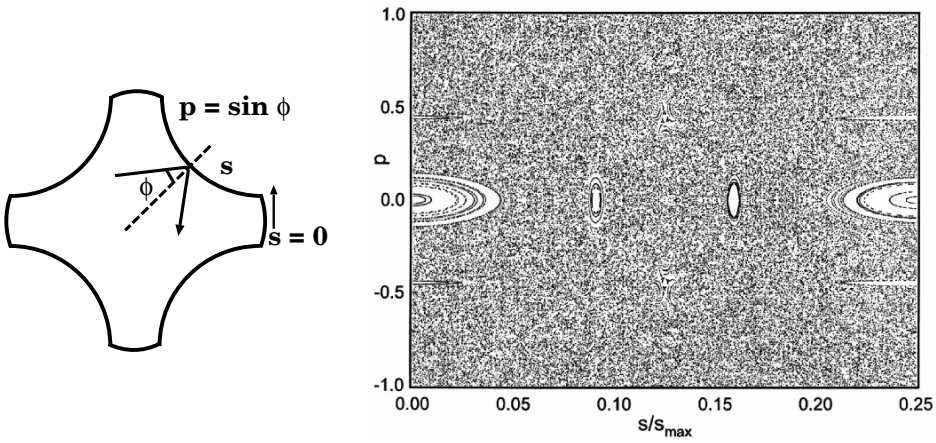

Figure 1.4: The clover geometry (left), an example of a billiard with a mixed regular and chaotic dynamics, as is clearly visible in the Poincaré map (right). After Brodier et al. [7]

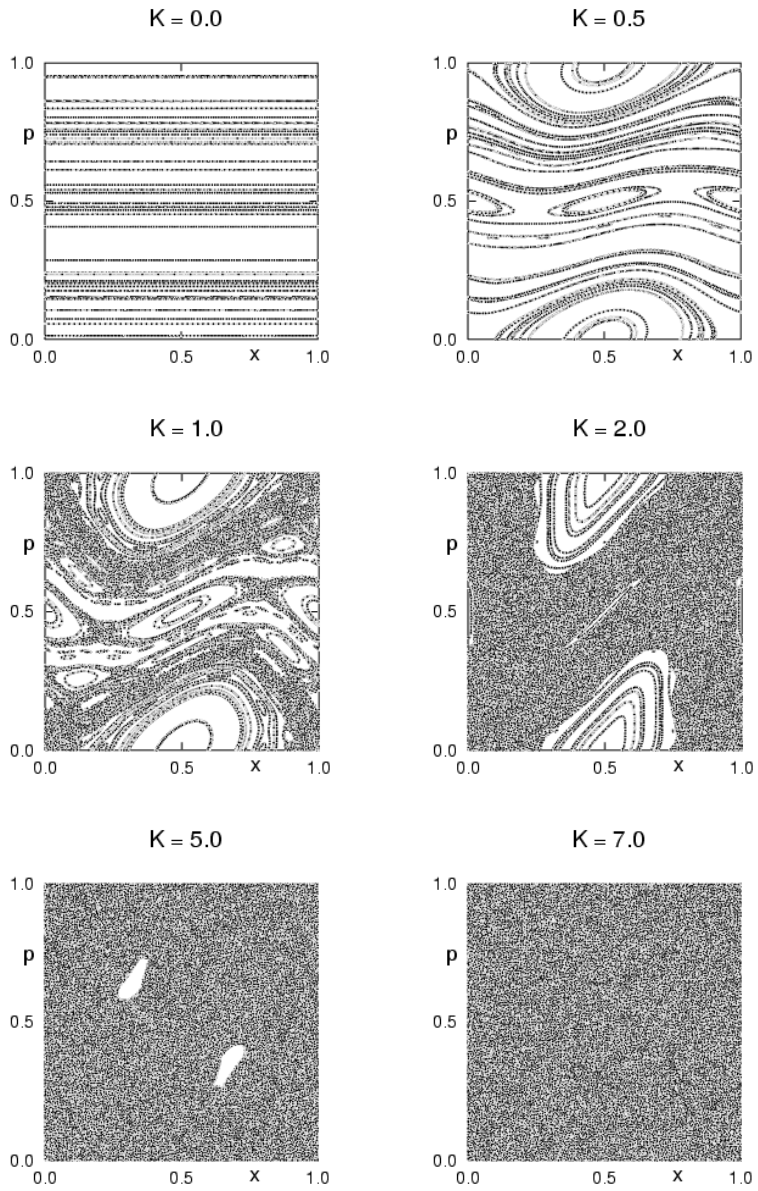

Figure 1.5: Poincaré surface of section of the standard (Chirikov) map (1.5). The dynamics crosses over from regular to mixed to fully chaotic with increasing kicking strength K.

The dynamics of this map takes place on the cylinder $0 < x < 1$, $-\infty < p < \infty$. For $K = 0$ the system is integrable and all trajectories lie on one-dimensional tori in phase space. For $K > 0$ the system undergoes a transition to chaos, in the way described by Kolmogorov, Arnold, and Moser (KAM) [8, 10–13]. For sufficiently small K, the Poincaré map follows simple smooth curves. As K increases, more and more of these curves disappear. At the golden number $K_g = (1 + \sqrt{5})/2 = 0.9716$ the last KAM curve becomes unstable and breaks up. The phase space for $K > K_g$ is not yet fully chaotic, some islands of stability remain. These disappear for $K > 5$, when the whole of phase space is characterized by the Lyapunov exponent $\lambda \approx \ln(K/2)$ [8]. In this regime, the momentum of a typical trajectory grows diffusively, with diffusion constant $D = \langle [p_n - p_0]^2 \rangle / n \approx K^2/8\pi^2$. Here n is measured in units of τ_0 and the average is over a distribution of initial conditions [3, 8, 14, 15]. Fig. 1.5 shows the iteration of the Chirikov map (1.5) for a small number of initial points. The map is periodic in x and p (with unit period), so only the torus $\{x, p \in [0, 1)\}$ is shown. One clearly sees how the system crosses over from the fully integrable regime to the fully chaotic regime as the kicking strength K increases.

1.2 Quantum chaos in quantum dots

Structures with a geometry similar to those shown in Figs. 1.1 and 1.2 can be fabricated in the two-dimensional electron gas (2DEG) which forms at the interface of a GaAs/AlGaAs heterostructure (see Fig. 1.6) [16, 17]. Such electron billiards have dimensions L of the order of $1 - 10\ \mu$m, while the Fermi wave length $\lambda_F \approx 60$ nm is much smaller than L. These are mesoscopic systems intermediate between the macroscopic world of classical mechanics and the microscopic world of quantum mechanics [18, 19].

An electron moving in a quantum dot obeys the Schrödinger wave equation, which approaches Newton's equation of particle motion in the limit that $\lambda_F/L \to 0$. This limit has been studied since the early days of quantum mechanics, mostly in integrable systems. The field of quantum chaos studies this limit in chaotic systems [20, 21].

An early result of the quantum-to-classical crossover, due to Ehrenfest [23], is that quantum mechanical expectation values of position and momentum follow Newton's equation of motion in the limit $h \to 0$ at fixed time interval. In the billiard the ratio $\lambda_F/L \equiv h_{\rm eff}$ is the effective Planck constant, which is experimentally tunable. If both the observation time t and $h_{\rm eff}^{-1}$ are sent to infinity, then Ehrenfest's correspondence principle breaks down unless $t < \tau_E(h_{\rm eff})$. The

Ehrenfest time τ_E goes itself to infinity when $h_{\rm eff} \to 0$, but it does so very slowly in a chaotic system [24],

$$\tau_E = \frac{1}{\lambda} \ln\left(h_{\rm eff}^{-1}\right) \ . \tag{1.6}$$

The argument leading to the Ehrenfest time (1.6) goes as follows (see Fig. 1.7). A wave packet with minimal uncertainty in both position and momentum has a width of order λ_F in real space. This initial width increases exponentially in time, $\Delta(t) = \lambda_F \ e^{\lambda t}$. The time τ_E is the time at which $\Delta(t) = L$. Thus, before the Ehrenfest time the wave packet can be well described by a particle trajectory,

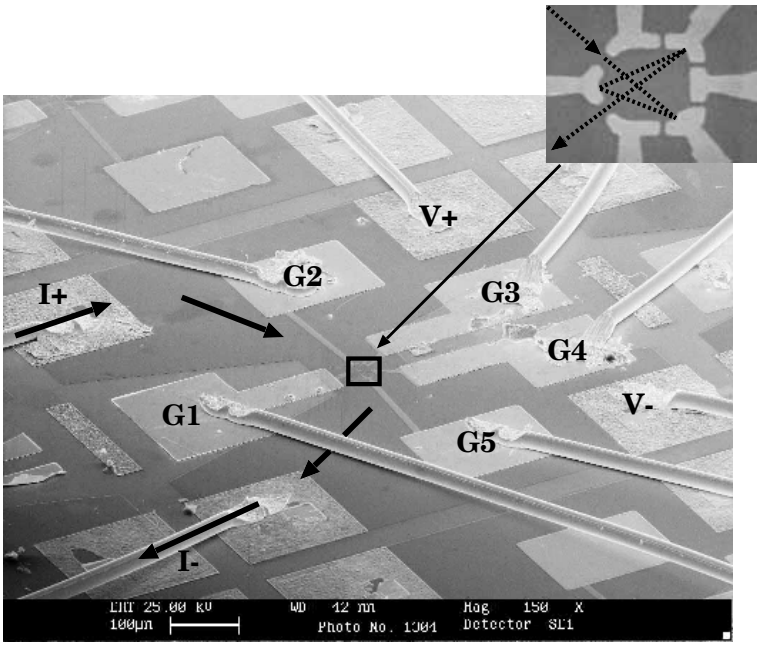

Figure 1.6: Perspective view of a quantum dot, fabricated in the 2DEG of a GaAs/AlGaAs heterostructure, with a blowup of the central region. The 2D electron gas lies 90 nm under the surface. The dot area is about 2 μm^2, and the Fermi wave length is about 60 nm. Electrons can enter and exit the quantum dot through point contacts. The elements labeled $G_1, G_2 \cdots, G_5$ are gate electrodes that can vary the shape of the billiard. A four-terminal resistance measurement at the contacts $V_\pm, I_\pm$ gives information on the transmission probability through the quantum dot. After Huibers [22].

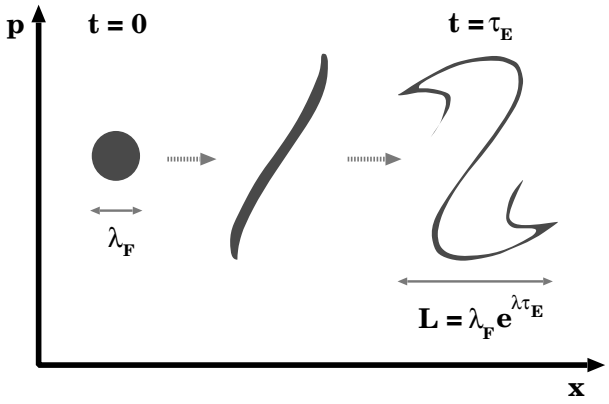

Figure 1.7: Schematic diagram of how a minimal uncertainty wave packet spreads over the whole phase space, while conserving its area.

whereas for times longer than τ_E the concept of a trajectory loses its meaning.

The phenomenology of electrical conduction through a quantum dot will thus be different in the two regimes $\tau_D \ll \tau_E$ and $\tau_D \gg \tau_E$, where τ_D is the mean dwell time of an electron inside the quantum dot. The time τ_D is independent of $h_{\rm eff}$, given by $\tau_D \simeq L^2/wv_F$ (with v_F the Fermi velocity and w the width of the openings through which an electron enters or leaves the quantum dot).

For $\tau_D \gg \tau_E$ quantum interference effects can be observed in the conductance of the quantum dot, such as weak localization and universal conductance fluctuations [18, 19]. These all require the splitting of wave packets into partial waves that then interfere constructively or destructively. The same splitting of wave packets leads to time-dependent current fluctuations (shot noise) [25]. Random-matrix theory (RMT) provides a universal theoretical description of these phenomena [26]. All of this will be modified in some way in the opposite regime $\tau_E \gg \tau_D$, when the wave packet no longer splits but stays together on a single trajectory.

To investigate the quantum-to-classical crossover when $L/\lambda_F \to \infty$, one can perform computer simulations. For such simulations one can choose two alternative approaches:

- One can solve numerically the Schrödinger equation in the particular geometry of a quantum billiard. This approach is appropriate for studying both the specific and generic properties of a quantum dot. Because it is restricted to small system sizes ($L/\lambda_F \lesssim 100 - 1000$), it is difficult to vary the Ehrenfest time $\tau_E \propto \ln(L/\lambda_F)$ by a substantial amount.

- One can quantize the stroboscopic map. Using this approach one loses information about specific characteristics of the quantum dot (pertaining to time scales below the time between subsequent collisions with the boundary). The computational efficiency of the map allows to study very big system sizes ($L/\lambda_F \sim 10^6$) and makes it possible to vary the logarithmic Ehrenfest time scale by an order of magnitude.

1.3 Stroboscopic model of a closed quantum dot

Quantization of the Chirikov standard map can be done by imposing the quantization rule

$$[\,\hat{x},\hat{p}\,] = i\hbar_{\rm eff} \tag{1.7}$$

on the Hamiltonian (1.4) of the kicked rotator. The effective Planck constant of the problem is $h_{\rm eff} = h\tau_0/(2\pi)^2 I_0 \equiv 2\pi\hbar_{\rm eff}$. The resulting quantum kicked rotator has Hamiltonian [20,21,27,28]

$$H = -\frac{\hbar_{\rm eff}^2}{2}\frac{\partial^2}{\partial x^2} + \frac{K}{(2\pi)^2}\cos(2\pi x)\sum_{n=-\infty}^{\infty}\delta(t-n)\,, \tag{1.8}$$

where t is measured in units of the stroboscopic time τ_0.

The wave function $\psi(t)$ at multiples of the stroboscopic time is given by $\psi(n) = \mathcal{F}^n\psi(0)$ in terms of the Floquet operator

$$\mathcal{F} = \left\{\exp\left[-\frac{i}{\hbar_{\rm eff}}\int_0^1 dt' H(t')\right]\right\}_+ . \tag{1.9}$$

Here $+$ denotes the positive time ordering. In the Heisenberg picture, the corresponding quantum map is defined as

$$\hat{x}(t+1) = \mathcal{F}^\dagger\hat{x}(t)\,\mathcal{F}\,, \tag{1.10a}$$

$$\hat{p}(t+1) = \mathcal{F}^\dagger\hat{p}(t)\,\mathcal{F}\,, \tag{1.10b}$$

where $\mathcal{F}^\dagger = \mathcal{F}^{-1}$ is the inverse of the unitary Floquet operator. The Floquet operator has orthonormal eigenvectors $|\mu\rangle$ and unimodular eigenvalues $\exp(-i\varepsilon_\mu)$,

$$\mathcal{F}|\mu\rangle = e^{-i\varepsilon_\mu}|\mu\rangle\,. \tag{1.11}$$

The real numbers ε_μ are called the quasienergies. In the Schrödinger picture, a wave function evolves as

$$\psi(x,t+n) = \sum_\mu e^{-in\varepsilon_\mu}\langle\mu|\psi(t)\rangle\,\langle x|\mu\rangle\,. \tag{1.12}$$

Because the interaction with the external force is instantaneous, one can factorize the total Floquet operator into the product of evolution operators corresponding to the free rotation and the interaction,

$$\mathcal{F} = B(\hat{x})\, G(\hat{p})\,, \tag{1.13a}$$

$$B(\hat{x}) = \exp\left(-\frac{i}{\hbar_{\rm eff}}\,\frac{K}{(2\pi)^2}\cos 2\pi\hat{x}\right)\,, \tag{1.13b}$$

$$G(\hat{p}) = \exp\left(-\frac{i}{\hbar_{\rm eff}}\,\frac{\hat{p}^2}{2}\right)\,. \tag{1.13c}$$

The periodicity of the angle variable gives rise to a discrete set of momentum eigenvalues defined by

$$\hat{p}\;|m\rangle = 2\pi\hbar_{\rm eff}\, m\;|m\rangle \qquad m = \pm 1, \pm 2, \cdots\,, \tag{1.14a}$$

$$\langle x|m\rangle = \exp(\, i 2\pi m x\,)\,. \tag{1.14b}$$

In the momentum representation, the free rotation operator G has a diagonal form with matrix elements

$$G_{mm'} = \exp\left(-i2\pi^2\hbar_{\rm eff} m^2\right)\delta_{mm'}\,. \tag{1.15}$$

In the same basis the matrix elements of the kick operator B are given in terms of a Bessel function,

$$B_{mm'} = i^{m-m'}\; J_{m-m'}\left(\frac{K}{(2\pi)^2\hbar_{\rm eff}}\right)\,. \tag{1.16}$$

The Bessel function decreases rapidly with increasing difference between indices and argument $\left(\,(2\pi)^2\hbar_{\rm eff}\,|m-m'| > K\,\right)$. It means that the unitary matrix $\mathcal{F}$ has the form of a band matrix [29,30] with negligible matrix elements outside a band of width $\approx K/2\pi^2\hbar_{\rm eff}$.

For a special choice of parameters $1/2\pi\hbar_{\rm eff} \equiv M$ an even integer, the Floquet operator reduces to an $M \times M$ unitary matrix. This choice is known as a resonance condition [27]. In this finite-dimensional space the basis states of position and momentum are the vectors $|x_n\rangle, |p_n\rangle, n = 0, 1, \cdots, M-1$. They obey

$$\hat{x}\;|x_n\rangle = (n/M)\;|x_n\rangle\,, \tag{1.17a}$$

$$\hat{p}\;|p_n\rangle = (n/M)\;|p_n\rangle\,, \tag{1.17b}$$

and are related by the discrete Fourier transform

$$\langle x_n|p_m\rangle = \frac{1}{\sqrt{M}}\;\exp\left[i\frac{2\pi}{M}\;mn\right]\,. \tag{1.18}$$

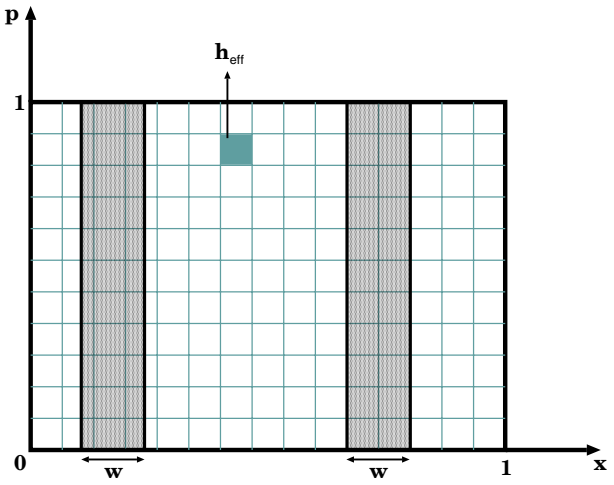

Figure 1.8: The phase space of unit area contains M Planck cells of area $h_{\rm eff}$. The connection to electron reservoirs is modeled by imposing absorbing boundary conditions inside two rectangular areas of width w, each containing N Planck cells.

The classical phase space consists of the torus $\{x \in (0,1), p \in (0,1)\}$, with periodic boundary conditions in the x and p directions. The number M is the number of Planck cells (of area $2\pi\hbar_{\rm eff}$) that are contained within the torus.

1.4 Stroboscopic model of an open quantum dot

So far we have discussed the stroboscopic description of a closed quantum dot. To study electrical conduction one needs to open it up and connect it to a pair of electron reservoirs.

The open kicked rotator was introduced in Refs. [31–33]. We impose absorbing boundary conditions inside a pair of rectangular areas in the phase space, which are assumed to be connected to electron reservoirs (see Fig. 1.8). If the particle enters one of these areas it is taken out of the system. We assume that the two absorbing regions contain a total of $2N$ Planck cells. The $2N \times 2N$ scattering matrix S of the open quantum dot is related to the $M \times M$ Floquet matrix of the closed dot by [31–33]

$$S = P\left[1 - \mathcal{F}\left(1 - P^{\rm T}P\right)\right]^{-1}\mathcal{F}\,P^{\rm T}\,. \tag{1.19}$$

The $2N \times M$ matrix P is the projection matrix which obeys

$$\left(P^{\mathrm{T}}P\right)_{nm} = \delta_{nm} \times \begin{cases} 1 & \text{if } L_1 \le n \le L_1 + N - 1, \\ 1 & \text{if } L_2 \le n \le L_2 + N - 1, \\ 0 & \text{otherwise,} \end{cases} \tag{1.20}$$

where L_1, L_2 denotes the left edge of the absorbing areas. The expression (1.19) can be easily understood if it is written out as a geometric series,

$$S = P\mathcal{F}P^{\mathrm{T}} + P\mathcal{F}Q\mathcal{F}P^{\mathrm{T}} + P(\mathcal{F}Q)^2\mathcal{F}P^{\mathrm{T}} + \cdots , \tag{1.21}$$

where $Q = 1 - P^{\mathrm{T}}P$ is the $M \times M$ matrix that projects onto the non-absorbing part of phase space. Each subsequent term in this series describes evolution over one more period τ_0. The evolution continues if the particle is not absorbed (Q) and stops if it is absorbed (P). One can verify that unitarity of $\mathcal{F}$ implies unitarity of S, as it should.

The scattering matrix (1.19) does not yet depend on the quasienergy. Such a dependence can be introduced by accounting for the phase shift $e^{i\varepsilon\tau_0}$ incurred during one stroboscopic period $\tau_0 \equiv 1$. Hence the energy dependent scattering matrix becomes

$$\begin{aligned} S(\varepsilon) &= Pe^{i\varepsilon}\mathcal{F}P^{\mathrm{T}} + Pe^{i\varepsilon}\mathcal{F}Qe^{i\varepsilon}\mathcal{F}P^{\mathrm{T}} + P(e^{i\varepsilon}\mathcal{F}Q)^2e^{i\varepsilon}\mathcal{F}P^{\mathrm{T}} + \cdots \\ &= P\frac{1}{1 - e^{i\varepsilon}\mathcal{F}\left(1 - P^{\mathrm{T}}P\right)}e^{i\varepsilon}\mathcal{F}P^{\mathrm{T}} . \end{aligned} \tag{1.22}$$

1.5 This thesis

Chapter 2: Quantum-to-classical crossover of shot noise

The current $I(t)$ flowing through a device exhibits fluctuations $\Delta I = I(t) - \bar{I}$ in time around the mean current $\bar{I}$. At zero temperature these fluctuations, known as shot noise, are caused by the discreteness of the electrical charge. If the current can be described by uncorrelated current pulses containing a single charge e, then the spectral density P_I of the current fluctuations has the Poissonian form $P_{\mathrm{Poisson}} = 2e\bar{I}$. Correlations imposed by fermionic statistics as well as by Coulomb interaction cause deviations of the shot noise from the Poisson value. These deviations are quantified by the Fano factor $F \equiv P_I / P_{\mathrm{Poisson}}$. In diffusive wires with non-interacting electrons $F = 1/3$, while in quantum dots $F = 1/4$ [34, 35]. These Fano factors are universal in the sense that they are independent of the details of the system.

Beenakker and van Houten predicted that shot noise in ballistic conductors should vanish when $L/\lambda_F \to \infty$, due to the crossover from stochastic quantum dynamics to deterministic classical dynamics [36]. The analytical calculation of Agam, Aleiner, and Larkin [37] led to the exponential suppression

$$F = \frac{1}{4}\exp\left(-\frac{\tau_E}{\tau_D}\right) . \tag{1.23}$$

This result was consistent with a recent experiment where the dwell time τ_D of an electron billiard created in a 2D electron gas was varied by changing the number of modes N transmitted through each of the two openings [38]. Since the Ehrenfest time τ_E depends only logarithmically on N, it remains approximately constant in the experiment.

A deficiency of the experiment, which is difficult to avoid, is that changing the width of the openings also changes the classical transport properties of the billiard. The contribution of relatively short, nonchaotic trajectories is reduced upon reducing N, and this modifies the Fano factor in a way that has nothing to do with the classical-to-quantum crossover. For a reliable test of the theory one would need to change all dimensions of the billiard relative to the wave length, not just the width of the openings. This is very problematic in an experiment, but is something that we can do easily in a computer simulation.

In this chapter we use the stroboscopic model to test the theoretical prediction (1.23), by increasing τ_E at constant τ_D. In this way all classical properties of the billiard remain unaffected and any variation in F must be of a quantum mechanical origin. We find that the simple exponential decay (1.23) is qualitatively correct but does not contain sufficient microscopic information to quantitatively describe our numerical data. A much better agreement is provided by the effective random-matrix theory of Ref. [39].

Chapter 3: Quantum-to-classical crossover of mesoscopic conductance fluctuations

We now turn from time dependent fluctuations to mesoscopic fluctuations, meaning fluctuations in the time-averaged current $\bar{I}$ from one sample to another sample of an ensemble of chaotic billiards. The quantity of interest is the variance Var G of the sample-to-sample conductance fluctuations. Random-matrix theory (RMT) [35, 40] predicts the universal values

$$\text{Var } G = \frac{1}{8\beta}\left(\frac{2e^2}{h}\right) , \tag{1.24}$$

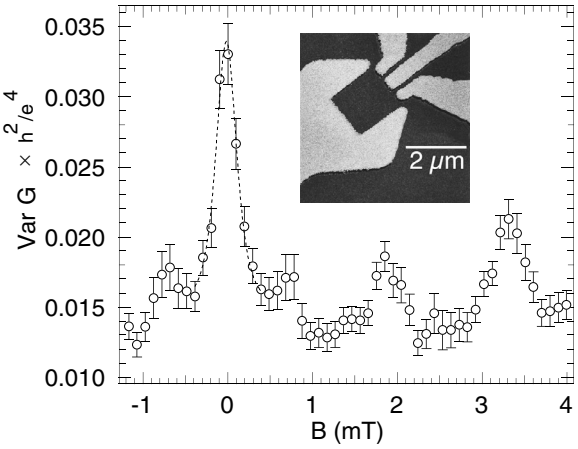

Figure 1.9: Variance of the conductance of a quantum dot as a function of magnetic field. The inset shows an electron micrograph of the device, fabricated in the two-dimensional electron gas of a GaAs/AlGaAs heterostructure. After Chan et al. [43].

where $\beta = 1(2)$ in the absence (presence) of a time-reversal symmetry-breaking magnetic field. This is the ballistic analogue of universal conductance fluctuations in disordered metals [41, 42].

Eq. (1.24) was observed in experiments by Chan et al. [43] (see Fig. 1.9) in which the shape-dependent fluctuations were measured as a function of magnetic field B. These experiments were in the regime $\tau_E \ll \tau_D$ in which no deviations from RMT are observed.

In our computer simulation we can access the regime of comparable τ_E and τ_D, to search for deviations from the RMT prediction (1.24). We find that such deviations are present if the ensemble is generated by varing the shape of the billiard or the positions of the leads, but we find no deviations if the ensemble is generated by varying the quasienergy. Jacquod and Sukhorukov [44] have explained this unexpected finding in terms of the effective random-matrix theory [39].

Chapter 4: Search for the τ_E dependence of weak localization

The argument of Jacquod and Sukhorukov implies not only that the conductance fluctuations as a function of energy or magnetic field should be τ_E-independent,

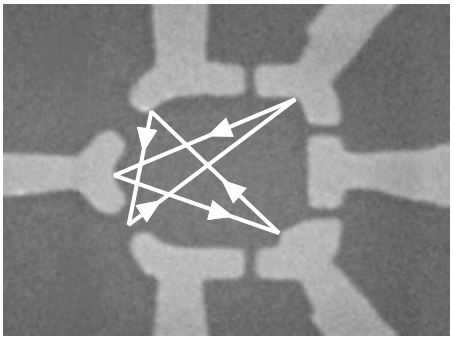

Figure 1.10: The reduced conductance in zero magnetic field is a result of the constructive interference of the closed trajectory shown with its time reversed partner. The picture of the device has been adapted from Ref. [22].

but also that other quantum interference effects should be τ_E-independent. This contradicts previous theories by Aleiner and Larkin [45] and Adagideli [46], which predicted a $\exp(-\tau_E/\tau_D)$ suppression of weak localization. In this chapter we will use the open kicked rotator to search numerically for the effect of increasing τ_E on weak localization.

Weak localization is the constructive interference of a pair of time-reversed trajectories. The resulting enhancement of the probability to return to the point of departure reduces the conductance, see Fig. 1.10. The reduced conductance disappears if a magnetic field breaks the time reversal symmetry. The prediction of RMT for the reduction δG of the conductance is [35, 40]

$$\delta G = -\frac{1}{4}\delta_{\beta,1}\left(\frac{2e^2}{h}\right) . \tag{1.25}$$

We have introduced a magnetic field into our model for the open kicked rotator, to search for the predicted $\exp(-\tau_E/\tau_D)$ suppression of the weak localization correction. No effect is found, in support of the effective random-matrix theory.

Chapter 5: Search for the τ_{E} dependence of dephasing

Our search for the Ehrenfest time dependence of quantum interference effects has so far been quite unsuccessful. No effect was found on the conductance fluctuations nor on the weak localization effect. In these studies we assumed full phase

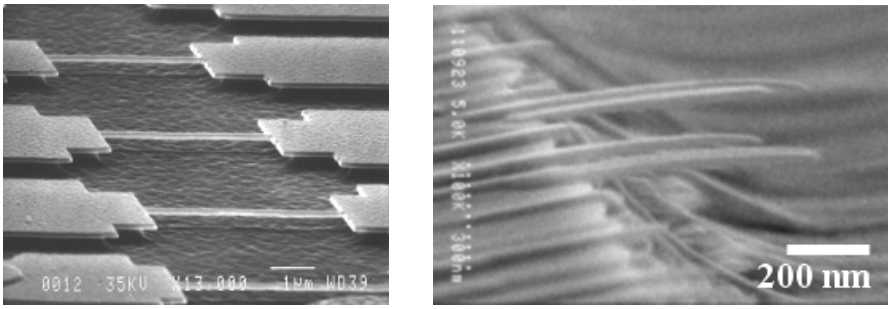

Figure 1.11: Series of doubly-clamped AlN beams, with lengths ranging from 3.9 to 5.6 μm and with widths ranging from 0.2 to 2.4 μm (left, adapted from Ref. [50]). Nanoscale InAs cantilevers (right, adapted from Ref. [51]).

coherence, as if the system was at zero temperature. In any realistic system there will be a finite dephasing time τ_ϕ.

According to random-matrix theory, interference effects in the conductance of a ballistic chaotic quantum dot should vanish $\propto (\tau_\phi/\tau_D)^p$ when the dephasing time τ_ϕ becomes small compared to the mean dwell time τ_D. Aleiner and Larkin have predicted that the power law crosses over to an exponential suppression $\propto \exp(-\tau_E/\tau_\phi)$ when τ_ϕ drops below the Ehrenfest time τ_E [45].

This chapter addresses the first observation of this crossover in a computer simulation of universal conductance fluctuations. As discussed in chapter 3 their theory also predicts an exponential suppression $\propto \exp(-\tau_E/\tau_D)$ in the absence of dephasing — which is *not* observed. We show that the effective random-matrix theory proposed previously for quantum dots without dephasing [39] can be extended to explain both observations.

Chapter 6: Momentum noise in a quantum point contact

This chapter falls outside of the main theme of this thesis. It addresses a topic in nanoelectromechanics, which is the study of the interplay of electrical and mechanical properties of mesoscopic systems [47, 48].

Mechanically suspended beams incorporating a two-dimensional electron gas, either in the form of a cantilever or a doubly-clamped beam (see Fig. 1.11), form a basic element in nanomechanical structures. The vibration is excited by the current because electrons transfer momentum to the lattice via elastic collisions with impurities and boundaries and thereby exert a fluctuating force on the lattice.

This fluctuating electromechanical force can be distinguished from thermal noise because of the linear dependence of the mean squared fluctuation on the applied voltage [49].

This chapter is devoted to an investigating of the electromechanical force in ballistic transport, where electrons collide with boundaries but not with impurities. We study the excitation of the transverse and longitudinal oscillator modes in a quantum point contact, which is a narrow constriction between two wide electron reservoirs. The conductance of the constriction is quantized in units of $2e^2/h$ [52]. While the electrical noise vanishes on the plateaus of quantized conductance, the force noise does not. We identify a regime in which the force noise has a stepwise increase as a function of the width of the constriction, similar to the conductance.

Bibliography

[1] Y. G. Sinai, Russian Mathematical Surveys **25**, 137 (1970).

[2] H. Goldstein, *Classical Mechanics* (Addison-Wesley, Massachusetts, 1980).

[3] A. J. Lichtenberg and M. A. Lieberman, *Regular and Chaotic Dynamics* (Springer, New York, 1983).

[4] M. Tabor, *Chaos and Integrability in Nonlinear Dynamics: An Introduction* (Wiley, New York, 1989).

[5] E. Ott, *Chaos in Dynamical Systems* (Cambridge University Press, Cambridge, 1993).

[6] A. Bäcker, in *Mathematical Aspects of Quantum Maps*, edited by M. Degli Esposti and S. Graffi, Springer Lecture Notes in Physics, volume 618 (Springer, New York, 2003).

[7] O. Brodier, T. Neicu, and A. Kudrolli, Eur. Phys. J. B **23**, 365 (2001).

[8] B. V. Chirikov, Phys. Rep. **52**, 263 (1979).

[9] J. M. Greene, J. Math. Phys. **20**, 1183 (1979).

[10] J. D. Meiss, Rev. Mod. Phys. **64**, 795 (1992).

[11] A. N. Kolmogorov, Dokl. Akad. Nauk SSSR **98**, 527 (1954).

[12] V. I. Arnold, Usp. Mat. Nauk **18**, No. 6, 91 (1963).

[13] J. Moser, Nachr. Akad. Wiss. Göttingen, Math. Phys. Kl.1 (1962).

[14] A. B. Rechester and R. B. White, Phys. Rev. Lett. **44**, 1586 (1980).

[15] E. Doron and S. Fishman, Phys. Rev. Lett. **60**, 867 (1988).

[16] L. P. Kouwenhoven, C. M. Marcus, P. L. McEuen, S. Tarucha, R. M. Westervelt, and N. S. Wingreen, in *Mesoscopic Electron Transport*, edited by L. L. Sohn, L. P. Kouwenhoven, and G. Schön, NATO Science Series E345, (Kluwer, Dordrecht, 1997).

[17] Y. Alhassid, Rev. Mod. Phys. **72**, 895 (2000).

[18] Y. Imry, *Introduction to Mesoscopic Physics* (Oxford University Press, Oxford, 1998).

[19] S. Datta, *Electronic Transport in Mesoscopic Systems* (Cambridge University Press, Cambridge, 1995).

[20] F. Haake, *Quantum Signatures of Chaos* (Springer, Berlin, 2001).

[21] H. -J. Stöckmann, *Quantum Chaos, An Introduction* (Cambridge University Press, Cambridge 1999).

[22] A. Huibers, Ph.D. Thesis (Stanford University, 1999).

[23] P. Ehrenfest, Z. Phys. **45**, 455 (1927).

[24] G. P. Berman and G. M. Zaslavsky, Physica A **91**, 450 (1978).

[25] Ya. M. Blanter and M. Büttiker, Phys. Rep. **336**, 1 (2000).

[26] C. W. J. Beenakker, Rev. Mod. Phys. **69**, 731 (1997).

[27] F. M. Izrailev, Phys. Rep. **196**, 299 (1990).

[28] L. E. Reichl, *The Transition to Chaos* (Springer, New York, 1992).

[29] G. Casati, B. V. Chirikov, I. Guarneri, and F. M. Izrailev, Phys. Rev. E **48**, 1613 (1993).

[30] F. M. Izrailev, T. Kottos, A. Politi, and G. P. Tsironis, Phys. Rev. E **55**, 4951 (1997).

[31] Y. V. Fyodorov and H.-J. Sommers, JETP Lett. **72**, 422 (2000).

[32] A. Ossipov, T. Kottos, and T. Geisel, Phys. Rev. E **65**, 055209 (2002).

[33] T. Kottos, A. Ossipov, and T. Geisel, Phys. Rev. E **68**, 066215 (2003).

[34] C. W. J. Beenakker and M. Büttiker, Phys. Rev. B **46**, 1889 (1992).

[35] R. A. Jalabert, J.-L. Pichard, and C. W. J. Beenakker, Europhys. Lett. **27**, 255 (1994).

[36] C. W. J. Beenakker and H. van Houten, Phys. Rev. B **43**, 12066 (1991).

[37] O. Agam, I. Aleiner, and A. Larkin, Phys. Rev. Lett. **85**, 3153 (2000).

[38] S. Oberholzer, E. V. Sukhorukov, and C. Schönenberger, Nature **415**, 765 (2002).

[39] P. G. Silvestrov, M. C. Goorden, and C. W. J. Beenakker, Phys. Rev. B **67**, 241301(R) (2003).

[40] H. U. Baranger and P. A. Mello, Phys. Rev. Lett. **73**, 142 (1994).

[41] B. L. Altshuler, JETP Lett. **41**, 648 (1985).

[42] P. A. Lee and A. D. Stone, Phys. Rev. Lett. **55**, 1622 (1985).

[43] I. H. Chan, R. M. Clarke, C. M. Marcus, K. Campman, and A. C. Gossard, Phys. Rev. Lett. **74**, 3876 (1995).

[44] Ph. Jacquod and E. V. Sukhorukov, Phys. Rev. Lett. **92**, 116801 (2004).

[45] I. L. Aleiner and A. I. Larkin, Phys. Rev. B **54**, 14423 (1996).

[46] I. Adagideli, Phys. Rev. B **68**, 233308 (2003).

[47] H. G. Craighead, Science **290**, 1532 (2000).

[48] M. L. Roukes, Phys. World **14**, 25 (2001).

[49] A. V. Shytov, L. S. Levitov, and C. W. J. Beenakker, Phys. Rev. Lett. **88**, 228303 (2002).

[50] J. S. Aldridge, R. S. Knobel, D. R. Schmidt, C. S. Yung and A. N. Cleland, in *SPIE Proceedings* **4591**, 11 (2001).

[51] H. Yamaguchi and Y. Hirayama, Appl. Phys. Lett. **80**, 4428 (2002).

[52] C. W. J. Beenakker and H. van Houten, Solid State Phys. **44**, 1 (1991).

Chapter 2

Dynamical model for the quantum-to-classical crossover of shot noise

2.1 Introduction

The problem of a quantum-to-classical crossover has been hotly debated since the early days of quantum mechanics. The recent progress in mesoscopic structures allows to address those issues in experimental context for actually available devices. The quantity of central interest is the shot noise.

Noise plays a uniquely informative role in connection with the particle-wave duality [1]. This has been appreciated for light since Einstein's theory of photon noise. Recent theoretical [2–6] and experimental [7] work has used electronic shot noise in quantum dots to explore the crossover from particle to wave dynamics. Particle dynamics is deterministic and noiseless, while wave dynamics is stochastic and noisy [8].

The crossover is governed by the ratio of two time scales, one classical and one quantum. The classical time is the mean dwell time τ_D of the electron in the quantum dot. In an open chaotic dot with two openings of width w, different scattering trajectories have in general different dwell times which are exponentially distributed $P(t) = \exp(-t/\tau_D)/\tau_D$, with the mean dwell time $\tau_D = 1/(2w)$. The quantum time is the Ehrenfest time τ_E, which is the time it takes a wave packet of minimal size to spread over the entire system. While τ_D is independent of $\hbar$, the time τ_E increases $\propto \ln(1/\hbar)$ for chaotic dynamics. An exponential suppression $\propto \exp(-\tau_E/\tau_D)$ of the shot noise power in the classical limit $\hbar \to 0$ (or equivalently, in the limit system-size-over-wave-length to infinity) was predicted by Agam, Aleiner, and Larkin [2]. A recent experiment by Oberholzer, Sukhorukov,

and Schönenberger [7] fits this exponential function. However, the accuracy and range of the experimental data is not sufficient to distinguish this prediction from competing theories (notably the rational function predicted by Sukhorukov [9] for short-range impurity scattering).

Computer simulations would be an obvious way to test the theory in a controlled model (where one can be certain that there is no weak impurity scattering to complicate the interpretation). However, the exceedingly slow (logarithmic) growth of τ_E with the ratio of system size over wave length has so far prevented a numerical test. Motivated by a recent successful computer simulation of the Ehrenfest-time dependent excitation gap in the superconducting proximity effect [10], we use the same model of the open kicked rotator to search for the Ehrenfest-time dependence of the shot noise.

2.2 Description of the stroboscopic model

The reasoning behind this model is as follows. The physical system we seek to describe is a ballistic (clean) quantum dot in a two-dimensional electron gas, connected by two ballistic leads to electron reservoirs. While the phase space of this system is four-dimensional, it can be reduced to two dimensions on a Poincaré surface of section [11, 12]. The open kicked rotator [10, 13–15] is a stroboscopic model with a two-dimensional phase space that is computationally more tractable, yet has the same phenomenology as open ballistic quantum dots. We give a description of the open kicked rotator, both in quantum mechanical and in classical terms.

2.2.1 Closed system

We begin with the closed system (without the leads). It was shown in chapter 1 that the kicked rotator is described by the following Hamiltonian [17, 18]

$$H = -\frac{\hbar^2}{2I_0}\frac{\partial^2}{\partial\theta^2} + \frac{K I_0}{\tau_0}\cos\theta \sum_{n=-\infty}^{\infty} \delta_s(t - n\tau_0)\,, \tag{2.1}$$

where the variable $\theta \in (0, 2\pi)$ is the angular coordinate of a particle moving along a circle (with moment of inertia I_0), kicked periodically at time intervals τ_0 (with a strength $\propto K\cos\theta$). To avoid a spurious breaking of time-reversal symmetry later on, when we open up the system, we represent the kicking by a symmetrized delta function: $\delta_s(t) = \frac{1}{2}\delta(t-\epsilon) + \frac{1}{2}\delta(t+\epsilon)$, with infinitesimal ϵ. The ratio $\hbar\tau_0/2\pi I_0 \equiv h_{\rm eff}$ represents the effective Planck constant, which governs the

quantum-to-classical crossover. For convenience, we will use the rescaled variables x and p introduced in chapter 1.

Classically, the stroboscopic time evolution of the kicked rotator is described by the following map, relating x_{n+1}, p_{n+1} at time $n+1$ to x_n, p_n at time n:

$$x_{n+1} = x_n + p_n + \frac{K}{4\pi} \sin 2\pi x_n \ \text{ modulo } 1\,, \tag{2.2a}$$

$$p_{n+1} = p_n + \frac{K}{4\pi} \left(\sin 2\pi x_n + \sin 2\pi x_{n+1} \right). \tag{2.2b}$$

The classical mechanics becomes fully chaotic for $K \gtrsim 7$, with Lyapunov exponent $\lambda \approx \ln(K/2)$. For smaller K the phase space is mixed, containing both regions of chaotic and of regular motion. The reduction of the shot noise in a mixed phase space system was numerically studied in billiards [3], but here we will restrict ourselves to the fully chaotic regime.

The stroboscopic time evolution of a wave function is given by the Floquet operator $\mathcal{F}$. Since we would like to compare the quantum kicked rotator to a chaotic quantum dot, without dynamical localization, we follow the usual procedure of quantizing phase space on the unit torus $\{x, p \mid \text{modulo } 1\}$, rather than on a cylinder. This amounts to a discretization of, say, the real space coordinate x. Thus the real space coordinate and momentum eigenvalues are given by $x_m = m/M$ and $p_n = n/M$, with $m,n = 1,2,\ldots M$. For $1/h_{\text{eff}} \equiv M$ an *even integer*, $\mathcal{F}$ can be represented by an $M \times M$ unitary symmetric matrix. In coordinate representation the matrix elements of $\mathcal{F}$ are given by (see Appendix 2.A)

$$\mathcal{F}_{mm'} = (X U^\dagger \Pi U X)_{mm'}, \tag{2.3a}$$

$$U_{mm'} = \frac{1}{\sqrt{M}} \exp\left(-i 2\pi m m'/M\right), \tag{2.3b}$$

$$X_{mm'} = \delta_{mm'} \exp\left[-i \frac{MK}{4\pi} \cos(2\pi m/M)\right], \tag{2.3c}$$

$$\Pi_{mm'} = \delta_{mm'} \exp\left(-i\pi m^2/M\right). \tag{2.3d}$$

The matrix product $U^\dagger \Pi U$ can be evaluated in closed form, resulting in the manifestly symmetric expression

$$(U^\dagger \Pi U)_{mm'} = M^{-1/2} e^{-i\pi/4} \exp[i(\pi/M)(m-m')^2]. \tag{2.4}$$

The eigenvalues $e^{-i\varepsilon_\mu}$ of $\mathcal{F}$ define the quasi-energies $\varepsilon_\mu \in (0, 2\pi)$. The mean spacing $2\pi/M$ of the quasi-energies plays the role of the mean level spacing δ in the quantum dot.

2.2.2 Open system

We now turn to a description of the open kicked rotator, following Refs. [10, 15, 16]. To model a pair of N-mode ballistic leads, we impose open boundary conditions in a subspace of Hilbert space represented by the indices $m_n^{(\alpha)}$ in coordinate representation. The subscript $n = 1,2,\dots N$ labels the modes and the superscript $\alpha = 1,2$ labels the leads. A $2N \times M$ projection matrix P describes the coupling to the ballistic leads. Its elements are

$$P_{nm} = \begin{cases} 1 & \text{if } m = n \in \{m_n^{(\alpha)}\}, \\ 0 & \text{otherwise.} \end{cases} \tag{2.5}$$

Therefore the $M \times M$ matrix $Q = 1 - P^{\mathrm{T}}P$ denotes all modes which are not lying on the leads. Particles are injected into the system by the leads, and at each iteration some of them leave the system while the remaining ones stay inside. Eventually all particles leave at the lead after a sufficient number of iterations. With this picture in mind, the $2N \times 2N$ scattering matrix is formed via a formal scattering series

$$\begin{aligned} S(\varepsilon) &= P\mathbb{F}P^{\mathrm{T}} + P\mathbb{F}Q\mathbb{F}P^{\mathrm{T}} + P(\mathbb{F}Q)^2\mathbb{F}P^{T} + \cdots \\ &= P\frac{1}{1-\mathbb{F}Q}\mathbb{F}P^{\mathrm{T}}\,, \end{aligned} \tag{2.6}$$

where $\mathbb{F} = \mathcal{F}e^{i\varepsilon}$ is the quasienergy-dependent Floquet matrix of the closed system. Using $PP^{\mathrm{T}} = 1$, Eq. (2.6) can be cast in the form (derived in Appendix 2.B)

$$S = \frac{P\mathcal{A}P^{\mathrm{T}} - 1}{P\mathcal{A}P^{\mathrm{T}} + 1}, \quad \mathcal{A} = \frac{1+\mathbb{F}}{1-\mathbb{F}} = -\mathcal{A}^{\dagger}, \tag{2.7}$$

which is manifestly unitary. The symmetry of $\mathbb{F}$ ensures that S is also symmetric, as it should be in the presence of time-reversal symmetry. By grouping together the N indices belonging to the same lead, the $2N \times 2N$ matrix S can be decomposed into 4 sub-blocks containing the $N \times N$ transmission and reflection matrices,

$$S = \begin{pmatrix} r & t' \\ t & r' \end{pmatrix}. \tag{2.8}$$

The Fano factor F follows from [19]

$$F = \frac{\mathrm{Tr}\, tt^{\dagger}\left(1 - tt^{\dagger}\right)}{\mathrm{Tr}\, tt^{\dagger}}\,. \tag{2.9}$$

This concludes the description of the stroboscopic model studied in this thesis. For completeness, we briefly mention how to extend the model to include a tunnel barrier in the leads. To this end we replace Eq. (2.6) by

$$S(\varepsilon) = -(1 - \mathcal{P}\mathcal{P}^{\mathrm{T}})^{1/2} + \mathcal{P}\frac{1}{1 - \mathbb{F}(1 - \mathcal{P}^{\mathrm{T}}\mathcal{P})}\mathbb{F}\mathcal{P}^{\mathrm{T}} . \tag{2.10}$$

The $2N \times M$ coupling matrix $\mathcal{P}$ has elements

$$\mathcal{P}_{nm} = \begin{cases} \sqrt{\Gamma_n} & \text{if } m = n \in \{m_n^{(\alpha)}\}, \\ 0 & \text{otherwise,} \end{cases} \tag{2.11}$$

with $\Gamma_n \in (0,1)$ the tunnel probability in mode n. Ballistic leads correspond to $\Gamma_n = 1$ for all n. The scattering matrix (2.10) can equivalently be written in the form used conventionally in quantum chaotic scattering [20, 21]:

$$S(\varepsilon) = -1 + 2W(\mathcal{A}^{-1} + W^{\mathrm{T}}W)^{-1}W^{\mathrm{T}}, \tag{2.12}$$

with $W = \mathcal{P}(1 + \sqrt{1 - \mathcal{P}^{\mathrm{T}}\mathcal{P}})^{-1}$ and $\mathcal{A}$ defined in Eq. (2.7).

2.3 Quantum-to-classical crossover of shot noise

Here we use the stroboscopic model to study the quantum-to-classical crossover of the shot noise in a ballistic chaotic quantum dot. Our goal is to prove that the suppression of the Fano factor F, predicted theoretically [2] and observed experimentally [7], is essentially due to the absence of noise on classical trajectories. We study the model in two complementary ways. First we present a fully numerical, quantum mechanical solution. Then we compare with a partially analytical, semiclassical solution, which is an implementation for this particular model of a general scheme presented recently by Silvestrov, Goorden, and Beenakker [5].

2.3.1 Quantum mechanical calculation

To calculate the transmission matrix from Eq. (2.6) we need to determine an $N \times N$ submatrix of the inverse of an $M \times M$ matrix. The ratio $M/2N = \tau_D$ is the mean dwell time in the system in units of the kicking time τ_0. This should be a large number, to avoid spurious effects from the stroboscopic description.

For large M/N we have found it efficient to do the partial inversion by iteration. Let $\mathcal{B}^{-1} \equiv (1 - \mathbb{F}Q)^{-1}$ be the inverse $M \times M$ matrix in Eq. (2.6), then the

scattering matrix can be expressed as $S = P\mathcal{X}$ with $\mathcal{X} = \mathcal{B}^{-1}\mathbb{F}P^{\mathrm{T}}$. Therefore, a particular element $S_{m_1m_2}$ of the scattering matrix is given by

$$S_{m_1m_2} = \begin{pmatrix} P_{m_11} & P_{m_12} \cdots & P_{m_1M} \end{pmatrix} \begin{pmatrix} \mathcal{X}_{1m_2} \\ \mathcal{X}_{2m_2} \\ \vdots \\ \mathcal{X}_{Mm_2} \end{pmatrix}. \tag{2.13}$$

The associated linear equations

$$(1-\mathbb{F}Q)\begin{pmatrix} \mathcal{X}_{1m_2} \\ \mathcal{X}_{2m_2} \\ \vdots \\ \mathcal{X}_{Mm_2} \end{pmatrix} = \mathbb{F}\begin{pmatrix} P_{m_21} \\ P_{m_22} \\ \vdots \\ P_{m_2M} \end{pmatrix} \tag{2.14}$$

can be solved iteratively. The iterative procedure we found most stable was the bi-conjugate-stabilized-gradient routine `F11BSF` from the NAG (Numerical Algorithms Group) library. Each step of the iteration requires a multiplication by $\mathbb{F}$, which can be done efficiently with the help of the fast-Fourier-transform algorithm [22]. We made sure that the iteration was fully converged (error estimate 0.1%). In comparison with a direct matrix inversion, the iterative calculation is much quicker: the time required scales $\propto M^2 \ln M$ rather than $\propto M^3$.

To study the quantum-to-classical crossover we reduce the quantum parameter $h_{\mathrm{eff}} = 1/M$ by two orders of magnitude at fixed classical parameters $\tau_D = M/2N = 5, 10, 30$ and $K = 7, 14, 21$. (These three values of K correspond, respectively, to Lyapunov exponents $\lambda = 1.3, 1.9, 2.4$.) The left edge of the leads is at $m/M = 0.1$ and $m/M = 0.8$. Ensemble averages are taken by sampling 10 random values of the quasi-energy $\varepsilon \in (0, 2\pi)$. We are interested in the semiclassical, large-N regime (typically $N > 10$). The average transmission $N^{-1}\langle \mathrm{Tr}\, tt^{\dagger}\rangle \approx 1/2$ is then insensitive to the value of h_{eff}, since quantum corrections are of order $1/N$ and therefore relatively small [21]. The Fano factor (2.9), however, is seen to depend strongly on h_{eff}, as shown in Fig. 2.1. The line through the data points follows from the semiclassical theory of Ref. [5], as explained in the next section.

In Fig. 2.2 we have plotted the numerical data on a double-logarithmic scale, to demonstrate that the suppression of shot noise observed in the simulation is indeed governed by the Ehrenfest time τ_E. The functional dependence predicted for $N > \sqrt{M}$ is [5]

$$F = \tfrac{1}{4} e^{-\tau_E/\tau_D}, \quad \tau_E = \lambda^{-1} \ln(N^2/M) + c, \tag{2.15}$$

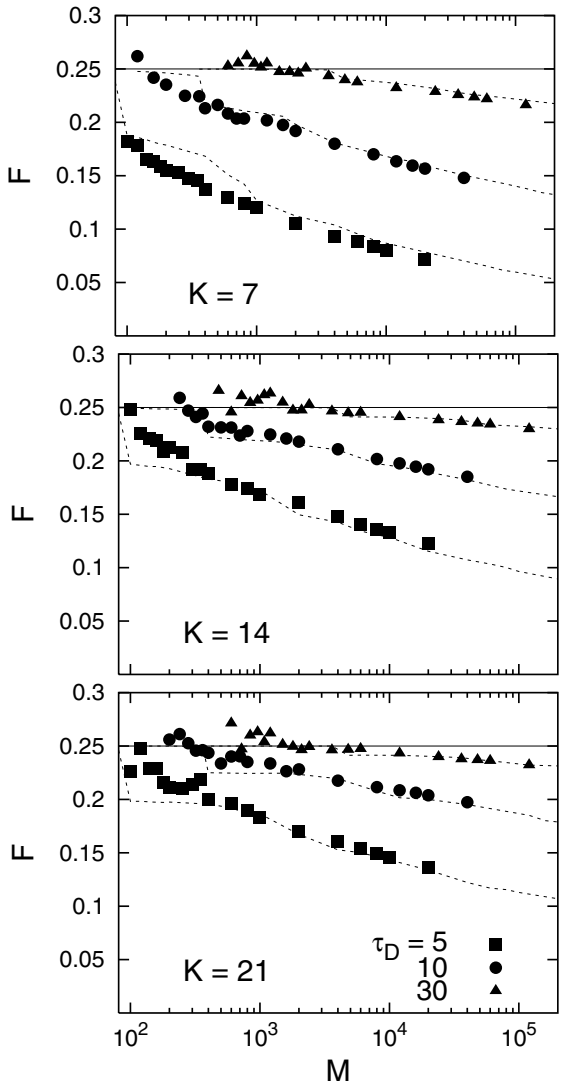

Figure 2.1: Dependence of the Fano factor F on the dimensionality of the Hilbert space $M = 1/h_{\rm eff}$, at fixed dwell time $\tau_D = M/2N$ and kicking strength K. The data points follow from the quantum mechanical simulation in the open kicked rotator. The solid line at $F = \frac{1}{4}$ is the M-independent result of random-matrix theory. The dashed lines are the semiclassical calculation using the theory of Ref. [5]. There are no fit parameters in the comparison between theory and simulation.

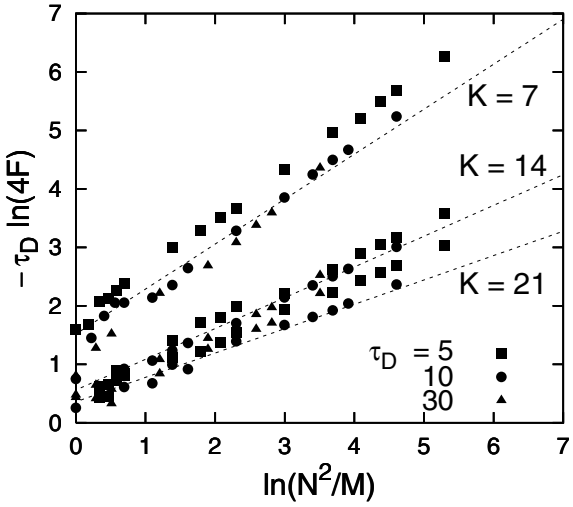

Figure 2.2: Demonstration of the logarithmic scaling of the Fano factor F with the parameter $N^2/M = M/(2\tau_D)^2$. The data points follow from the quantum mechanical simulation and the lines are the analytical prediction (2.15), with c a fit parameter. The slope $\lambda^{-1} = 1/\ln(K/2)$ of each line is not a fit parameter.

with c a K-dependent coefficient of order unity. As shown in Fig. 2.2, the data follows quite nicely the logarithmic scaling with $N^2/M = M/(2\tau_D)^2$ predicted by Eq. (2.15) and understood as a next to leading order correction for the dominant $\ln(M)$-scaling of τ_E in the closed systems. This corresponds to a scaling with $w^2/L\lambda_F$ in a two-dimensional quantum dot (with λ_F the Fermi wave length and w and L the width of the point contacts and of the dot, respectively.) We note that the same parametric scaling governs the quantum-to-classical crossover in the superconducting proximity effect [10, 23].

2.3.2 Semiclassical calculation

To describe the data from our quantum mechanical simulation we use the semiclassical approach of Ref. [5]. To that end we first identify which points in the x, p phase space of lead 1 are transmitted to lead 2 and which are reflected back to lead 1. By iteration of the classical map (2.2) we arrive at phase space portraits as shown in Fig. 2.3 (top panels). Points of different color (or gray scale) identify the initial conditions that are transmitted or reflected.

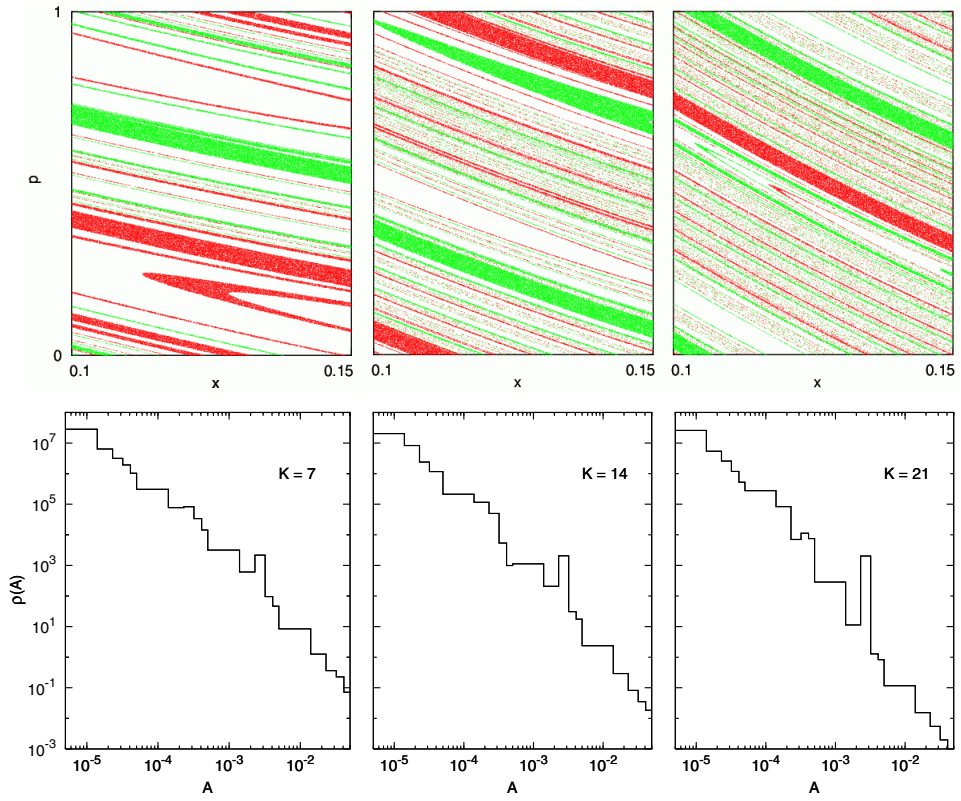

Figure 2.3: Upper panels: phase space portrait of lead 1, for $\tau_D = 10$ and different values of K. Each point represents an initial condition for the classical map (2.2), that is either transmitted through lead 2 (black/red) or reflected back through lead 1 (gray/green). Only initial conditions with dwell times ≤ 3 are shown for clarity. Lower panels: histogram of the area distribution of the transmission and reflection bands, calculated from the corresponding phase space portrait in the upper panel. Areas greater than $h_{\text{eff}} = 1/M$ correspond to noiseless scattering channels.

The transmitted and reflected points group together in nearly parallel, narrow bands. Each transmission or reflection band (labeled by an index j) supports noiseless scattering channels provided its area A_j in phase space is greater than $h_{\text{eff}} = 1/M$. The total number N_0 of noiseless scattering channels is estimated by

$$N_0 = M \sum_j A_j \theta(A_j - 1/M), \tag{2.16}$$

with $\theta(x) = 0$ if $x < 0$ and $\theta(x) = 1$ if $x > 0$. In the classical limit $M \to \infty$ one has $N_0 = N$, so all channels are noiseless and the Fano factor vanishes [8].

As argued in Ref. [5], the contribution to the Fano factor from the $N - N_0$ noisy channels can be estimated as $1/4N$ per channel. In the quantum limit $N_0 = 0$ one then has the result $F = 1/4$ of random-matrix theory [24]. The prediction for the quantum-to-classical crossover of the Fano factor is

$$\begin{aligned} F &= \frac{M}{4N} \sum_j A_j \theta(1/M - A_j) \\ &= \frac{M}{4N} \int_0^{1/M} A\rho(A)\, dA, \end{aligned} \tag{2.17}$$

with band density $\rho(A) = \sum_j \delta(A - A_j)$. The solid curves in Fig. 2.1 give the resulting Fano factor, according to Eq. (2.17). The quantum limit $F = 1/4$ follows from the total area $\int_0^1 A\rho(A)\, dA = N/M$. The lower panels of Fig. 2.3 show the band density in the form of a histogram. We have approximated the areas of the bands from the monodromy matrix of the classical map, as detailed in the Appendix 2.C.

2.3.3 Scattering states in the lead

To investigate further the correspondence between the quantum mechanical and semiclassical descriptions we compare the quantum mechanical eigenstates $|U_i\rangle$ of $t'^\dagger t'$ with the classical transmission bands. Phase space portraits of eigenstates are given by the Husimi function

$$\mathcal{H}_i(m_x, m_p) = |\langle U_i | m_x, m_p \rangle|^2. \tag{2.18}$$

The state $|m_x, m_p\rangle$ is a Gaussian wave packet centered at $x = m_x/M$, $p = m_p/M$. In position representation it reads

$$\langle m | m_x, m_p \rangle \propto \sum_{k=-\infty}^{\infty} e^{-\pi(m - m_x + kN)^2/N} e^{2\pi i m_p m/N}. \tag{2.19}$$

The summation over k ensures periodicity in m. The transmission bands typically support several modes, thus the eigenvalues T_i are nearly degenerate at unity. We choose the group of eigenstates with $T_i > 0.9995$ and plot the Husimi function for the projection onto the subspace spanned by these eigenstates:

$$\mathcal{H}(m_x, m_p) = \sum_{T_i > 0.9995} \mathcal{H}_i(m_x, m_p). \tag{2.20}$$

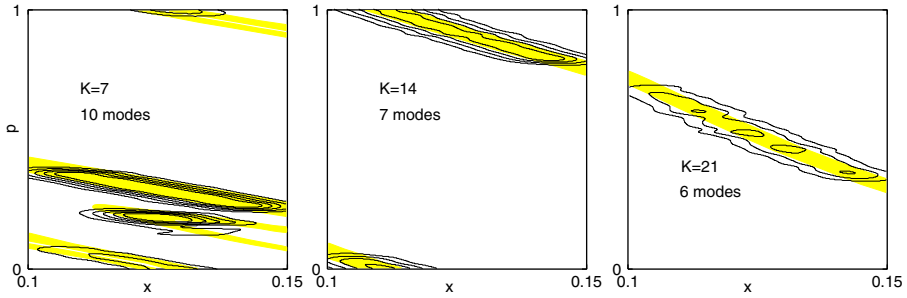

Figure 2.4: Contour plots of the Husimi function (2.20) in lead 1 for $M = 2400$, $\tau_D = 10$, and $K = 7, 14, 21$. The outer contour is at the value 0.15, inner contours increase with increments of 0.1. Yellow/Gray regions are the classical transmission bands with area $> 1/M$, extracted from Fig. 2.3.

As shown in Fig. 2.4, this quantum mechanical function indeed corresponds to a phase-space portrait of the classical transmission bands with area $> 1/M$.

2.4 Conclusion

We have presented compelling numerical evidence for the validity of the theory of the Ehrenfest-time dependent suppression of shot noise in a ballistic chaotic system [2, 5]. The key prediction [2] of an exponential suppression of the noise power with the ratio τ_E/τ_D of Ehrenfest time and dwell time is observed over two orders of magnitude in the simulation. We have also tested the semiclassical theory proposed recently [5], and find that it describes the fully quantum mechanical data quite well. It would be of interest to extend the simulations to mixed chaotic/regular dynamics and to systems which exhibit localization.

2.A Floquet matrix in coordinate representation

The Floquet operator $\mathcal{F}$ relates the wave function from time t to $t+1$,

$$\psi(x, t+1) = \langle x|\mathcal{F}|\psi(t)\rangle \, . \tag{2.21}$$

For the symmetrized kicked rotator, $\mathcal{F}$ can be factorized into the product of the evolution operators corresponding to the half-interaction, free propagation and half-interaction,

$$\mathcal{F} = X(\hat{x})\, G(\hat{p})\, X(\hat{x}) \, , \tag{2.22}$$

with

$$X(\hat{x}) = \exp\left(-\frac{i}{\hbar_{\rm eff}}\,\frac{K}{8\pi^2}\cos 2\pi\hat{x}\right)\,, \tag{2.23a}$$

$$G(\hat{p}) = \exp\left(-\frac{i}{\hbar_{\rm eff}}\,\frac{\hat{p}^2}{2}\right)\,. \tag{2.23b}$$

Substituting $\mathcal{F}$ in Eq. (2.21), one arrives at

$$\begin{aligned}\psi(x,t+1) &= \sum_{m=-\infty}^{\infty}\int_0^1 dx'\langle x|X(\hat{x})|m\rangle\; G(p_m)\;\langle m|X(\hat{x})|x'\rangle\;\langle x'|\psi(t)\rangle \\ &= \sum_{m=-\infty}^{\infty}\int_0^1 dx' X(x)X(x')e^{-i\pi h_{\rm eff}m^2}e^{i2\pi m(x-x')}\psi(x',t). \end{aligned}\tag{2.24}$$

The corresponding classical map, given by Eq. (2.2), is invariant under the transformation $p \to p+r$ with r being an integer. If such a symmetry also exists in the associated quantum system then it would correspond to a transformation in the momentum eigenvalue given by

$$m \to m + \frac{r}{2\pi\hbar_{\rm eff}} \equiv m + \frac{r}{h_{\rm eff}}\,. \tag{2.25}$$

Since m has to be an integer, Eq. (2.25) can be valid only if

$$\frac{r}{h_{\rm eff}} \equiv M \tag{2.26}$$

is an integer, or equivalently, only if

$$h_{\rm eff} = \frac{r}{M} \tag{2.27}$$

is a rational number. The condition that $h_{\rm eff}$ is a rational number is a resonance condition for the quantum system, which makes it possible to describe the quantum dynamics in a finite M-dimensional Hilbert space. For the generic irrational case, p is no longer periodic and the quantum dynamics occurs in an infinite Hilbert space. Thus one has to deal with an infinite Floquet matrix, for which there are different methods depending on the type of irrationality [25].

Let us now show that the rationality of the effective Planck constant gives rise to a finite dimensional Hilbert space. By introducing

$$m = n + lM\,, \tag{2.28a}$$

$$n = 0,1,\cdots,M-1\,, \tag{2.28b}$$

$$l = \cdots,-1,0,1,\cdots\,, \tag{2.28c}$$

Eq. (2.24) can be written as

$$\psi(x,t+1) = X(x) \sum_{n=0}^{M-1} e^{-i\pi r n^2/M} \int_0^1 dx' e^{i2\pi n(x-x')} X(x') \psi(x',t) \times \sum_{l=-\infty}^{\infty} e^{i2\pi l(Mx-Mx')} , \qquad (2.29)$$

where we have assumed that at least one of r and M is even. It is straightforward to check that this choice leads to the translation symmetry of the matrix elements of the Floquet matrix, namely $\mathcal{F}_{m+M,m'+M} = \mathcal{F}_{mm'}$. Using the Poisson summation formula

$$\sum_{l=-\infty}^{\infty} e^{i2\pi l(Mx-Mx')} = \sum_{l=-\infty}^{\infty} \delta(Mx - Mx' + l) , \qquad (2.30)$$

we obtain

$$\psi(x,t+1) = \frac{1}{M} X(x) \sum_{n=0}^{M-1} \sum_{l=-L_1}^{L_2} \exp\left(-i\pi r n^2/M\right) \exp(-i2\pi nl/M) \times X(x+l/M) \ \psi(x+l/M,t) , \qquad (2.31)$$

where the range $[-L_1, L_2]$ is determined such that $x, x' \in [0,1)$. Because of the periodicity of system with respect to the position, Eq. (2.31) is invariant under transformation $l \to l+M$, hence the summation over l can be restricted to the range $[0,M)$. This indicates that the position has a finite discrete spectrum $x_l = l/M$ with $l = 0, \cdots, M-1$, resulting from the fact that the system is periodic in momentum with period 1. Since the variable x in Eq. (2.31) is arbitrary, we set it at $x_m = m/M$ with $m = 0, \cdots, M-1$. Therefore Eq. (2.31) can be expressed as

$$\langle x_m|\psi(t+1)\rangle = \sum_{m'=0}^{M-1} \mathcal{F}_{mm'} \ \langle x_{m'}|\psi(t)\rangle , \qquad (2.32)$$

where $\mathcal{F}_{mm'}$ represents the elements of the finite $M \times M$ Floquet matrix in the position representation

$$\mathcal{F}_{mm'} = X(x_m) \left[\frac{1}{M} \sum_{n=0}^{M-1} e^{-i\pi r n^2/M} \ e^{i2\pi n(m-m')/M} \right] X(x_{m'}) . \qquad (2.33)$$

For a system which is restricted to be on the unit torus ($r = 1$), the summation can be evaluated with the help of the relation

$$\sum_{n=0}^{M-1} \exp\left[-i\pi(n-m+m')^2/M\right] = \sum_{n=0}^{N-1} \exp\left[-i\pi n^2/M\right] = \sqrt{\frac{M}{i}} \qquad (2.34)$$

for integer numbers $m, m' \in [0, M)$. This results in the simple symmetric form

$$\mathcal{F}_{mm'} = \frac{1}{\sqrt{iM}}\, X(x_m)\, \exp\left[i(\pi/M)(m-m')^2\right]\, X(x_{m'})\,. \tag{2.35}$$

2.B Derivation of Eq. (2.7)

We use a series expansion for the inverse operator in Eq. (2.6),

$$\begin{aligned}
[1-\mathbb{F}Q]^{-1} &= \left[1-\mathbb{F}+\mathbb{F}P^{\mathrm{T}}P\right]^{-1} \\
&= \left[(1-\mathbb{F})\left(1+\frac{1}{1-\mathbb{F}}\mathbb{F}P^{\mathrm{T}}P\right)\right]^{-1} \\
&= \left[1+\frac{1}{1-\mathbb{F}}\mathbb{F}P^{\mathrm{T}}P\right]^{-1}\frac{1}{1-\mathbb{F}} \\
&= \sum_{k\geq 0}\left(-\frac{1}{1-\mathbb{F}}\mathbb{F}P^{\mathrm{T}}P\right)^{k}\frac{1}{1-\mathbb{F}}\,.
\end{aligned} \tag{2.36}$$

Substituting this expansion in Eq. (2.6) and using $PP^{\mathrm{T}} = 1$, we obtain

$$\begin{aligned}
S &= \sum_{k\geq 0} P\left(-\frac{1}{1-\mathbb{F}}\mathbb{F}P^{\mathrm{T}}P\right)^{k}\frac{1}{1-\mathbb{F}}\mathbb{F}P^{\mathrm{T}} \\
&= \sum_{k\geq 0}(-1)^k\left(P\frac{1}{1-\mathbb{F}}\mathbb{F}P^{\mathrm{T}}\right)^{k+1} \\
&= \frac{P\,(\mathbb{F}/1-\mathbb{F})\,P^{\mathrm{T}}}{1+P\,(\mathbb{F}/1-\mathbb{F})\,P^{\mathrm{T}}} \\
&= \frac{P\,(2\mathbb{F}/1-\mathbb{F})\,P^{\mathrm{T}}}{P\,(2/1-\mathbb{F})\,P^{\mathrm{T}}} \\
&= \frac{P\left[(1+\mathbb{F}/1-\mathbb{F})-1\right]P^{\mathrm{T}}}{P\left[(1+\mathbb{F}/1-\mathbb{F})+1\right]P^{\mathrm{T}}} \\
&= \frac{P\mathcal{A}P^{\mathrm{T}}-1}{P\mathcal{A}P^{\mathrm{T}}+1}\,.
\end{aligned} \tag{2.37}$$

2.C Calculation of the band area distribution

We approximate the bands in Fig. 2.3 by straight and narrow strips in the shape of a parallelogram, disregarding any curvature. This is a good approximation in

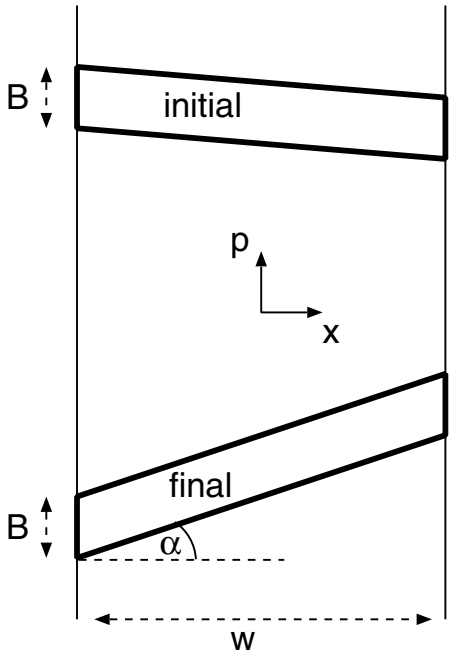

Figure 2.5: Phase space of a lead (width w) showing two areas (in the shape of a parallelogram) that are mapped onto each other after n iterations. They have the same base B, so the same area, but their tilt angle α is different.

particular for the narrowest bands, which are the ones that determine the shot noise. Each band is characterized by a mean dwell time n (in units of τ_0). We disregard any variations in the dwell time within a given band, assuming that the entire band exits through one of the two leads after n iterations. (We have found numerically that this is true with rare exceptions.)

The case of a reflection band is shown in Fig. 2.5. The initial and final parallelograms have the same height, set by the width $w = N/M$ of the lead. Since the map is area preserving, the base B of the two parallelograms should be the same as well. We have approximated the areas of the bands from the monodromy matrix $M(x_k, p_k)$, which describes the stretching by the map of an infinitesimal displacement δx_k, δp_k:

$$\begin{pmatrix} \delta x_{k+1} \\ \delta p_{k+1} \end{pmatrix} = M(x_k, p_k) \begin{pmatrix} \delta x_k \\ \delta p_k \end{pmatrix}. \tag{2.38}$$

From Eq. (2.2) one finds

$$M(x_k, p_k) = \begin{pmatrix} \Lambda(x_k) & 1 \\ \Lambda(x_k)\Lambda(x_{k+1}) - 1 & \Lambda(x_{k+1}) \end{pmatrix}, \tag{2.39a}$$

$$\Lambda(x) = 1 + \frac{K}{2}\cos 2\pi x. \tag{2.39b}$$

To calculate the band area $A = Bw$, we assume that the monodromy matrix $M(x_k, p_k)$ does not vary appreciably within the band at each iteration $k = 1, 2, \ldots n$. An initial vector $\vec{e}_i$ within the parallelogram is then mapped after n iterations onto a final vector $\vec{e}_f$ given by

$$\vec{e}_f = \mathcal{M}\vec{e}_i, \;\; \mathcal{M} = M(x_n, p_n)\cdots M(x_2, p_2)M(x_1, p_1), \tag{2.40}$$

with x_1, p_1 inside the initial parallelogram. We apply Eq. (2.40) to the vectors that form the sides of the initial and final parallelograms. The base vector $\vec{e}_i = B\hat{p}$ is mapped onto the vector $\vec{e}_f = \pm w(\hat{x} + \hat{p}\tan\alpha)$, with α the tilt angle of the final parallelogram. It follows that $B|\mathcal{M}_{xp}| = w$, hence

$$A = w^2/|\mathcal{M}_{xp}|. \tag{2.41}$$

We obtain the Fano factor F by a Monte Carlo procedure. An initial point x_1, p_1 is chosen randomly in lead 1 and iterated until it exits through one of the two leads. The product $\mathcal{M}$ of monodromy matrices starting from that point gives the area A of the band to which it belongs, according to Eq. (2.41). The fraction of points with $A < 1/M$ then equals $w^{-1}\int_0^{1/M} A\rho(A)\,dA = 4F$, according to Eq. (2.17).

To assess the accuracy of this procedure, we repeat the calculation of the Fano factor with initial points chosen randomly in lead 2 (instead of lead 1). The difference is about 5%. The dashed lines in Fig. 2.1 are the average of these two results.

Bibliography

[1] C. W. J. Beenakker and C. Schönenberger, Physics Today (May 2003).

[2] O. Agam, I. Aleiner, and A. Larkin, Phys. Rev. Lett. **85**, 3153 (2000).

[3] H.-S. Sim and H. Schomerus, Phys. Rev. Lett. **89**, 066801 (2002).

[4] R. G. Nazmitdinov, H.-S. Sim, H. Schomerus, and I. Rotter, Phys. Rev. B **66**, 241302(R) (2002).

[5] P. G. Silvestrov, M. C. Goorden, and C. W. J. Beenakker, Phys. Rev. B **67**, 241301(R) (2003).

[6] H. Schanz, M. Puhlmann, and T. Geisel, Phys. Rev. Lett. **91**, 134101 (2003).

[7] S. Oberholzer, E. V. Sukhorukov, and C. Schönenberger, Nature **415**, 765 (2002).

[8] C. W. J. Beenakker and H. van Houten, Phys. Rev. B **43**, 12066 (1991).

[9] S. Oberholzer, 2001, Ph.D. thesis (Basel University).

[10] Ph. Jacquod, H. Schomerus, and C.W.J. Beenakker, Phys. Rev. Lett. **90**, 207004 (2003).

[11] E. B. Bogomolny, Nonlinearity **5**, 805 (1992).

[12] R. E. Prange, Phys. Rev. Lett. **90**, 070401 (2003).

[13] F. Borgonovi, I. Guarneri, and D. L. Shepelyansky, Phys. Rev. A **43**, 4517 (1991).

[14] F. Borgonovi and I. Guarneri, J. Phys. A **25**, 3239 (1992).

[15] A. Ossipov, T. Kottos, and T. Geisel, Phys. Rev. E **65**, 055209 (2002).

[16] Y. V. Fyodorov and H.-J. Sommers, JETP Lett. **72**, 422 (2000).

[17] F. M. Izrailev, Phys. Rep. **196**, 299 (1990).

[18] F. Haake, *Quantum Signatures of Chaos* (Springer, Berlin, 1992).

[19] M. Büttiker, Phys. Rev. Lett. **65**, 2901 (1990).

[20] T. Guhr, A. Müller-Groeling, and H. A. Weidenmüller, Phys. Rep. **299**, 189 (1998).

[21] C. W. J. Beenakker, Rev. Mod. Phys. **69**, 731 (1997).

[22] R. Ketzmerick, K. Kruse, and T. Geisel, Physica D **131**, 247 (1999).

[23] M. G. Vavilov and A. I. Larkin, Phys. Rev. B **67**, 115335 (2003).

[24] R. A. Jalabert, J.-L. Pichard, and C. W. J. Beenakker, Europhys. Lett. **27**, 255 (1994).

[25] T. Dittrich and U. Smilansky, Nonlinearity **4**, 85 (1991).

Chapter 3

Quantum-to-classical crossover of mesoscopic conductance fluctuations

3.1 Introduction

Sample-to-sample fluctuations of the conductance of disordered systems have a universal regime, in which they are independent of the mean conductance. The requirement for these universal conductance fluctuations [1, 2] is that the sample size should be small compared to the localization length. The mean conductance is then much larger than the conductance quantum e^2/h.

The same condition applies to the universality of conductance fluctuations in ballistic chaotic quantum dots [3, 4], although there is no localization in these systems. Random-matrix-theory (RMT) has the universal limit

$$\lim_{N\to\infty} \operatorname{var} G = \frac{1}{8} \tag{3.1}$$

for the variance of the conductance G in units of e^2/h. Here N is the number of modes transmitted through each of the two ballistic point contacts that connect the quantum dot to electron reservoirs. Since the mean conductance $\langle G\rangle = N/2$, the condition for universality remains that the mean conductance should be large compared to the conductance quantum.

In the present chapter we will show that there is actually an upper limit on N, beyond which RMT breaks down in a quantum dot and the universality of the conductance fluctuations is lost. Since the width w of a point contact should be small compared to the size L of the quantum dot, in order to have chaotic scattering, a trivial requirement is $N \ll M$, where M is the number of transverse

modes in a cross-section of the quantum dot. (In two dimensions, $N \simeq w/\lambda_F$ and $M \simeq L/\lambda_F$, with λ_F the Fermi wavelength.) By considering the quantum-to-classical crossover, we arrive at the more stringent requirement

$$1 \ll N \ll \sqrt{M} e^{\lambda \tau_{erg}/2}, \tag{3.2}$$

with λ the Lyapunov exponent and τ_{erg} the ergodic time of the classical chaotic dynamics. The requirement is more stringent than $N \ll M$ because, typically, λ^{-1} and τ_{erg} are both equal to the time of flight τ_0 across the system, so the exponential factor in Eq. (3.2) is not far from unity.

Expressed in terms of time scales, the upper limit in Eq. (3.2) says that τ_{erg} should be larger than the Ehrenfest time [5, 6]

$$\tau_E = \max\left[0, \lambda^{-1} \ln \frac{N^2}{M}\right]. \tag{3.3}$$

The condition $\tau_{erg} > \tau_E$ which we find for the universality of conductance fluctuations is much more stringent than the condition $\tau_D > \tau_E$ for the validity of RMT found in other contexts [5–13]. Here $\tau_D \approx (M/N)\tau_0$ is the mean dwell time in the quantum dot, which is $\gg \tau_{erg}$ in any chaotic system.

The outline of this chapter is as follows. In Sec. 3.2 we describe the quantum mechanical model that we use to calculate $\mathrm{var}\, G$ numerically, which is the same stroboscopic model used in previous investigations of the Ehrenfest time [9, 11, 14]. The data is interpreted semiclassically in Sec. 3.4, leading to the crossover criterion (3.2). We conclude in Sec. 3.5.

3.2 Stroboscopic model

The physical system we have in mind is a ballistic (clean) quantum dot in a two-dimensional electron gas, connected by two ballistic leads to electron reservoirs. While the phase space of this system is four-dimensional, it can be reduced to two dimensions on a Poincaré surface of section [15, 16]. The open kicked rotator [9, 11, 14, 17–20] is a stroboscopic model with a two-dimensional phase space. We summarize how this model is constructed, following Ref. [11].

One starts from the closed system (without the leads). The kicked rotator describes a particle moving along a circle, kicked periodically at time intervals τ_0. We set to unity the stroboscopic time τ_0 and the Plank constant $\hbar$. The stroboscopic time evolution of a wave function is given by the Floquet operator $\mathcal{F}$, which can be represented by an $M \times M$ unitary symmetric matrix. The even

integer M defines the effective Planck constant $h_{\rm eff} = 1/M$. In the discrete coordinate representation ($x_m = m/M$, $m = 0,1,\ldots,M-1$) the matrix elements of $\mathcal{F}$ are given by

$$\mathcal{F}_{m'm} = M^{-1/2} e^{-i\pi/4} e^{i2\pi M S(x_{m'},x_m)}, \tag{3.4}$$

where S is the map generating function,

$$S(x',x) = \tfrac{1}{2}(x'-x)^2 - (K/8\pi^2)(\cos 2\pi x' + \cos 2\pi x), \tag{3.5}$$

and K is the kicking strength. The eigenvalues $\exp(-i\varepsilon_m)$ of $\mathcal{F}$ define the quasi-energies $\varepsilon_m \in (0,2\pi)$. The mean spacing $2\pi/M$ of the quasi-energies plays the role of the mean level spacing δ in the quantum dot.

To model a pair of N-mode ballistic leads, we impose open boundary conditions in a subspace of Hilbert space represented by the indices $m_n^{(\alpha)}$. The subscript $n = 1,2,\ldots N$ labels the modes and the superscript $\alpha = 1,2$ labels the leads. A $2N \times M$ projection matrix P describes the coupling to the ballistic leads. Its elements are

$$P_{nm} = \begin{cases} 1 & \text{if } m = n \in \{m_n^{(\alpha)}\}, \\ 0 & \text{otherwise.} \end{cases} \tag{3.6}$$

The mean dwell time is $\tau_D = M/2N$ (in units of τ_0).

The matrices P and $\mathcal{F}$ together determine the quasi-energy dependent scattering matrix

$$S(\varepsilon) = P[e^{-i\varepsilon} - \mathcal{F}(1 - P^{\rm T}P)]^{-1}\mathcal{F}P^{\rm T}. \tag{3.7}$$

The symmetry of $\mathcal{F}$ ensures that S is also symmetric, as it should be in the presence of time-reversal symmetry. By grouping together the N indices belonging to the same lead, the $2N \times 2N$ matrix S can be decomposed into 4 sub-blocks containing the $N \times N$ transmission and reflection matrices,

$$S = \begin{pmatrix} r & t' \\ t & r' \end{pmatrix}. \tag{3.8}$$

The conductance G (in units of e^2/h) follows from the Landauer formula

$$G = {\rm Tr}\, tt^\dagger. \tag{3.9}$$

The open quantum kicked rotator has a classical limit, described by a map on the torus $\{x,p \mid \text{modulo } 1\}$. The classical phase space, including the leads, is shown in Fig. 3.1. The map relates x,p at time k to x',p' at time $k+1$:

$$p' = \frac{\partial}{\partial x'} S(x',x), \quad p = -\frac{\partial}{\partial x} S(x',x). \tag{3.10}$$

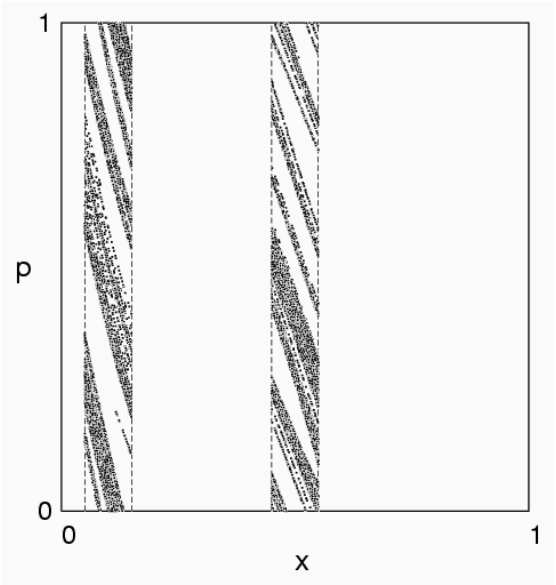

Figure 3.1: Classical phase space of the open kicked rotator. The dashed lines indicate the two leads (shown for the case $\tau_D = 5$). Inside each lead we plot the initial and final coordinates of trajectories which are transmitted from the left to the right lead after at most 3 iterations (with $K = 7.5$). The points cluster along narrow "transmission bands".

The classical mechanics becomes fully chaotic for $K \gtrsim 7$, with Lyapunov exponent $\lambda \approx \ln(K/2)$. For smaller K the phase space is mixed, containing both regions of chaotic and of regular motion. We will restrict ourselves to the fully chaotic regime in this chapter.

3.3 Numerical results

To calculate the conductance (3.9) we need to invert the $M \times M$ matrix between square brackets in Eq. (3.7). We do this numerically using an iterative procedure [11]. The iteration can be done efficiently using the fast-Fourier-transform algorithm to calculate the application of $\mathcal{F}$ to a vector. The time required to calculate S scales as $M^2 \ln M$, which for large M is quicker than the M^3 scaling of a direct inversion. The memory requirements scale as M, because we need not store the full scattering matrix to obtain the conductance.

We distinguish two types of mesoscopic fluctuations in the conductance. The first type appears upon varying the quasi-energy ε for a given scattering matrix $S(\varepsilon)$. Since these fluctuations have no classical analogue (the classical map (3.10) being ε-independent), we refer to them as quantum fluctuations. The second type appears upon varying the position of the leads, so these involve variation of the scattering matrix at fixed ε. We refer to them as sample-to-sample fluctuations. They have both a quantum mechanical component and a classical analogue. One could introduce a third type of fluctuations, involving both variation of ε and of the lead positions. We have found (as expected) that these are statistically equivalent to the sample-to-sample fluctuations at fixed ε, so we need not distinguish between fluctuations of type two and three.

We have calculated the variance $\operatorname{var} G = \langle G^2 \rangle - \langle G \rangle^2$ of the conductance, either by varying ε at fixed lead positions (quantum fluctuations) or by varying both ε and lead positions (sample-to-sample fluctuations). Since the quantum interference pattern is completely different only for energy variations of order of the Thouless energy $1/\tau_D$, we choose a number τ_D of equally spaced values of ε in the interval $(0, 2\pi)$. We take 10 different lead positions, randomly located at the x-axis in Fig. 3.1. To investigate the quantum-to-classical crossover, we change $h_{\text{eff}} = 1/M$ while keeping the dwell time $\tau_D = M/2N$ constant. The results are plotted in Figs. 3.2 and 3.3.

3.4 Interpretation

We interpret the numerical data by assuming that the variance of the conductance is the sum of two contributions: a universal quantum mechanical contribution $\mathcal{V}_{\text{RMT}}$ given by random-matrix theory and a nonuniversal quasiclassical contribution $\mathcal{V}_{\text{cl}}$ determined by sample-to-sample fluctuations in the classical transmission probabilities.

The RMT contribution equals [3, 4]

$$\mathcal{V}_{\text{RMT}} = \tfrac{1}{8}, \tag{3.11}$$

in the presence of time-reversal symmetry. The classical contribution is calculated from the classical map (3.10), by determining the probability $P_{1\to 2}$ of a particle injected randomly through lead 1 to escape via lead 2. Since the conductance is given semiclassically by $G_{\text{cl}} = N P_{1\to 2}$, we obtain

$$\mathcal{V}_{\text{cl}} = N^2 \operatorname{var} P_{1\to 2}. \tag{3.12}$$

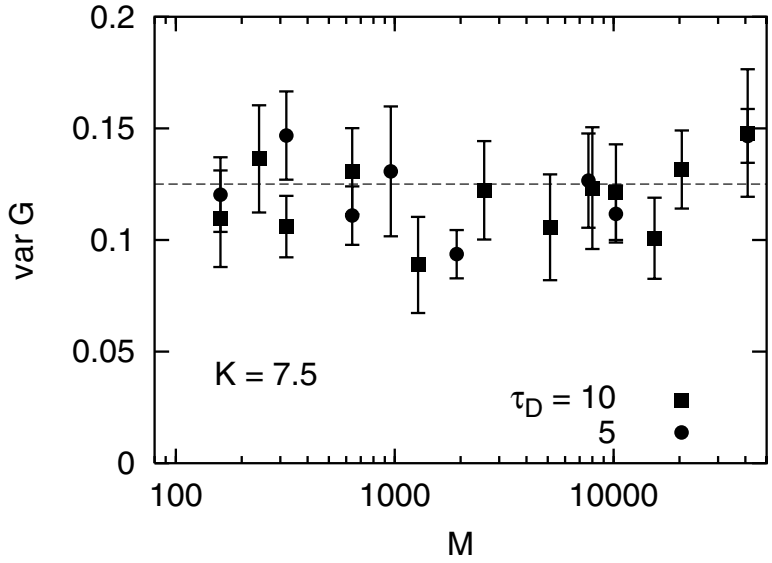

Figure 3.2: Variance of the conductance fluctuations obtained numerically by varying ε with fixed lead positions. Error bars indicate the scatter of values obtained for different lead positions. Results are shown as a function of $1/h_{\rm eff} = M$, for two values of the dwell time $\tau_D = M/2N$. The dashed line is the RMT prediction $\mathrm{var}\, G = \frac{1}{8}$.

We plot $\mathrm{var}\, G = \mathcal{V}_{\rm RMT} + \mathcal{V}_{\rm cl}$ in Fig. 3.3 (dashed curves), for comparison with the results of our full quantum mechanical calculation. The agreement is excellent.

We now would like to investigate what ratio of time scales governs the crossover from quantum to classical fluctuations.

To estimate the magnitude of the sample-to-sample fluctuations in the classical transmission probability, we use results from Ref. [6]. There it was found that the starting points (and end points) of transmitted trajectories are not homogeneously distributed in phase space. Instead, they cluster together in nearly parallel, narrow bands. These transmission bands are clearly visible in Fig. 3.1. The largest band has an area $A_{\rm max} = A_0 e^{-\lambda \tau_{\rm erg}}$ determined by the ergodic time $\tau_{\rm erg}$. This is the time required for a trajectory to explore the whole accessible phase space. The values of $\tau_{\rm erg}$ and A_0 depend on the degree of collimation of the beam of trajectories injected into the system [6]. For our model, without col-

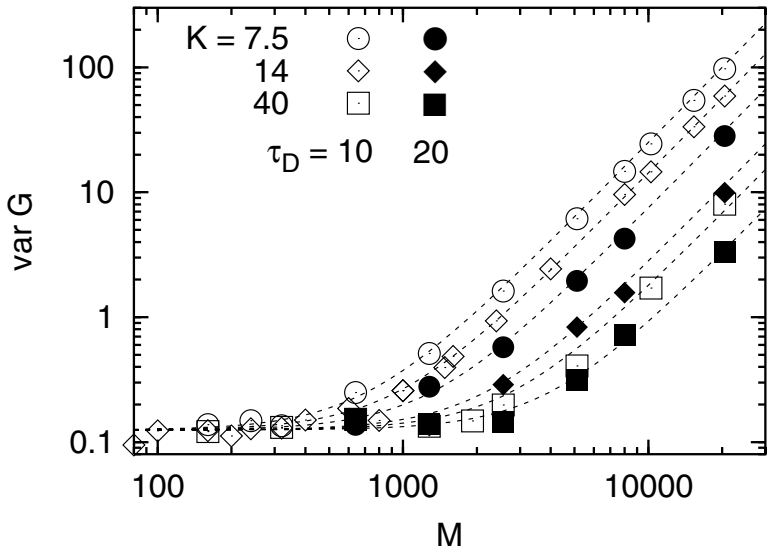

Figure 3.3: Same as Fig. 3.2, but now for an ensemble in which the lead positions and the quasi-energy are both varied. The dashed lines are the sum of the RMT value (3.11) and the classical result (3.12). Results are shown for three values of the kicking strength K. Open symbols are for the dwell time $\tau_D = 10$ and closed ones for $\tau_D = 20$.

limation, one has $\tau_{\rm erg}$ of order unity (one stroboscopic period) and $A_0 \simeq (N/M)^2$. The typical transmission band has an area $A_0 e^{-\lambda\tau_D}$ which is exponentially smaller than $A_{\rm max}$ (since $\tau_D = M/2N \gg \tau_{\rm erg}$).

As the position of the lead is moved around, transmission bands move into and out of the lead. The resulting fluctuations in the transmission probability $P_{1\to 2}$ are dominated by the largest band. Since there is an exponentially large number $e^{\lambda\tau_D}$ of typical bands, their fluctuations average out. The total area in phase space of the lead is $A_{\rm lead} = N/M$, so we estimate the mean squared fluctuations in $P_{1\to 2}$ at

$$\mathrm{var}\, P_{1\to 2} \simeq (A_{\rm max}/A_{\rm lead})^2 = c\,(N/M)^2 e^{-2\lambda\tau_{\rm erg}}, \tag{3.13}$$

with c and $\tau_{\rm erg}$ of order unity. We have tested this functional dependence numerically for the map (3.10), and find a reasonable agreement (see Fig. 3.4). Both the exponential dependence on λ and the quadratic dependence on $\tau_D = M/2N$ are consistent with the data. We find $\tau_{\rm erg} = 0.68$ of order unity, as expected.

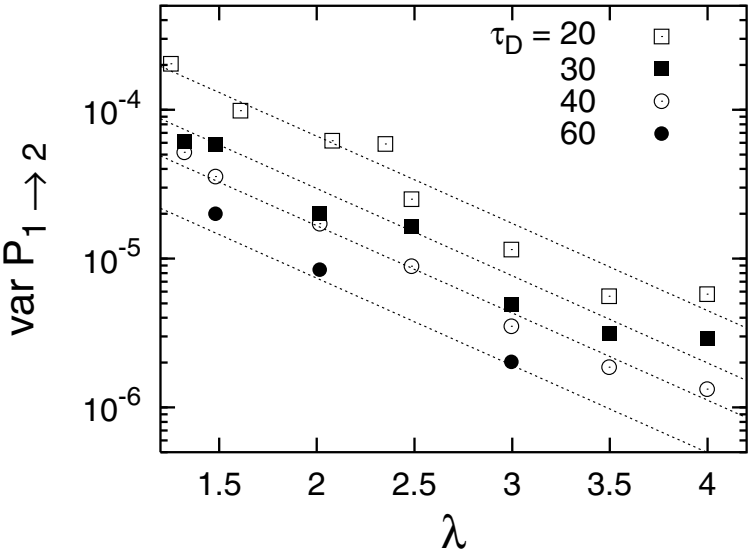

Figure 3.4: Variance of the classical fluctuations of the transmission probability $P_{1\to 2}$ upon changes of lead positions, calculated numerically from the map (3.10). The data is shown for four values of the dwell time τ_D, as a function of the Lyapunov exponent $\lambda = \ln(K/2)$. The dotted lines are the analytical prediction (3.13), with fit parameters $c = 1.6$ and $\tau_{\rm erg} = 0.68$ (the same for all data sets).

Eqs. (3.12) and (3.13) imply

$$\mathrm{var}\, G = \tfrac{1}{8} + c\ (N^4/M^2)\ e^{-2\lambda\tau_{\rm erg}}. \tag{3.14}$$

In Fig. 3.5 we plot the same data as in Fig. 3.3, but now as a function of (N^4/M^2) $e^{-2\lambda\tau_{\rm erg}}$. We see that the functional dependence (3.14) is approached for large dwell times.

The quantum fluctuations of RMT dominate over the classical fluctuations if $N^2\,\mathrm{var}\, P_{1\to 2} \ll 1$. Using the estimate (3.13), this amounts to the condition

$$\tau_{\rm erg} > \max\left[0, \lambda^{-1}\ln(N^2/M)\right] \equiv \tau_E \tag{3.15}$$

that the ergodic time exceeds the Ehrenfest time. Notice that condition (3.15) is always satisfied if $N^2 < M \equiv 1/h_{\rm eff}$. This agrees with the findings of Ref. [6], that the breakdown of RMT starts when $N \gtrsim \sqrt{M}$.

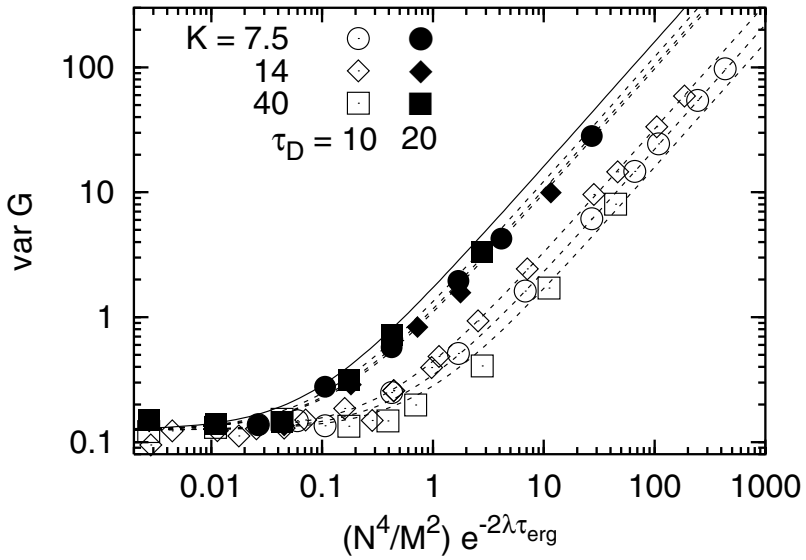

Figure 3.5: Same data as in Fig. 3.3 rescaled to show the approach to a single limiting curve in the large dwell time limit. The solid line is calculated from Eq. (3.14), with the same parameters $c = 1.6$, $\tau_{\rm erg} = 0.68$ as in Fig. 3.4.

3.5 Conclusions

In summary, we have presented both a fully quantum mechanical and a semi-classical calculation of the quantum-to-classical crossover from universal to non-universal conductance fluctuations. The two calculations are in very good agreement, without any adjustable parameter (compare data points with curves in Fig. 3.3). We have also given an analytical approximation to the numerical data, which allows us to determine the parametric dependence of the crossover.

We have found that universality of the conductance fluctuations requires the ergodic time $\tau_{\rm erg}$ to be larger than the Ehrenfest time τ_E. This condition is much more stringent than the condition that the dwell time τ_D should be larger than τ_E, found previously for universality of the shot noise in a quantum dot [6, 10, 11]. The universality of the excitation gap in a quantum dot connected to a superconductor is also governed by the ratio τ_D/τ_E rather than $\tau_{\rm erg}/\tau_E$ [5, 7–9], as is the universality of the weak localization effect [12, 13]. These two properties have in common that they represent ensemble averages, rather than sample-to-sample

fluctuations.

We propose that what we have found here for the conductance is generic for other transport properties: That the breakdown of RMT with increasing τ_E occurs when $\tau_E > \tau_D$ for ensemble averages and when $\tau_E > \tau_{\rm erg}$ for the fluctuations. This has immediate experimental consequences, because it is much easier to violate the condition $\tau_E > \tau_{\rm erg}$ than the condition $\tau_E > \tau_D$.

To test this proposal, an obvious next step would be to determine the ratio of time scales that govern the breakdown of universality of the fluctuations in the superconducting excitation gap. The numerical data in Refs. [14] and [21] was interpreted in terms of the ratio τ_E/τ_D, but an alternative description in terms of the ratio $\tau_E/\tau_{\rm erg}$ was not considered.

One final remark about the distinction between classical and quantum fluctuations, explained in Sec. 3.3. It is possible to suppress the classical fluctuations entirely, by varying only the quasi-energy at fixed lead positions. In that case we would expect the breakdown of universality to be governed by τ_D/τ_E instead of $\tau_{\rm erg}/\tau_E$. Our numerical data (Fig. 3.2) does not show any systematic deviation from RMT, probably because we could not reach sufficiently large systems in our simulation.

Our final remark above has been criticized by Jacquod and Sukhorukov [22]. They argue that the numerical data of Fig. 3.2 (and similar data of their own) does not show any systematic deviation from RMT because quantum fluctuations remain universal if $\tau_E > \tau_D$. Their argument relies on the assumption that the effective RMT of Ref. [6] holds not only for the classical fluctuations (as we assume here), but also for the quantum fluctuations. The effective RMT says that quantum fluctuations are due to a number $N_{\rm eff} \approx N e^{-\tau_E/\tau_D}$ of transmission channels with an RMT distribution. Universality of the quantum fluctuations is then guaranteed even if $N_{\rm eff} \ll N$, as long as $N_{\rm eff}$ is still large compared to unity.

This line of reasoning, if pursued further, contradicts the established theory [12, 13] of the τ_E dependence of weak localization. RMT says that the weak localization correction $\delta G = -\frac{1}{4}$ is independent of the number of channels [3, 4]. Validity of the effective RMT at the quantum level would therefore imply that weak localization remains universal if $\tau_E > \tau_D$, as long as $N e^{-\tau_E/\tau_D} \gg 1$. This contradicts the result $\delta G = \frac{1}{4} e^{-\tau_E/\tau_D}$ of Refs. [12] and [13].

Bibliography

[1] B. L. Altshuler, JETP Lett. **41**, 648 (1985).

[2] P. A. Lee and A. D. Stone, Phys. Rev. Lett. **55**, 1622 (1985).

[3] H. U. Baranger and P. A. Mello, Phys. Rev. Lett. **73**, 142 (1994).

[4] R. A. Jalabert, J.-L. Pichard, and C. W. J. Beenakker, Europhys. Lett. **27**, 255 (1994).

[5] M. G. Vavilov and A. I. Larkin, Phys. Rev. B **67**, 115335 (2003).

[6] P. G. Silvestrov, M. C. Goorden, and C. W. J. Beenakker, Phys. Rev. B **67**, 241301 (2003).

[7] A. Lodder and Yu. V. Nazarov, Phys. Rev. B **58**, 5783 (1998).

[8] P. G. Silvestrov, M. C. Goorden, and C. W. J. Beenakker, Phys. Rev. Lett. **90**, 116801 (2003).

[9] Ph. Jacquod, H. Schomerus, and C.W.J. Beenakker, Phys. Rev. Lett. **90**, 207004 (2003).

[10] O. Agam, I. Aleiner, and A. Larkin, Phys. Rev. Lett. **85**, 3153 (2000).

[11] J. Tworzydło, A. Tajic, H. Schomerus, and C. W. J. Beenakker, Phys. Rev. B **68**, 115313 (2003).

[12] I. L. Aleiner and A. I. Larkin, Phys. Rev. B **54**, 14423 (1996).

[13] I. Adagideli, Phys. Rev. B **68**, 233308 (2003).

[14] M.C. Goorden, Ph. Jacquod, and C.W.J. Beenakker, Phys. Rev. B **68**, 220501 (2003).

[15] E. B. Bogomolny, Nonlinearity **5**, 805 (1992).

[16] R. E. Prange, Phys. Rev. Lett. **90**, 070401 (2003).

[17] F. Borgonovi, I. Guarneri, and D. L. Shepelyansky, Phys. Rev. A **43**, 4517 (1991).

[18] F. Borgonovi and I. Guarneri, J. Phys. A **25**, 3239 (1992).

[19] Y. V. Fyodorov and H.-J. Sommers, JETP Lett. **72**, 422 (2000).

[20] A. Ossipov, T. Kottos, and T. Geisel, Europhys. Lett. **62**, 719 (2003).

[21] A. Kormanyos, Z. Kaufmann, C. J. Lambert, and J. Cserti, Phys. Rev. B **67**, 172506 (2003).

[22] Ph. Jacquod and E. V. Sukhorukov, Phys. Rev. Lett. **92**, 116801 (2004).

Chapter 4

Weak localization of the open kicked rotator

4.1 Introduction

Random-matrix theory (RMT) makes system-independent ("universal") predictions about quantum mechanical systems with a chaotic classical dynamics [1–4]. The presence or absence of time-reversal symmetry (TRS) identifies two universality classes. RMT is also capable of describing the crossover between the universality classes, e.g. when TRS is broken by the application of a magnetic field B. The crossover is predicted to depend on a single system-specific parameter, being the mean absolute curvature of the energy levels E_i around $B = 0$. More precisely, a universal magnetic-field dependence of spectral correlations is predicted when B is rescaled by the characteristic field

$$B_c = \left(\frac{1}{\Delta} \left\langle \left| \frac{d^2 E_i}{dB^2} \right|_{B=0} \right\rangle \right)^{-1/2}, \tag{4.1}$$

with Δ the mean level spacing. This prediction has been tested in a variety of computer simulations [5–7].

In open systems there exists a similar prediction of universality for transport properties, but now the characteristic field depends also on the conductance g of the point contacts that couple the chaotic quantum dot to electron reservoirs [8–11]. A universal magnetic field dependence is predicted if B is rescaled by $B_c\sqrt{g}$, provided g is large compared to the conductance quantum e^2/h. To provide a numerical test of this prediction is the purpose of this chapter.

We present a computer simulation of the open quantum kicked rotator [12–15], which is a stroboscopic model of a quantum dot coupled to electron reservoirs by ballistic point contacts. The ensemble averaged conductance increases upon breaking of TRS, as a manifestation of weak localization. The height, width, and lineshape of the weak localization peak are compared with the predictions of RMT.

The simulation itself is straightforward, but the formulation of the model is not. There exist several ways to break TRS in the closed kicked rotator [16–19] and related models [20–23]. When opening up the system one needs to ensure that the scattering matrix satisfies the reciprocity relation

$$S(-B) = S^T(B). \tag{4.2}$$

(The superscript T indicates the transpose of the scattering matrix S.) We also require that TRS is broken already at the level of the classical dynamics (as it is in a quantum dot in a uniform magnetic field). Finally, we need to relate the TRS-breaking parameter in the stroboscopic formulation to the flux enclosed by the quantum dot. All these issues are addressed in Secs. 4.2 and 4.3 before we proceed to the actual simulation in Sec. 4.4. We conclude in Sec. 4.5.

4.2 Time-reversal-symmetry breaking in the open kicked rotator

4.2.1 Formulation of the model

The kicked rotator is a particle moving along a circle, kicked periodically at time intervals τ_0 [1,17]. The stroboscopic time evolution of a wave function is given by the Floquet operator $\mathcal{F}$. In addition to the stroboscopic time τ_0 and the moment of inertia I_0, which we set to unity, $\mathcal{F}$ depends on the kicking strength K and the TRS-breaking parameter γ. We require

$$\mathcal{F}(-\gamma) = \mathcal{F}^T(\gamma), \tag{4.3}$$

which guarantees the reciprocity relation (4.2) for the scattering matrix when we open up the model.

We will consider two different representations of $\mathcal{F}$, both of which can be written as an $M \times M$ unitary matrix. The classical limit corresponds to a map defined on a toroidal phase space. The difference between the two representations is whether TRS breaking persists in the classical limit or not. The simplest representation of $\mathcal{F}$ has one kick per period. It breaks TRS quantum mechanically, but not

classically. This would correspond to a quantum dot that encloses a flux tube, but in which the magnetic field vanishes. A more realistic model has TRS breaking both at the quantum mechanical and at the classical level. We have found that we then need a minimum of three kicks per period.

4.2.2 Three-kick representation

We will mainly consider the three-kick model, so we describe it first. In this model TRS is broken both quantum mechanically and classically. Stroboscopic models with multiple kicks per period of different magnitude were studied previously in the context of quantum ratchets [21]. Inspired by that work, we study the time-dependent Hamiltonian

$$\begin{aligned} H(t) &= \frac{p^2}{2} + \frac{1}{2}V(\theta)\sum_n [\delta_\epsilon(t-n+\epsilon)+\delta_\epsilon(t-n-\epsilon)] \\ &\quad + \gamma\cos(\theta)\sum_n \delta(t-n+1/3) \\ &\quad - \gamma\cos(\theta)\sum_n \delta(t-n-1/3), \end{aligned} \tag{4.4}$$

with ϵ an infinitesimal. The angular momentum operator $p = -i\hbar_{\rm eff}\partial_\theta$ is canonically conjugate to the angle $\theta \in [0, 2\pi)$. The effective Planck constant is $\hbar_{\rm eff} = \hbar\tau_0/I_0$. The potential [18, 19, 24, 25]

$$V(\theta) = K\cos(\pi q/2)\cos(\theta) + \frac{1}{2}K\sin(\pi q/2)\sin(2\theta) \tag{4.5}$$

with $q \neq 0$ breaks the parity symmetry of the model. The form of the potential is such that in the large K-limit the diffusion constant does not depend on q. For $\gamma = 0$ there are two kicks per period in Eq. (4.4), but since they are displaced by an infinitesimal amount we still call this a "single-kick" model. For $\gamma \neq 0$ two more kicks appear with opposite sign at finite displacement. We will see that this choice guarantees the reciprocity criterion (4.3) for the Floquet operator.

The reduction of the Floquet operator

$$\mathcal{F} = \mathcal{T}\exp\left[-\frac{i}{\hbar_{\rm eff}}\int_0^1 H(t)dt\right] \tag{4.6}$$

(with $\mathcal{T}$ the time ordering operator) to a discrete, finite form is obtained only for special values of $\hbar_{\rm eff}$, known as resonances [17]. We have to reconsider the usual

condition for resonances in the presence of additional, TRS-breaking kicks. Here our analysis departs from the quantum ratchet analogy [21].

The initial wave function $\psi(x)$ evolves in one period to a final wave function $\bar{\psi}(x)$, given by

$$\begin{aligned}\bar{\psi}(\theta) &= \exp(-iV(\theta)/2\hbar_{\rm eff})\exp(i\hbar_{\rm eff}\partial_\theta^2/6) \\ &\quad\times\exp(-i\gamma\cos(\theta)/\hbar_{\rm eff})\exp(i\hbar_{\rm eff}\partial_\theta^2/6) \\ &\quad\times\exp(i\gamma\cos(\theta)/\hbar_{\rm eff})\exp(i\hbar_{\rm eff}\partial_\theta^2/6) \\ &\quad\times\exp(-iV(\theta)/2\hbar_{\rm eff})\psi(\theta). \end{aligned} \tag{4.7}$$

One recognizes three factors describing free propagation for $1/3$ of a period, each followed by a kick. The resonance condition for free propagation is $\hbar_{\rm eff} = 2\pi r/M$, with r an odd integer and M an even integer [17]. The free propagation

$$\psi_1(\theta) = \exp(i\hbar_{\rm eff}\partial_\theta^2/6)\psi(\theta) \tag{4.8}$$

is then given by (derived in Appendix 4.A)

$$\begin{aligned}\psi_1\left(\theta+\frac{2\pi}{3M}n\right) &= \frac{1}{3M}\sum_{m,n'=0}^{3M-1}\exp\left(-i\frac{\pi r}{3M}m^2\right) \\ &\quad\times\exp\left(-im\frac{2\pi}{3M}(n'-n)\right)\psi\left(\theta+\frac{2\pi}{3M}n'\right). \end{aligned} \tag{4.9}$$

Resonance means that the initial and final wave functions can be treated as discrete vectors on a $3M$-point lattice, labeled by the indices n, n'. The angle θ is an arbitrary offset parameter. Different values of θ are not coupled by the free propagation. Putting together three iterations of Eq. (4.9) we get three independent components of $\psi(\theta+2\pi n/3M)$ for $n = 0,1,2 \pmod 3$, each on an M-point lattice.

We find that the resonance property is preserved in the presence of intervening TRS-breaking kicks, provided that $r = 3$ and M even, but not a multiple of 3. [1] The free propagation (4.9) then is conveniently expressed in matrix notation. The matrix acts on an M-component vector $\psi_m = \psi(\theta+2\pi m/M)$, $m = 0,\ldots,M-1$. We choose the arbitrary phase $\theta = 0$, so that (see Appendix 4.A)

$$(\psi_1)_m = \sum_{m'=0}^{M-1}(U^\dagger\Sigma U)_{mm'}\psi_{m'}. \tag{4.10}$$

[1] The associated classical map is periodic in momentum with period 6π. This constrains us to quantize the map on the torus $\{\theta\in[0,2\pi)\,,\ p\in[0,6\pi)\}$, resulting in the finite Hilbert space of dimension $M = 12\pi^2/h_{\rm eff}$.

The matrices are defined by

$$\Sigma_{mm'} = \delta_{mm'} e^{-i\pi m^2/M}, \tag{4.11}$$
$$U_{mm'} = M^{-1/2} e^{-2\pi i m m'/M}. \tag{4.12}$$

The matrix product $U^\dagger \Sigma U$ can be evaluated in closed form, with the result

$$\begin{aligned} \Pi_{mm'} &= (U^\dagger \Sigma U)_{mm'} \\ &= M^{-1/2} e^{-i\pi/4} \exp[i(\pi/M)(m'-m)^2]. \end{aligned} \tag{4.13}$$

Collecting results, we find that for $\hbar_{eff} = 6\pi/M$ the Floquet operator (4.7) is represented by an $M \times M$ unitary matrix, of the form

$$\mathcal{F}_{mm'} = (X \Pi Y^* \Pi Y \Pi X)_{mm'}, \tag{4.14a}$$
$$Y_{mm'} = \delta_{mm'} e^{i(M\gamma/6\pi)\cos(2\pi m/M)}, \tag{4.14b}$$
$$X_{mm'} = \delta_{mm'} e^{-i(M/12\pi)V(2\pi m/M)}. \tag{4.14c}$$

One readily verifies the reciprocity relation (4.3).

The classical map corresponding to this quantum mechanical model is derived in Appendix 4.B. We show there that TRS-breaking of the classical map is broken for $\gamma \neq 0$ in the three-kick model.

4.2.3 One-kick representation

TRS breaking in the one-kick model is constructed as a formal analogy to the magnetic vector potential, by adding an offset δ to the momentum of the kicked rotator [16–19, 24–26].

To obey reciprocity

$$\mathcal{F}(-\delta) = \mathcal{F}^T(\delta) \tag{4.15}$$

for odd M it is enough to symmetrize the expression of Ref. [16] by infinitesimally splitting the kick (as it was done in Ref. [15] for $\delta = 0$). For even M, which is more convenient for application of the fast Fourier transform, one also needs to redefine the lattice points in order to preserve reciprocity [27].

The model takes the form

$$\mathcal{F}_{mm'} = (\tilde{X} \tilde{U}^\dagger \tilde{\Pi} \tilde{U} \tilde{X})_{mm'}, \tag{4.16a}$$
$$\tilde{U}_{mm'} = M^{-1/2} e^{-2\pi i (m - \frac{M-1}{2}) m'/M}, \tag{4.16b}$$
$$\tilde{X}_{mm'} = \delta_{mm'} e^{-i(MK/4\pi)\cos(2\pi m/M + \phi)}, \tag{4.16c}$$
$$\tilde{\Pi}_{mm'} = \delta_{mm'} e^{-i\pi (m - \frac{M-1}{2} - \delta \frac{M}{2\pi})^2/M}. \tag{4.16d}$$

In addition to the TRS-breaking phase δ there is a phase ϕ to break the parity symmetry. The reciprocity property (4.15) can easily be checked.

The classical map corresponding to this model is also discussed in Appendix 4.B. It does not break TRS.

4.2.4 Scattering matrix

To model a pair of N-mode ballistic point contacts that couple the quantum dot to electron reservoirs, we impose open boundary conditions in a subspace of Hilbert space represented by the indices $m_n^{(\alpha)}$. The subscript $n = 1,2,\ldots N$ labels the modes and the superscript $\alpha = 1,2$ labels the leads. A $2N \times M$ projection matrix P describes the coupling to the ballistic leads. Its elements are

$$P_{nm} = \begin{cases} 1 & \text{if } m = n \in \{m_n^{(\alpha)}\}, \\ 0 & \text{otherwise.} \end{cases} \tag{4.17}$$

The mean dwell time is $\tau_D = M/2N$ (in units of τ_0).

The matrices P and $\mathcal{F}$ together determine the scattering matrix [13–15]

$$S(\varepsilon) = P[e^{-i\varepsilon} - \mathcal{F}(1 - P^{\mathrm{T}}P)]^{-1}\mathcal{F}P^{\mathrm{T}}, \tag{4.18}$$

where ε is the quasi-energy. The reciprocity condition (4.3) of $\mathcal{F}$ implies that also S satisfies the reciprocity condition (4.2).

By grouping together the N indices belonging to the same point contact, the $2N \times 2N$ matrix S can be decomposed into 4 sub-blocks containing the $N \times N$ transmission and reflection matrices,

$$S = \begin{pmatrix} r & t' \\ t & r' \end{pmatrix}. \tag{4.19}$$

The conductance G (in units of e^2/h, disregarding spin degeneracy) follows from the Landauer formula

$$G = \mathrm{Tr}\, tt^{\dagger}. \tag{4.20}$$

4.3 Relation with random-matrix theory

In RMT time-reversal symmetry is broken by means of the Pandey-Mehta Hamiltonian [28]

$$H = H_0 + i\alpha A, \tag{4.21}$$

which consists of the sum of a real symmetric matrix H_0 and a real antisymmetric matrix A with imaginary weight $i\alpha$. We denote by M_H the dimensionality of the Hamiltonian matrix. The two matrices H_0 and A are independently distributed with the same Gaussian distribution. The variance $v^2 = \left\langle (H_0)_{ij}^2 \right\rangle = \left\langle A_{ij}^2 \right\rangle (i \neq j)$ determines the mean level spacing $\Delta = \pi v/\sqrt{M_H}$ at the center of the spectrum for $M_H \gg 1$ and $\alpha \ll 1$.

To lowest order in perturbation theory the energy levels $E_i(\alpha)$ depend on the TRS-breaking parameter α according to

$$\delta E_i = \alpha^2 \sum_{j \neq i} \frac{A_{ij}^2}{E_i - E_j}, \tag{4.22}$$

with $\delta E_i = E_i(\alpha) - E_i(0)$ and $E_i \equiv E_i(0)$. The characteristic value α_c is determined by the mean absolute curvature,

$$\alpha_c \equiv \left(\frac{1}{\Delta} \left\langle \left| \frac{d^2 E_i}{d\alpha^2} \right|_{\alpha=0} \right\rangle \right)^{-1/2}. \tag{4.23}$$

From Eq. (4.22) we deduce that $\alpha_c \simeq \Delta/v \simeq 1/\sqrt{M_H}$, up to a numerical coefficient of order unity. A numerical calculation gives

$$\alpha_c \sqrt{M_H} \equiv \kappa_{\mathrm{RMT}} = 1.27. \tag{4.24}$$

A real magnetic field B is related to the parameter α of RMT by

$$B/B_c = \alpha/\alpha_c, \tag{4.25}$$

where B_c is determined by the level curvature according to Eq. (4.1). For a ballistic two-dimensional billiard (area A, Fermi velocity v_{F}) with a chaotic classical dynamics, one has [2, 5]

$$B_c = c \frac{h}{eA} (\Delta \sqrt{A}/\hbar v_F)^{1/2}, \tag{4.26}$$

with c a numerical coefficient that depends only on the shape of the billiard. The field B_c corresponds to a flux through the quantum dot of order $(h/e)\sqrt{\tau_{\mathrm{erg}} \Delta/\hbar} \ll h/e$, with the ergodic time τ_{erg} being the time it takes an electron to explore the available phase space in the quantum dot.

The analogue of Eqs. (4.1) and (4.25) for the quantum kicked rotator considered here is

$$\gamma/\gamma_c = \alpha/\alpha_c,\ \gamma_c \equiv \left(\frac{M}{2\pi} \left\langle \left| \frac{d^2 \phi_i}{d\gamma^2} \right|_{\gamma=0} \right\rangle \right)^{-1/2}. \tag{4.27}$$

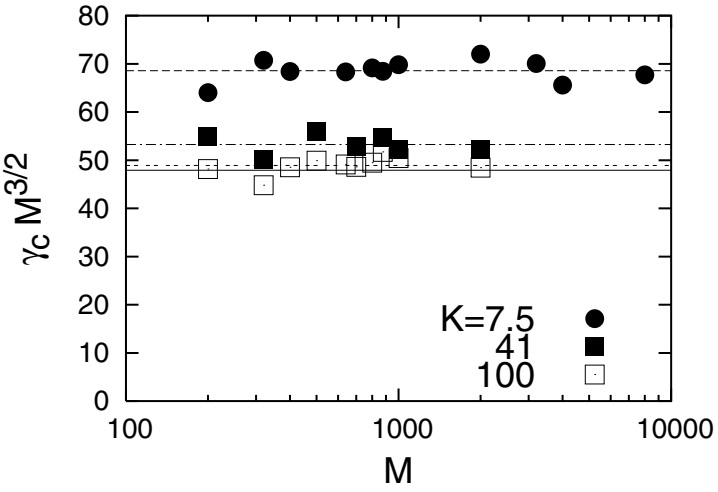

Figure 4.1: The critical value γ_c of the TRS-breaking parameter in the closed three-kick model is presented for different system sizes at fixed K. The parity-breaking parameter is $q = 0.2$. The solid line shows the large-K limit (4.28). The dashed lines are averages over M of the numerical data.

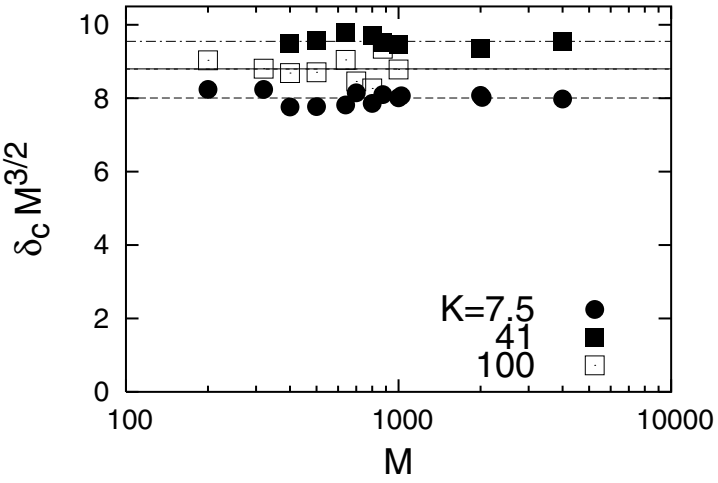

Figure 4.2: Same as Fig. 4.1, but now for the closed one-kick model. The parity-breaking parameter is $\phi = 0.2\pi$. The solid line shows the large-K limit (4.29).

Here γ is the TRS-breaking parameter in the three-kick model. The same relation applies to the one-kick model, with γ, γ_c replaced by δ, δ_c.

To complete the correspondence between the kicked rotator, RMT, and the real quantum dot, we need to determine the two characteristic values γ_c and δ_c. In Appendix 4.C we present an analytical calculation deep in the chaotic regime ($K \to \infty$), according to which

$$\lim_{K\to\infty} \gamma_c = 12\pi M^{-3/2}\kappa_{\rm RMT} = 47.9\, M^{-3/2}, \tag{4.28}$$

$$\lim_{K\to\infty} \delta_c = 4\sqrt{3}M^{-3/2}\kappa_{\rm RMT} = 8.80\, M^{-3/2}. \tag{4.29}$$

In Figs. 4.1 and 4.2 we show a numerical calculation for finite K, which confirms these analytical large-K limits.

In the open system the characteristic field scale for TRS-breaking is increased by a factor $\sqrt{g}$, with g the conductance of the point contacts. We consider ballistic N-mode point contacts, so that $g = N$, measured in units of e^2/h. The conductance $G(B)$ of the quantum dot is also measured in units of e^2/h. According to RMT, the weak localization magnetoconductance is given by [9, 11]

$$G(B) = \frac{N}{2} - \frac{1}{4}\left[1 + (2\kappa_{\rm RMT}N^{-1/2}B/B_c)^2\right]^{-1}. \tag{4.30}$$

For the quantum kicked rotator we would therefore expect a weak localization peak in the conductance given by

$$G(\gamma) = G_\infty - \frac{1}{4}\left[1 + (2\kappa_{\rm RMT}N^{-1/2}\gamma/\gamma_c)^2\right]^{-1}, \tag{4.31}$$

in the three-kick model. We define the weak localization correction $\delta G(\gamma) = G(\gamma) - G_\infty$, with G_∞ the conductance at fully broken TRS. The expression in the one-kick model is similar, with γ/γ_c replaced by δ/δ_c.

In the large-K limit we can use the analytical expressions (4.28) and (4.29) for γ_c and δ_c to obtain

$$\lim_{K\to\infty} \delta G(\gamma) = -\tfrac{1}{4}[1 + (M^{3/2}N^{-1/2}\gamma/6\pi)^2]^{-1}, \tag{4.32}$$

$$\lim_{K\to\infty} \delta G(\delta) = -\tfrac{1}{4}[1 + (M^{3/2}N^{-1/2}\delta/2\sqrt{3})^2]^{-1}. \tag{4.33}$$

In Appendix 4.D we show how these two results are consistent with a semiclassical calculation.

4.4 Numerical results

The numerical technique we use to calculate the conductance was described in Refs. [15] and [29]. The calculation of the scattering matrix (4.18) is performed efficiently by use of an iterative procedure and the fast-Fourier-transform algorithm. We need to average over many system realizations (varying lead positions and quasi-energies) to suppress statistical fluctuations. In addition, we need several points to plot the γ-dependence. This makes the calculation for large M more time consuming than earlier studies of universal conductance fluctuations in the same model at zero magnetic field [29, 30].

First we present in Figs. 4.3 and 4.4 results for the weak localization correction δG in the three-kick model as a function of the TRS-breaking parameter γ. The data are obtained by averaging over 40 lead positions and 80 quasi-energies. The parameter γ_c was calculated for the closed model using Eq. (4.27), and the resulting RMT prediction (4.31) is also shown (dotted curve).

To compare the simulation with RMT in more detail we have fitted a Lorentzian

$$\delta G = -\tfrac{1}{4}[1+(M\gamma/\gamma^*)^2]^{-1} \tag{4.34}$$

to each data set. This is the RMT result (4.31) if $\gamma^* = \gamma^*_{\rm RMT} \equiv \gamma_c M^{3/2}/(2\sqrt{2\tau_D}\,\kappa_{\rm RMT})$. The large K-limit is

$$\lim_{K\to\infty} \gamma^*_{\rm RMT} = 6\pi/\sqrt{2\tau_D}. \tag{4.35}$$

In Fig. 4.5 we plot the fitted crossover parameter γ^* as a function of M for fixed dwell time. The plot confirms the scaling with $\tau_D^{-1/2} \propto g^{-1/2}$, and also shows good agreement with the values of $\gamma^*_{\rm RMT}$ calculated from the mean level curvature (dotted lines).

We also performed numerical calculations for the one-kick model. The crossover scale δ^* extracted from a Lorentzian fit to the weak-localization peak was compared with the value $\delta^*_{\rm RMT} = \delta_c M^{3/2}/(2\sqrt{2\tau_D}\kappa_{\rm RMT})$ predicted by the mean level curvature. The large K-limit of this value is

$$\lim_{K\to\infty} \delta^*_{\rm RMT} = \sqrt{6}/\sqrt{\tau_D}. \tag{4.36}$$

We show in Fig. 4.6 the ratio $\delta^*/\delta^*_{\rm RMT}$ for the one-kick model, as well as the ratio $\gamma^*/\gamma^*_{\rm RMT}$ for the three-kick model. The ratio is close to unity for both models if the dwell time is sufficiently large. At the smallest τ_D there is some deviation from unity in the one-kick model.

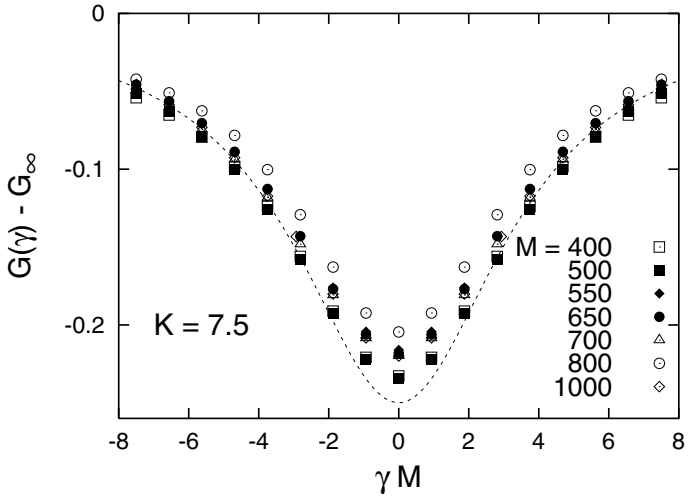

Figure 4.3: Dependence of the average conductance on the TRS-breaking parameter γ. The three-kick model is characterized by $K = 7.5$, $q = 0.2$, and $\tau_D = M/2N = 25$. The dotted line shows the RMT prediction (4.31), with γ_c calculated from the mean level curvatures (Fig. 4.1).

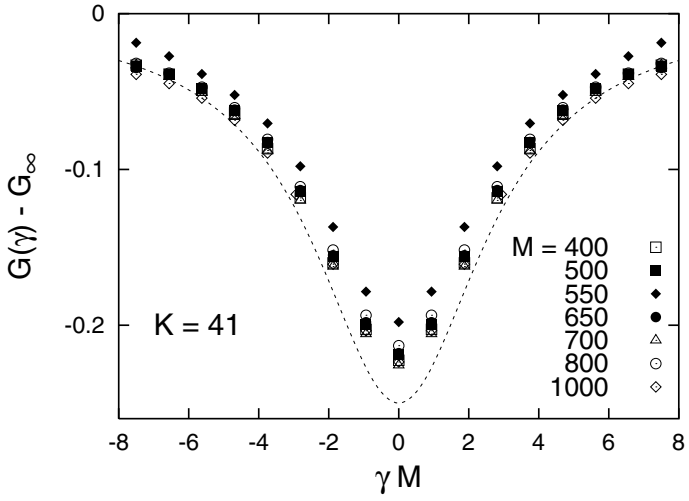

Figure 4.4: Same as Fig. 4.3, but for $K = 41$.

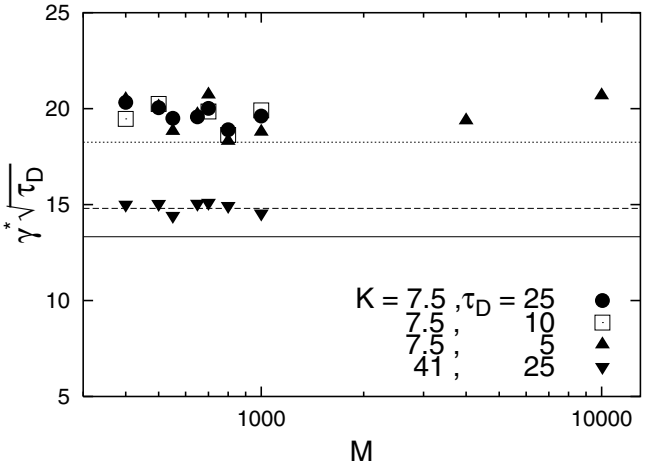

Figure 4.5: Dependence of the crossover parameter γ^* on the system size. The data are obtained by fitting the Lorentzian (4.34) to the numerical data of Figs. 4.3 and 4.4. The solid line shows the large K-limit (4.35). The dotted lines are the RMT prediction for $K = 7.5$ and $K = 41$, using γ_c found from the level curvatures in the closed model (Fig. 4.1).

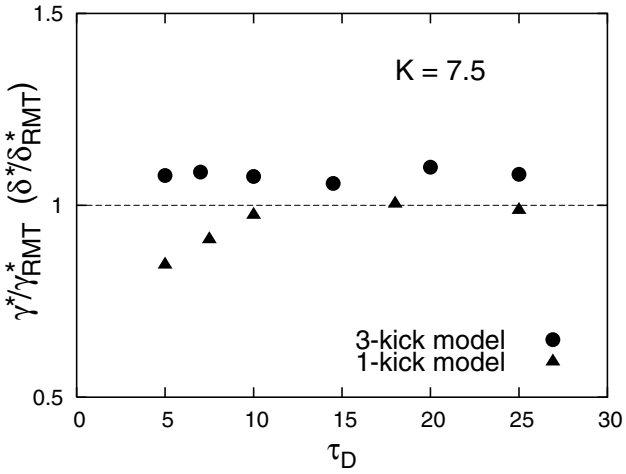

Figure 4.6: Dependence of the ratio $\gamma^*/\gamma^*_{\rm RMT}$ for the three-kick model and the ratio $\delta^*/\delta^*_{\rm RMT}$ for the one-kick model on the dwell time τ_D. Data points for a given dwell time are obtained by averaging over system sizes in the range from 200 to 1000.

The magnitude of the weak localization peak in Figs. 4.3 and 4.4 shows a small (about 10%) discrepancy with the RMT prediction. We attribute this to non-ergodic, short-time trajectories. We show in Fig. 4.8 the dependence of the magnitude of the weak localization peak $\delta G(0)$ on the dwell time. The results suggest that $\delta G(0) + \frac{1}{4} \propto 1/\tau_D$, a deviation from RMT to be expected from the Thouless energy scale (which is $\propto 1/\tau_D$). The deviation from unity in Fig. 4.6 has presumably the same origin.

We could determine the M-dependence of γ^* and $\delta G(0)$ up to $M = 10^4$ (for $K = 7.5$ and $\tau_D = 5$). The motivation for extending the calculation to large system sizes is to search for effects of the Ehrenfest time [32,33]. Although the Ehrenfest time $\tau_E \approx 3.8$ (estimating as in Ref. [15]) was comparable to $\tau_D = 5$, we did not find any systematic M-dependence in γ^* or $\delta G(0)$, cf. Figs. 4.5 and 4.7.

4.5 Conclusions

In conclusion, we have studied time-reversal symmetry breaking in quantum chaos through its effect on weak localization. We have found an overall good agreement between the universal predictions of random-matrix theory and the results for a specific quantum mechanical model of a chaotic quantum dot. In particular, the scaling $\propto g^{-1/2}$ of the crossover magnetic field with the point contact conductance g is confirmed over a broad parameter range.

Deviations from RMT that we have observed scale inversely proportional with the mean dwell time τ_D, consistent with an explanation in terms of non-ergodic short-time trajectories. These deviations therefore have a classical origin.

More interesting deviations of a quantum mechanical origin have been predicted [32, 33] in relation with the finite Ehrenfest time τ_E. This is the time scale on which a wave packet of minimal initial dimension spreads to cover the entire available phase space. The theoretical prediction is that the weak localization peak $\delta G(0) \propto e^{-\tau_E/\tau_D}$ should decay exponentially once τ_E exceeds τ_D. Our simulation extends up to $\tau_E \simeq \tau_D$, but shows no sign of this predicted decay. This is consistent with the explanation advanced by Jacquod and Sukhorukov [30] for the insensitivity of universal conductance fluctuations to a finite Ehrenfest time, based on the effective RMT of Ref. [31]. As pointed out in Ref. [29] the same explanation also implies that weak localization should not depend on the relative magnitude of τ_E and τ_D.

Because our simulation could not be extended to the regime $\tau_E > \tau_D$, this final conclusion remains tentative. It might be that the exponential suppression of $\delta G(0)$ does exist, but that our system was simply too small to see it.

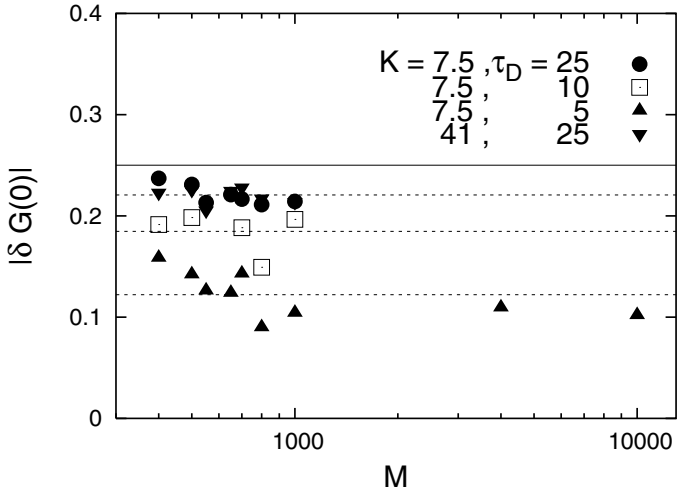

Figure 4.7: Dependence of $\delta G(0)$ on the system size M for several dwell times. Dashed lines show averages over system size.

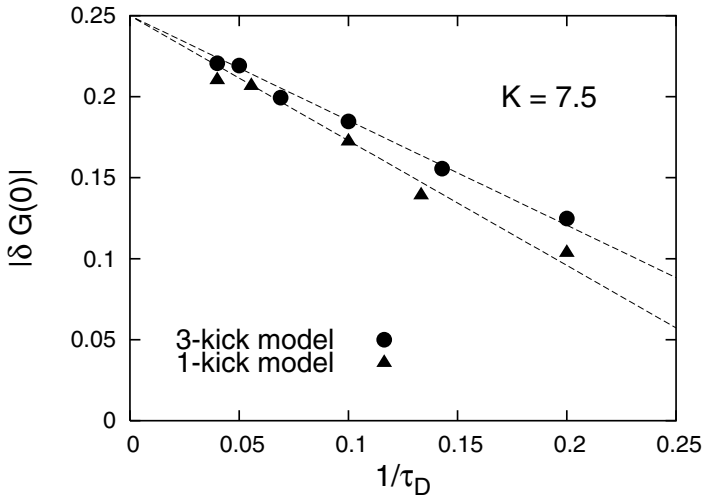

Figure 4.8: Dependence of the amplitude of the weak localization peak $\delta G(0)$ (averaged over several system sizes) on the dwell time τ_D. Dashed lines show a linear dependence on $1/\tau_D$, extrapolated to the RMT value $|\delta G(0)| = 1/4$.

4.A Derivation of the free propagator

Since without kicks the Hamiltonian (4.4) is time independent, the solution of the Schrödinger equation is conveniently represented in the form of an expansion in eigenfunctions of the angular momentum,

$$\psi(\theta,t) = \frac{1}{\sqrt{2\pi}} \sum_{n=-\infty}^{\infty} A_n(t)\, e^{in\theta} \,, \tag{4.37}$$

where the coefficients

$$A_n(t) = \frac{1}{\sqrt{2\pi}} \int_0^{2\pi} d\theta' e^{-in\theta'} \psi(\theta',t) \tag{4.38}$$

are essentially the Fourier coefficients of the time-dependent wave function $\psi(\theta,t)$. Therefore, the $1/3$-free propagation is given by

$$\begin{aligned} \psi(\theta,t+1/3) &= e^{i\hbar_{\rm eff}\partial_\theta^2/6}\, \psi(\theta,t) \\ &= \frac{1}{\sqrt{2\pi}} \sum_{n=-\infty}^{\infty} A_n(t)\, e^{-i\hbar_{\rm eff}n^2/6}\, e^{in\theta} \,. \end{aligned} \tag{4.39}$$

At resonance condition $\hbar_{\rm eff} = 2\pi r/M$, by introducing

$$n = m + 3lM \,, \tag{4.40a}$$

$$m = 0,1,\cdots,3M-1 \,, \tag{4.40b}$$

$$l = \cdots,-1,0,1,\cdots \,, \tag{4.40c}$$

we arrive at

$$\psi(\theta,t+1/3) = \frac{1}{\sqrt{2\pi}} \sum_{m=0}^{3M-1} \sum_{l=-\infty}^{\infty} A_{m+3lM}(t)\, e^{-i\pi r m^2/3M}\, e^{i(m+3lM)\theta} \,, \tag{4.41}$$

provided M to be an even integer. The choice of r being an odd integer guarantees that $\hbar_{\rm eff}/2\pi$ is an irreducible rational number. Substituting the Fourier coefficients from Eq. (4.38) in Eq. (4.41), we obtain

$$\begin{aligned} \psi(\theta,t+1/3) = \frac{1}{2\pi} \sum_{m=0}^{3M-1} e^{-i\pi r m^2/3M} \int_0^{2\pi} d\theta' \psi(\theta',t)\, e^{im(\theta-\theta')} \\ \times \left[\sum_{l=-\infty}^{\infty} e^{i3lM(\theta-\theta')} \right]. \end{aligned} \tag{4.42}$$

Using the Poisson summation formula

$$\sum_{l=-\infty}^{\infty} e^{i3lM(\theta-\theta')} = \frac{2\pi}{3M} \sum_{l=-\infty}^{\infty} \delta\left(\theta-\theta'+\frac{2\pi l}{3M}\right) , \tag{4.43}$$

and taking into account that system is periodic in the angular direction, we can write

$$\psi(\theta,t+1/3) = \frac{1}{3M} \sum_{m=0}^{3M-1} \sum_{l=0}^{3M-1} e^{-i\pi r m^2/3M}\, e^{-i2\pi ml/3M}\, \psi\left(\theta+\frac{2\pi}{3M}l,t\right) . \tag{4.44}$$

To derive Eq. (4.9), we make use of the change $\theta \to \theta + (2\pi/3M)\, n$, thus

$$\begin{aligned} \psi\left(\theta+\frac{2\pi}{3M}n,t+1/3\right) = \frac{1}{3M} \sum_{m,n'=0}^{3M-1} \exp\left(-i\frac{\pi r}{3M}m^2\right) \\ \times \exp\left(-i\frac{2\pi}{3M}m(n'-n)\right)\, \psi\left(\theta+\frac{2\pi}{3M}n',t\right) . \end{aligned} \tag{4.45}$$

For $r = 3$, the summation over m can be implemented as follows

$$\begin{aligned} \sum_{m=0}^{3M-1} e^{-i\pi m^2/M}\, e^{-i2\pi ml/3M} &= \left[\sum_{m=1}^{M-1} + \sum_{m=M}^{2M-1} + \sum_{m=2M}^{3M-1}\right] e^{-i\pi m^2/M}\, e^{-i2\pi ml/3M} \\ &= \sum_{m=1}^{M-1} e^{-i\pi m^2/M}\, e^{-i2\pi ml/3M} \\ &\quad \times \left[1+e^{-i2\pi l/3}+e^{-i4\pi l/3}\right] , \end{aligned} \tag{4.46}$$

with $n'-n = l$ being fixed. Geometrically, one can show that

$$1+e^{-i2\pi l/3}+e^{-i4\pi l/3} = \begin{cases} 3 & \text{if mod}(l,3)=0 \\ 0 & \text{otherwise} \end{cases} . \tag{4.47}$$

This completes the derivation of Eq. (4.10).

4.B Classical map

Here we derive the classical map that is associated with the quantum mechanical Floquet operator of the kicked rotator with broken TRS. We consider separately the three-kick and one-kick representation.

4.B.1 Three-kick representation

We seek the classical limit of the Floquet operator (4.14). We consider the classical motion from θ_0 at $t=0$ to θ_T at $t=T$ (in units of τ_0). Intermediate values of the coordinate are denoted by θ_t, $t=0,1,...,T$. The classical action $\mathcal{S}$ is the sum

$$\mathcal{S} = \sum_{t=0}^{T-1} S(\theta_{t+1},\theta_t). \tag{4.48}$$

Following the general method of Ref. [7] we derive

$$S(\theta',\theta) = S_c(\theta',\theta_2) + S_b(\theta_2,\theta_1) + S_a(\theta_1,\theta), \tag{4.49}$$

$$\begin{aligned}
S_a(\theta_1,\theta) &= \tfrac{3}{2}(\theta_1-\theta+2\pi\sigma_{\theta_1})^2 - 6\pi\sigma_{p_1}\theta_1 \\
&\quad + \gamma\cos(\theta_1) - \tfrac{1}{2}V(\theta), && (4.50)\\
S_b(\theta_2,\theta_1) &= \tfrac{3}{2}(\theta_2-\theta_1+2\pi\sigma_{\theta_2})^2 - 6\pi\sigma_{p_2}\theta_2, && (4.51)\\
S_c(\theta',\theta_2) &= \tfrac{3}{2}(\theta'-\theta_2+2\pi\sigma_{\theta'})^2 - 6\pi\sigma_{p'}\theta' \\
&\quad - \gamma\cos(\theta_2) - \tfrac{1}{2}V(\theta). && (4.52)
\end{aligned}$$

The integers σ_θ, σ_p are the winding numbers of a classical trajectory on a torus with $\theta \in [0,2\pi)$ and $p \in [0,6\pi)$. The map equations are derived from

$$\begin{aligned}
p_1 &= \frac{\partial}{\partial\theta_1}S_a(\theta_1,\theta), \quad p = -\frac{\partial}{\partial\theta}S_a(\theta_1,\theta), && (4.53)\\
p_2 &= \frac{\partial}{\partial\theta_2}S_b(\theta_2,\theta_1), \quad p_1 = -\frac{\partial}{\partial\theta_1}S_b(\theta_2,\theta_1), && (4.54)\\
p' &= \frac{\partial}{\partial\theta'}S_c(\theta',\theta_2), \quad p_2 = -\frac{\partial}{\partial\theta_2}S_c(\theta',\theta_2). && (4.55)
\end{aligned}$$

Eqs. (4.53-4.55) are equivalent to the following set of 6 equations that map initial coordinates (θ, p) onto final coordinates (θ', p') after one period:

$$\begin{cases} \theta_1 = \theta + p/3 - V'(\theta)/6 - 2\pi\sigma_{\theta_1}, \\ p_1 = p - \gamma\sin\theta_1 - V'(\theta)/2 - 6\pi\sigma_{p_1}, \end{cases} \tag{4.56}$$

$$\begin{cases} \theta_2 = \theta_1 + p_1/3 - 2\pi\sigma_{\theta_2}, \\ p_2 = p_1 - 6\pi\sigma_{p_2}, \end{cases} \tag{4.57}$$

$$\begin{cases} \theta' = \theta_2 + p_2/3 + \gamma\sin\theta_2/3 - 2\pi\sigma_{\theta'}, \\ p' = p_2 + \gamma\sin\theta_2 - V'(\theta')/2 - 6\pi\sigma_{p'}. \end{cases} \tag{4.58}$$

We denote $V' = dV/d\theta$. Winding numbers of a trajectory on the torus in phase space (θ, p) are denoted by σ_θ, σ_p. These integers are determined by the requirement that $\theta, \theta_1, \theta_2, \theta' \in [0, 2\pi)$ and $p, p_1, p_2, p' \in [0, 6\pi)$. TRS for a classical map means that the point $(\theta', -p')$ maps to $(\theta, -p)$. This property is satisfied for $\gamma = 0$, but not for $\gamma \neq 0$. TRS is broken at the classical level in the three-kick model.

4.B.2 One-kick representation

We now seek the classical limit of the Floquet operator (4.16). The classical action S after one kick is

$$\begin{aligned} S(\theta', \theta) &= \tfrac{1}{2}(\theta' - \theta + 2\pi\sigma_\theta)^2 - 2\pi\sigma_p\theta' \\ &\quad + \delta(\theta' - \theta + 2\pi\sigma_\theta) \\ &\quad - \tfrac{1}{2}K[\cos(\theta + \phi) + \cos(\theta' + \phi)]. \end{aligned} \tag{4.59}$$

The map equations are derived from

$$p' = \frac{\partial}{\partial\theta'} S(\theta', \theta), \quad p = -\frac{\partial}{\partial\theta} S(\theta', \theta). \tag{4.60}$$

The mapping of initial coordinates (θ, p) onto final ones (θ', p') after one kick is then

$$\left\{ \begin{array}{rcl} \theta' &=& \theta + p + \tfrac{1}{2}K\sin(\theta + \phi) - \delta - 2\pi\sigma_\theta, \\ p' &=& p + \tfrac{1}{2}K[\sin(\theta + \phi) + \sin(\theta' + \phi)] - 2\pi\sigma_p. \end{array} \right. \tag{4.61}$$

The canonical transformation $p - \delta \to \tilde{p}$, $\theta + \phi \to \tilde{\theta}$ brings the map to an equivalent form

$$\left\{ \begin{array}{rcl} \tilde{\theta}' &=& \tilde{\theta} + \tilde{p} + \tfrac{1}{2}K\sin\tilde{\theta} - 2\pi\sigma_\theta, \\ \tilde{p}' &=& \tilde{p} + \tfrac{1}{2}K(\sin\tilde{\theta} + \sin\tilde{\theta}') - 2\pi\sigma_p. \end{array} \right. \tag{4.62}$$

This form is manifestly invariant under the transformation that maps $(\tilde{\theta}', -\tilde{p}')$ onto $(\tilde{\theta}, -\tilde{p})$ for any value of ϕ and δ. Hence TRS is not broken at the classical level in the one-kick model.

4.C Derivation of Eqs. (4.28) and (4.29)

In the large-K limit the level curvature in the kicked rotator can be related to the level curvature in the Pandey-Mehta Hamiltonian. This leads to the relations (4.28) and (4.29) between the TRS breaking parameters γ (three-kick model) and

δ (one-kick model), on the one hand, and the Pandey-Mehta parameter α, on the other hand.

Perturbation theory for eigenphases $\phi_i(\delta\gamma)$ of a unitary matrix $\mathcal{F}(\delta\gamma)$ gives the series expansion

$$\begin{aligned}\phi_i(\delta\gamma) &= \phi_i + W_{ii}\delta\gamma + \tfrac{1}{2}\textstyle\sum_{j\neq i}|W_{ij}|^2(\delta\gamma)^2\mathrm{cotan}\frac{\phi_i-\phi_j}{2} \\ &\quad + \tfrac{1}{2}V_{ii}(\delta\gamma)^2. \end{aligned} \tag{4.63}$$

Here ϕ_i denotes an eigenphase of $\mathcal{F}(0) = U\,\mathrm{diag}(e^{i\phi_1},\ldots,e^{i\phi_M})U^\dagger$. The Hermitian matrices W and V are defined by $W = U(-i\mathcal{F}^\dagger\partial_\gamma\mathcal{F}|_{\gamma=0})U^\dagger$, $V = \partial_\gamma W|_{\gamma=0}$. Due to reciprocity of $\mathcal{F}$ we find $W_{ii} = 0$. For the three-kick model (4.14) the operators W, V are

$$W = \frac{M}{6\pi}UX^\dagger\Pi^\dagger Y^\dagger\Pi^\dagger(-C\Pi + \Pi C)Y\Pi XU^\dagger, \tag{4.64}$$

$$V = i(\frac{M}{6\pi})^2UX^\dagger\Pi^\dagger Y^\dagger(C\Pi^\dagger C\Pi - \Pi^\dagger C\Pi C)Y\Pi XU^\dagger, \tag{4.65}$$

where $C_{mm'} = \delta_{mm'}\cos(2\pi m/M)$. We assume that for strongly chaotic systems ($K \gg 1$) the matrix elements W_{ij} and V_{ii} are random Gaussian numbers independent of the eigenphases. Average diagonal elements calculated in the three kick model at $\gamma = 0$ are $\langle V_{ii}\rangle = \mathrm{Tr}V/M = 0$ and $\langle W_{ii}\rangle = \mathrm{Tr}W/M = 0$. The variance of the off-diagonal elements is $\left\langle|W_{ij}|^2\right\rangle = \mathrm{Tr}WW^\dagger/M^2 = M/(6\pi)^2$.

For the one-kick model (4.16) the operators W, V are

$$W = UX^\dagger\tilde{U}^\dagger D\tilde{U}XU^\dagger, \quad V = -\frac{1}{2\pi}M, \tag{4.66}$$

with $D_{mm'} = \delta_{mm'}(m + 1/2 - M/2 - \delta M/2\pi)$. Average diagonal elements at $\delta = 0$ are $\langle V_{ii}\rangle = \mathrm{Tr}V/M = -M/2\pi$ and $\langle W_{ii}\rangle = \mathrm{Tr}W/M = 0$. The variance of the off-diagonal elements is $\left\langle|W_{ij}|^2\right\rangle = \mathrm{Tr}WW^\dagger/M^2 = M/12$.

For $K \gg 1$ the eigenphases ϕ_i are distributed randomly in the circular ensemble, which is locally equivalent to the Gaussian ensemble [1]. We expand Eq. (4.63) for small eigenphases difference, compare with Eq. (4.22) and substitute the variances of matrix elements calculated above. For the one-kick model we drop terms with V_{ii} as they are of order $1/M$. We finally arrive at Eqs. (4.28) and (4.29).

The explicit formula for the Pandey-Mehta parameter α describing the kicked rotator at large K is

$$\alpha\sqrt{M_{\mathrm{H}}} = \frac{\gamma M^{3/2}}{12\pi} \tag{4.67}$$

for the three-kick model. The corresponding formula for the one-kick model is

$$\alpha\sqrt{M_{\rm H}} = \frac{\delta M^{3/2}}{4\sqrt{3}}. \tag{4.68}$$

4.D Semiclassical derivation of the weak localization peak

We present a semiclassical derivation of the weak localization peak, adopting the method of Ref. [8] to the case of the kicked rotator. The method can not be used to determine the amplitude $\delta G(0)$, but we use it for the crossover scale. This serves as an independent check for the scaling predicted by RMT.

The action difference in the three-kick model for a pair of trajectories related by TRS is calculated as follows. The action $\mathcal{S}_0$ for a trajectory with initial coordinate θ_0 and final coordinate θ_T at $\gamma = 0$ is compared with the action $\mathcal{S}$ for a trajectory with the same initial and final coordinates, but at small γ. The result of linear expansion in γ is

$$\Delta S = \mathcal{S} - \mathcal{S}_0 = \gamma \sum_t [\cos\theta_1(t) - \cos\theta_2(t)], \tag{4.69}$$

where periods are numbered by $t = 0, 1, \ldots, T-1$ and $\theta_1(t), \theta_2(t)$ denote the coordinate of the particle when TRS-breaking kicks are applied.

The weak localization correction is

$$\delta G \propto \langle \exp(2i\,\Delta S/\hbar_{\rm eff}) \rangle\,, \tag{4.70}$$

where the average is taken with respect to all trajectories connecting initial to final coordinates. Approximating the distribution of the phase difference ΔS for a single step by a Gaussian, and taking the continuum limit of exponential dwell-time probability $P(t) \propto e^{-t/\tau_D}$, we derive

$$\delta G \propto [1 + (M\gamma/\gamma^*)^2]^{-1}, \quad (\gamma^*)^2 = 2\hbar_{\rm eff}^2/(\tau_D \nu), \tag{4.71}$$

with ν being the variance of $\Delta S/\gamma$ for a single step. The result $\nu = 1$ for large K (and large τ_D) is obtained by averaging over random initial points in the whole phase space. We thus find Eq. (4.35), the same result as the one obtained in RMT.

The action difference for a pair of symmetry related trajectories in the one-kick model is

$$\Delta S = \mathcal{S} - \mathcal{S}_0 = \delta \sum_t [\theta'(t) - \theta(t) + 2\pi\sigma_\theta(t)], \tag{4.72}$$

to linear order in δ. This leads to

$$\delta G \propto [1 + (M\delta/\delta^*)^2]^{-1}, \quad (\delta^*)^2 = 2\hbar_{\rm eff}^2/(\tau_D \nu). \tag{4.73}$$

By averaging over random initial points in the whole phase space for large K and τ_D we find $\nu = 4\pi^2/3$. Hence we obtain Eq. (4.36), the result of RMT.

Bibliography

[1] F. Haake, *Quantum Signatures of Chaos* (Springer, Berlin, 1992).

[2] C. W. J. Beenakker, Rev. Mod. Phys. **69**, 731 (1997).

[3] T. Guhr, A. Müller-Groeling, and H. A. Weidenmüller, Phys. Rep. **299**, 190 (1998).

[4] Y. Alhassid, Rev. Mod. Phys. **72**, 895 (2000).

[5] O. Bohigas, M. G. Giannoni, A. M. Ozorio de Almeida, and C. Schmit, Nonlinearity **8**, 203 (1995).

[6] Z. D. Yan and R. Harris, Europhys. Lett. **32**, 437 (1995).

[7] P. Shukla and A. Pandey, Nonlinearity **10**, 979 (1997).

[8] H. U. Baranger, R. A. Jalabert, and A. D. Stone, Phys. Rev. Lett. **70**, 3876 (1993); Chaos **3**, 665 (1993).

[9] Z. Pluhar, H. A. Weidenmüller, J. A. Zuk, and C. H. Lewenkopf, Phys. Rev. Lett. **73**, 2115 (1994).

[10] K. B. Efetov, Phys. Rev. Lett. **74**, 2299 (1995).

[11] K. Frahm, Europhys. Lett. **30**, 457 (1995); K. Frahm and J.-L. Pichard, J. Phys. I **5**, 847 (1995).

[12] Y. V. Fyodorov and H. -J. Sommers, JETP Lett. **72**, 422 (2000).

[13] A. Ossipov, T. Kottos, and T. Geisel, Europhys. Lett. **62**, 719 (2003).

[14] Ph. Jacquod, H. Schomerus, and C.W.J. Beenakker, Phys. Rev. Lett. **90**, 207004 (2003).

[15] J. Tworzydło, A. Tajic, H. Schomerus, and C. W. J. Beenakker, Phys. Rev. B **68**, 115313 (2003).

[16] F. M. Izrailev, Phys. Rev. Lett. **56**, 541 (1986).

[17] F. M. Izrailev, Phys. Rep. **196**, 299 (1990).

[18] R. Blümel and U. Smilansky, Phys. Rev. Lett. **69**, 217 (1992).

[19] M. Thaha, R. Blümel, and U. Smilansky, Phys. Rev. E **48**, 1764 (1993).

[20] T. O. de Carvalho, J. P. Keating, and J. M. Robbins, J. Phys. A **31**, 5631 (1998).

[21] T. Dittrich, R. Ketzmeric, M.-F. Otto, and H. Schanz, Ann. Phys. (Leipzig) **9**, 755 (2000).

[22] P. H. Jones, M. Goonasekera, H. E. Saunders-Singer, and D. R. Meacher, quant-ph/0309149.

[23] T. Jonckheere, M. R. Isherwood, and T. S. Monteiro, Phys. Rev. Lett. **91**, 253003 (2003).

[24] G. Casati, R. Graham, I. Guarneri, and F. M. Izrailev, Phys. Lett. A **190**, 159 (1994).

[25] T. Kottos, A. Ossipov, and T. Geisel, Phys. Rev. E **68**, 066215 (2003).

[26] P. Shukla, Phys. Rev. E **53**, 1362 (1996).

[27] M. C. Goorden and Ph. Jacquod (private communication).

[28] M. L. Mehta and A. Pandey, J. Phys. A **16**, 2655 (1983).

[29] J. Tworzydło, A. Tajic, and C. W. J. Beenakker, Phys. Rev. B **69**, 165318 (2004).

[30] Ph. Jacquod and E. V. Sukhorukov, Phys. Rev. Lett. **92**, 116801 (2004).

[31] P. G. Silvestrov, M. C. Goorden, and C. W. J. Beenakker, Phys. Rev. Lett. **90**, 116801 (2003); Phys. Rev. B **67**, 241301 (2003).

[32] I. L. Aleiner and A. I. Larkin, Phys. Rev. B **54**, 14423 (1996).

[33] I. Adagideli, Phys. Rev. B **68**, 233308 (2003).

Chapter 5

Exponential sensitivity to dephasing of electrical conduction through a quantum dot

An instructive way to classify quantum interference effects in mesoscopic conductors is to ask whether they depend exponentially or algebraically on the dephasing time τ_ϕ. The Aharonov-Bohm effect is of the former class, while weak localization (WL) and universal conductance fluctuations (UCF) are of the latter class [1, 2]. It is easy enough to understand the difference: On the one hand, Aharonov-Bohm oscillations in the magnetoconductance of a ring require phase coherence for a certain minimal time $t_{\min}$ (the time it takes to circulate once along the ring), which becomes exponentially improbable if $\tau_\phi < t_{\min}$. On the other hand, WL and UCF in a disordered quantum dot originate from multiple scattering on a broad range of time scales, not limited from below, and the superposition of exponents with a range of decay rates amounts to a power law decay.

In a seminal paper [3], Aleiner and Larkin have argued that ballistic chaotic quantum dots are in a class of their own. In these systems the Ehrenfest time τ_E introduces a lower limiting time scale for the interference effects, which are exponentially suppressed if $\tau_\phi < \tau_E$. The physical picture is that electron wave packets in a chaotic system can be described by a single classical trajectory for a time up to τ_E [4]. Both WL and UCF, however, require that a wave packet splits into partial waves which follow different trajectories before interfering. Only the fraction $\exp(-\tau_E/\tau_\phi)$ of electrons which have not yet dephased at time τ_E can therefore contribute to WL and UCF.

The WL correction $\delta G = \langle G \rangle - G_{\rm cl}$ is the deviation of the ensemble averaged conductance $\langle G \rangle$ (in zero magnetic field) from the classical value $G_{\rm cl} = N/2$. (We measure conductances in units of $2e^2/h$ and assume an equal number of modes $N \gg 1$ in the two leads that connect the quantum dot to electron reservoirs.) The WL correction according to random-matrix theory (RMT),

$$\delta G_{\rm RMT} = -\tfrac{1}{4}(1 + \tau_D/\tau_\phi)^{-1}, \tag{5.1}$$

has a power law suppression $\propto \tau_\phi/\tau_D$ when τ_ϕ becomes smaller than the mean dwell time τ_D in the quantum dot [5]. Similarly, RMT predicts for the UCF a power law suppression $\propto (\tau_\phi/\tau_D)^2$ of the mean-squared sample-to-sample conductance fluctuations [5,6],

$$\mathrm{Var}\, G_{\rm RMT} = \frac{1}{8\beta}(1 + \tau_D/\tau_\phi)^{-2}, \tag{5.2}$$

with $\beta = 2$ (1) in the presence (absence) of a time-reversal-symmetry-breaking magnetic field.

Aleiner and Larkin have calculated the τ_E-dependence of the WL correction, with the result [3]

$$\delta G = e^{-\tau_E/\tau_\phi} e^{-2\tau_E/\tau_D}\, \delta G_{\rm RMT}. \tag{5.3}$$

The two exponential suppression factors in Eq. (5.3) result from the absence of interfering trajectories for times below τ_E. The first factor $\exp(-\tau_E/\tau_\phi)$ accounts for the loss by dephasing and the second factor $\exp(-2\tau_E/\tau_D)$ accounts for the loss by escape into one of the two leads. The UCF are expected to be suppressed similarly.

The physical picture presented by Aleiner and Larkin is simple and supported by two independent calculations [3, 7]. And yet, it has been questioned as a result of some very recent computer simulations of UCF [8, 9] and WL [10] in the absence of dephasing. The expected exponential reduction of quantum interference effects due to escape into the leads was not observed. In fact, both WL and UCF were found to be completely independent of τ_E, even though the simulations extended to system sizes for which τ_E was well above τ_D. To explain these negative results, Jacquod and Sukhorukov [8] invoked the *effective* RMT of Silvestrov et al. [11]. In that approach the electrons with dwell times $> \tau_E$ are described by RMT with an effective number $N_{\rm eff} = N \exp(-\tau_E/\tau_D)$ of modes. Then no τ_E-dependence is expected as long as $N_{\rm eff} \gg 1$ — even if $\tau_E \gg \tau_D$.

Since the predicted exponential reduction factor due to escape into the leads has not appeared in the simulations, it is natural to ask about the factor $\propto \exp(-\tau_E/\tau_\phi)$ due to dephasing. Does it exist? An experimental study of two-dimensional

(2D) weak localization has concluded that it does [12], but since leads play no role in 2D these experiments can not really resolve the issue. In the absence of experiments on the zero-dimensional geometry of a quantum dot, we have used computer simulations to provide an answer. We find that a relatively small amount of dephasing is sufficient to introduce a marked τ_E-dependence of the UCF. Our observation can be explained by incorporating dephasing into the effective RMT. We find that

$$\delta G = e^{-\tau_E/\tau_\phi}\ \delta G_{\rm RMT}, \tag{5.4}$$

$$\mathrm{Var}\, G = e^{-2\tau_E/\tau_\phi}\ \mathrm{Var}\, G_{\rm RMT}, \tag{5.5}$$

and show that Eq. (5.5) provides a fitting-parameter-free description of the numerical data.

We have introduced a dephasing lead [13] in the kicked rotator, which is the same dynamical system studied in Refs. [8–10, 14] in the absence of dephasing. The kicked rotator provides a stroboscopic description of chaotic scattering in a quantum dot [15], in the sense that the wave function is determined only at times which are multiples of a time τ_0 (which we set to unity). The mean dwell time $\tau_D = M/2N = \pi/N\delta$ is the ratio of the dimension M of the Floquet matrix (corresponding to a mean level spacing $\delta = 2\pi/M$) and the dimension $2N$ of the scattering matrix (without the dephasing lead). The kicking strength $K = 7.5$ determines the Lyapunov exponent $\lambda = \ln(K/2) = 1.32$. The Ehrenfest time is given by [16, 17]

$$\tau_E = \begin{cases} \lambda^{-1}\ln(N^2/M) & \text{if } N > \sqrt{M}, \\ 0 & \text{if } N < \sqrt{M}. \end{cases} \tag{5.6}$$

The dephasing lead increases the dimension of the scattering matrix S to $M \times M$. It has the block form

$$S = \begin{pmatrix} s_{00} & s_{01} & s_{02} \\ s_{10} & s_{11} & s_{12} \\ s_{20} & s_{21} & s_{22} \end{pmatrix}, \tag{5.7}$$

where the subscripts $1, 2$ label the two real leads and 0 labels the dephasing lead. The two real N-mode leads are coupled ballistically to the system, while the remaining $M - 2N$ modes are coupled via a tunnel barrier. The dephasing rate $1/\tau_\phi = \Gamma(1 - 2N/M)$ is proportional to the tunnel probability Γ per mode. The dephasing lead is connected to an electron reservoir at a voltage which is adjusted

so that no current is drawn. The conductance G is then determined by the coefficients $G_{ij} = \mathrm{Tr}\, s_{ij} s_{ij}^\dagger$ through Büttiker's formula [13],

$$\begin{aligned} G &= G_{12} + \frac{G_{10} G_{02}}{G_{10} + G_{20}} \\ &= G_{12} + \frac{(N - G_{11} - G_{12})(N - G_{22} - G_{12})}{2N - G_{11} - G_{12} - G_{22} - G_{21}}. \end{aligned} \tag{5.8}$$

.

For $\Gamma \ll 1$ the dephasing lead model is equivalent to the imaginary energy model of dephasing [5], which is the model used by Aleiner and Larkin [3]. (We will also make use of this equivalent representation later on.) There exist other models of dephasing in quantum transport [18, 19], but for a comparison with Ref. [3] our choice seems most appropriate.

Since we need a relatively small Lyapunov exponent in order to reach a large enough Ehrenfest time, our simulations are sensitive to short non-ergodic trajectories. These introduce an undesired dependence of the data on the position of the leads. Preliminary investigations indicated that UCF in a magnetic field was least sensitive to the lead positions, so we concentrate on that quantum interference effect in the numerics. The variance $\mathrm{Var}\, G$ of the conductance was calculated in an ensemble created by sampling 40 values of the quasi-energy. To determine the dependence on the lead positions we repeated the calculation for 40 different configurations of the leads. Error bars in the plots give the spread of the data.

There are four time scales in the problem: λ^{-1}, τ_D, τ_ϕ, and τ_E. To isolate the τ_E dependence we increase both M and N at constant ratio M/N and fixed K, Γ. Then only τ_E varies. Results are shown in Fig. 5.1. The variance of the conductance is divided by the RMT prediction (5.2), with $\beta = 2$ because of broken time-reversal symmetry. [1] We see that for $\tau_\phi \gg \tau_E$ there is no systematic dependence of UCF on the Ehrenfest time, consistent with Refs. [8, 9]. However, an unambiguous τ_E-dependence appears for $\tau_\phi \lesssim \tau_E$, regardless of whether τ_ϕ is smaller or larger than τ_D.

To explain the data in Fig. 5.2 we introduce dephasing into the effective RMT. For that purpose it is more convenient to use an imaginary energy than a dephasing lead, so we first make the connection between these two equivalent representations. There exists an exact correspondence for any N [5], which requires a re-injection step to ensure current conservation. For the case $N \gg 1$ of interest here there is a simpler way.

[1] Time-reversal symmetry was broken by means of the one-kick Floquet operator of Ref. [10].

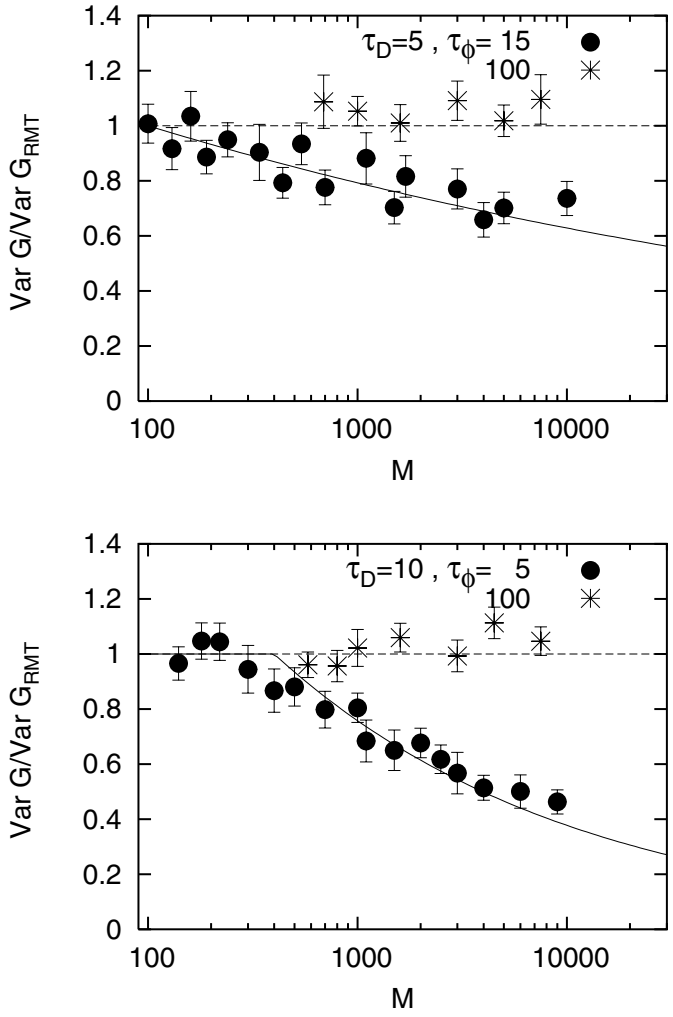

Figure 5.1: Variance of the conductance fluctuations, normalized by the RMT value (5.2), as a function of the dimension M of the scattering matrix of the kicked rotator with a dephasing lead. Each data set is for a fixed value of the dwell time $\tau_D = M/2N$ and dephasing time $\tau_\phi = \Gamma^{-1}(1-2N/M)^{-1}$. The Lyapunov exponent $\lambda = 1.32$ is kept the same for all data sets. The curves show the Ehrenfest time dependence (5.5) predicted by the effective RMT, without any fit parameter.

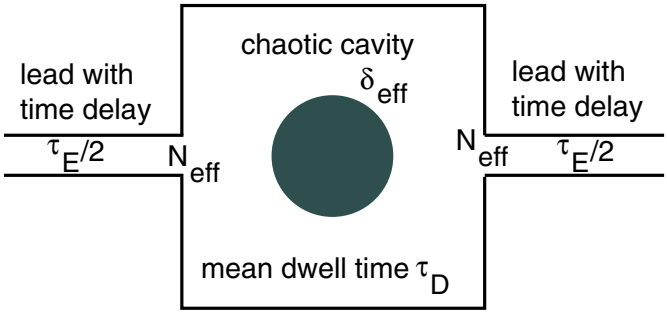

Figure 5.2: Pictorial representation of the effective RMT of a ballistic chaotic quantum dot. The part of phase space with dwell times $> \tau_E$ is represented by a fictitious chaotic cavity (mean level spacing $\delta_{\rm eff}$), connected to electron reservoirs by two long leads ($N_{\rm eff}$ propagating modes, one-way delay time $\tau_E/2$ for each mode). The effective parameters are determined by $N_{\rm eff}/N = \delta/\delta_{\rm eff} = \exp(-\tau_E/\tau_D)$. The scattering matrix of lead plus cavity is $\exp(iE\tau_E/\hbar)S_{\rm RMT}(E)$, with $S_{\rm RMT}(E)$ distributed according to RMT. A finite dephasing time τ_ϕ is introduced by the substitution $E \to E + i\hbar/2\tau_\phi$. The part of phase space with dwell times $< \tau_E$ has a classical scattering matrix, which does not contribute to quantum interference effects.

The coefficients $G_{ij} = G^{\rm cl}_{ij} + G^{\rm q}_{ij}$ in Eq. (5.8) consist of a classical contribution $G^{\rm cl}_{ij}$ of order N plus a (sample specific) quantum correction $G^{\rm q}_{ij}$ of order unity. The classical contribution is

$$G^{\rm cl}_{ij} = \tfrac{1}{2}N(1+\tau_D/\tau_\phi)^{-1}, \text{ for } i,j \in \{1,2\}. \tag{5.9}$$

Substitution into Eq. (5.8) gives a classical conductance $G_{\rm cl} = N/2$ independent of dephasing — as it should be. To leading order in N we obtain the quantum correction to the conductance,

$$G_{\rm q} = \tfrac{1}{4}(G_{12} + G_{21} - G_{11} - G_{22}). \tag{5.10}$$

(Notice that the classical contribution drops out of the right-hand-side.) For $\Gamma \ll 1$ the effect of the dephasing lead on the coefficients G_{ij} is equivalent to the addition of an imaginary part $i\hbar/2\tau_\phi$ to the energy. With the help of Eq. (5.10) we can compute the effect of dephasing on WL and UCF,

$$\delta G = \langle G_{\rm q}(E + i\hbar/2\tau_\phi)\rangle, \tag{5.11}$$

$$\mathrm{Var}\, G = \langle \left[G_{\rm q}(E + i\hbar/2\tau_\phi)\right]^2\rangle - (\delta G)^2, \tag{5.12}$$

by averaging the scattering matrix at a complex energy without having to enforce current conservation.

Effective RMT [11] is a phenomenological decomposition of the scattering matrix $S(t)$ in the time domain into a classical deterministic part $S_{\rm cl}$ for $t < \tau_E$ and a quantum part $S_{\rm q}$ with RMT statistics for $t > \tau_E$,

$$S(t) = \begin{cases} S_{\rm cl}(t) & \text{if } t < \tau_E, \\ S_{\rm q}(t) = S_{\rm RMT}(t - \tau_E) & \text{if } t > \tau_E. \end{cases} \tag{5.13}$$

The RMT part $S_{\rm q}$ couples to a reduced number $N_{\rm eff} = N \exp(-\tau_E/\tau_D)$ of channels in each lead. The mean dwell time in the quantum dot of these channels is $\tau_E + \tau_D$. The classical part $S_{\rm cl}$ couples to the remaining $2(N - N_{\rm eff})$ channels. (See Ref. [17] for an explicit construction of $S_{\rm cl}$.)

Only $S_{\rm q}$ contributes to $G_{\rm q}$. Fourier transformation to the energy domain gives

$$S_{\rm q}(E) = e^{iE\tau_E/\hbar} S_{\rm RMT}(E), \tag{5.14}$$

where we have used that $S_{\rm RMT}(t) = 0$ if $t < 0$. The matrix $S_{\rm RMT}$ has the RMT statistics of a fictitious chaotic cavity with zero Ehrenfest time, $N_{\rm eff}$ modes in each lead, and the same mean dwell time τ_D as the real cavity (see Fig. 5.2). For real energy the phase factor $\exp(iE\tau_E/\hbar)$ is irrelevant, hence all τ_E-dependence is hidden in $N_{\rm eff}$ and $\delta_{\rm eff}$. Since δG and $\mathrm{Var}\, G$ are independent of these two parameters, they are also independent of τ_E. The imaginary part $i\hbar/2\tau_\phi$ of the energy that represents the dephasing introduces a τ_E-dependence of $G_{\rm q} \propto \exp(-\tau_E/\tau_\phi)$. Insertion of this factor into Eqs. (5.11) and (5.12) yields the results (5.4) and (5.5) given in the introduction.

The curves in Fig. 5.1 follow from Eq. (5.5). They describe the simulation quite well — without any fit parameter. To test the agreement between simulation and effective RMT in a different way, we have collected all our data in Fig. 5.3 in a plot of $-(\tau_\phi/2)\ln(\mathrm{Var}\, G/\mathrm{Var}\, G_{\rm RMT})$ versus $\ln(N^2/M)$. According to Eq. (5.5) this should be a plot of τ_E versus $\ln(N^2/M)$, which in view of Eq. (5.6) is a straight line with slope $1/\lambda = 0.76$. There is considerable scatter of the data in Fig. 5.3, but the systematic parameter dependence is consistently described by the theory as N and M vary over two orders of magnitude.

In conclusion, our findings explain the puzzling difference in the outcome of previous experimental [12] and numerical [8–10] searches for the Ehrenfest time dependence of quantum interference effects in chaotic systems: The experiments found a dependence while the computer simulations found none. We have identified the absence of dephasing in the simulations as the origin of the difference. By

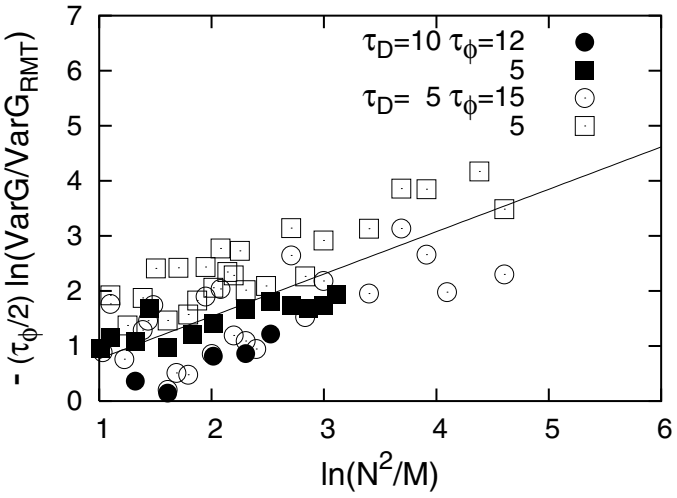

Figure 5.3: Four data sets of fixed τ_ϕ, τ_D, each consisting of a range of M between 10^2 and $2 \cdot 10^4$, plotted on a double-logarithmic scale. The solid line with slope $1/\lambda = 0.76$ is the scaling predicted by Eqs. (5.6) and (5.5).

introducing dephasing into the simulation we recover the exponential τ_E/τ_ϕ suppression factor predicted by Aleiner and Larkin [3]. The effective RMT explains why this suppression factor is observed while the exponential τ_E/τ_D suppression factor of Eq. (5.3) is not.

It remains an outstanding theoretical challenge to provide a microscopic foundation for the effective RMT, or alternatively, to derive Eqs. (5.4) and (5.5) from the quasiclassical theory of Refs. [3,7]. One might think that diffraction of a wave packet at the point contacts is the key ingredient which is presently missing from quasiclassics and which would eliminate the exponential τ_E/τ_D suppression factor from Eq. (5.3). However, our observation of an exponential τ_E/τ_ϕ suppression factor suggests otherwise: If diffraction at the edge of the point contacts were the dominant mechanism by which wave packets are split into partial waves, then the characteristic time scale for the suppression of quantum interference by dephasing would not be different from the mean dwell time τ_D.

Bibliography

[1] *Mesoscopic Phenomena in Solids*, edited by B. L. Altshuler, P. A. Lee, and R. A. Webb (Elsevier, Amsterdam, 1991).

[2] Y. Imry, *Introduction to Mesoscopic Physics* (Oxford University, Oxford, 2002).

[3] I. L. Aleiner and A. I. Larkin, Phys. Rev. B **54**, 14423 (1996); Chaos, Solitons & Fractals, **8**, 1179 (1997).

[4] G. M. Zaslavsky, Phys. Rep. **80**, 157 (1981).

[5] P. W. Brouwer and C. W. J. Beenakker, Phys. Rev. B **55**, 4695 (1997); **66**, 209901(E) (2002).

[6] H. U. Baranger and P. A. Mello, Phys. Rev. B **51**, 4703 (1995).

[7] I. Adagideli, Phys. Rev. B **68**, 233308 (2003).

[8] Ph. Jacquod and E. V. Sukhorukov, Phys. Rev. Lett. **92**, 116801 (2004).

[9] J. Tworzydło, A. Tajic, and C. W. J. Beenakker, Phys. Rev. B, **69**, 165318 (2004).

[10] J. Tworzydło, A. Tajic, and C. W. J. Beenakker, Phys. Rev. B **70**, 205324 (2004).

[11] P. G. Silvestrov, M. C. Goorden, and C. W. J. Beenakker, Phys. Rev. Lett. **90**, 116801 (2003). For a review, see C. W. J. Beenakker, cond-mat/0406018.

[12] O. Yevtushenko, G. Lütjering, D. Weiss, and K. Richter, Phys. Rev. Lett. **84**, 542 (2000).

[13] M. Büttiker, Phys. Rev. B **33**, 3020 (1986); IBM J. Res. Dev. **32**, 63 (1988).

[14] C. Tian, A. Kamenev, and A. Larkin, Phys. Rev. Lett. **93**, 124101 (2004).

[15] A. Ossipov, T. Kottos, and T. Geisel, Europhys. Lett. **62**, 719 (2003).

[16] M. G. Vavilov and A. I. Larkin, Phys. Rev. B **67**, 115335 (2003).

[17] P. G. Silvestrov, M. C. Goorden, and C. W. J. Beenakker, Phys. Rev. B **67**, 241301 (2003).

[18] F. Marquardt and C. Bruder, Phys. Rev. Lett. **92**, 056805 (2004); Phys. Rev. B **70**, 125305 (2004).

[19] A. A. Clerk and A. D. Stone, Phys. Rev. B **69**, 245303 (2004).

Chapter 6

Momentum noise in a quantum point contact

Not long after the discovery of conductance quantization in a ballistic constriction [1] it was predicted that the quantization is noiseless [2]: The time dependent current fluctuations should vanish at low temperatures on the plateaus of quantized conductance and they should peak in the transition from one plateau to the next. The conclusive experimental verification of this prediction followed many years later [3], delayed by the difficulty of eliminating extraneous sources of noise. The notion of noiseless quantum ballistic transport is now well established [4].

The origin of noiseless transport lies in the fact that the eigenvalues T_n of the transmission matrix product $tt^\dagger$ take only the values 0 or 1 on a conductance plateau. The current noise power at zero temperature $P_I \propto \sum_n T_n(1-T_n)$ then vanishes [5]. In other words, current fluctuations require partially filled scattering channels, which are incompatible with a quantized conductance.

In this chapter we point out that the notion of noiseless quantum ballistic transport does not apply if one considers momentum transfer instead of charge transfer. Momentum noise created by an electrical current (socalled electromechanical noise) has been studied in the tunneling regime [6] and in a diffusive conductor [7], but not yet in connection with ballistic transport. Our analysis is based on a recent scattering matrix representation of the momentum noise power P [8], according to which P depends not only on the transmission eigenvalues but also on the eigenvectors. This makes it possible for the electrons to generate noise even in the absence of partially filled scattering channels.

The geometry is shown schematically in Fig. 6.1. We consider a two-dimensional electron gas channel in the x-y plane. The width of the channel in the y-direction is W and the length in the x-direction is L. The channel contains a narrow constriction of length $\delta L \ll L$ and width $\delta W \ll W$ located at a distance L' from the left end. (We choose $x = 0$ at the middle of the constriction, so that the channel extends from $-L' < x < L - L'$.) A voltage V drives a current through the constriction, exciting a vibration of the channel. We seek the low-frequency noise power

$$P = 2\int_{-\infty}^{\infty} dt\, \overline{\delta F(0)\delta F(t)} = \lim_{t\to\infty} \frac{2}{t}\overline{\Delta \mathcal{P}(t)^2} \tag{6.1}$$

of the fluctuating force $\delta F(t) \equiv F(t) - \overline{F}$ that drives the vibration. The noise power is proportional to the variance of the momentum $\Delta\mathcal{P}(t)$ transferred by the electrons to the channel in a long time t.

We assume that the electron gas is deposited on top of a doubly clamped beam extended along the x axis and free to vibrate in the y direction. The solution of the wave equation is $\mathbf{u}(\mathbf{r},t) = \hat{y}u(x)\cos wt$, with w the mode frequency and $u(x)$ the mode profile. Both u and du/dx vanish at the ends of the beam and $u(x)$ is normalized such that it equals to 1 at the point x_0 at which the amplitude is measured [7]. We choose $x_0 = 0$ so that F corresponds to a point force at the location of the constriction.

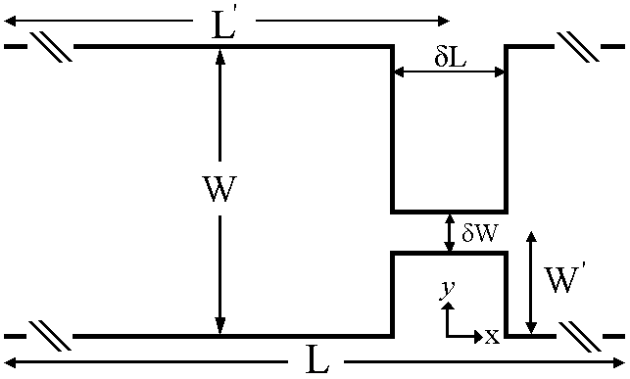

Figure 6.1: Schematic diagram of a two-dimensional channel containing a constriction. The current flows in the x-direction, the channel is free to vibrate either in the x-direction (longitudinal vibration) or in the y-direction (transverse vibration).

The wave functions are represented by scattering states. The incident wave has the form $\phi_n(\mathbf{r}) = |\hbar k_n/m^*|^{-1/2}\exp(ik_n x)\Phi_n(y)$, where m^* is the effective mass, $n = 1,2,\ldots N$ is the mode index, Φ_n the transverse wave function, and $k_n = \pm(2m^*/\hbar^2)^{1/2}(E_F - E_n)^{1/2}$ the longitudinal wave vector (at Fermi energy E_F larger than the cutoff energy E_n). We take k_n positive to the left and negative to the right of the constriction. Incident and outgoing waves are related by the $2N \times 2N$ unitary scattering matrix

$$S = \begin{pmatrix} r & t' \\ t & r' \end{pmatrix}, \tag{6.2}$$

containing the $N \times N$ transmission and reflection matrices t, t', r, r'. We assume time reversal symmetry, so that Φ_n is real and S is symmetric.

As derived in Ref. [8], the noise power P and the mean force $\overline{F}$ for a localized scatterer can be expressed in terms of the matrix S and a Hermitian matrix $\mathcal{M}_{nn'} = m^{*-1}\sum_{\alpha\beta}\langle n|p_\alpha u_{\alpha\beta} p_\beta|n'\rangle$ of expectation values in the basis of incident modes. The expectation value is taken of the electron momentum flux $m^{*-1}p_\alpha p_\beta$, weighted by the strain tensor $u_{\alpha\beta} = \frac{1}{2}(\partial u_\alpha/\partial x_\beta + \partial u_\beta/\partial x_\alpha)$. The matrix $\mathcal{M}$ is block-diagonal,

$$\mathcal{M} = \begin{pmatrix} M_{\rm L} & 0 \\ 0 & M_{\rm R} \end{pmatrix}. \tag{6.3}$$

At zero temperature and to first order in the voltage one has, for a two-fold spin degeneracy,

$$\begin{aligned} P &= \frac{4eV}{h}\mathrm{Tr}\left(rr^\dagger M_{\rm L}^* t t'^\dagger M_{\rm L}^* + r'r'^\dagger M_{\rm R}^* t t^\dagger M_{\rm R}^* \right. \\ &\quad \left. - 2tr^\dagger M_{\rm L}^* r t^\dagger M_{\rm R}^*\right), \end{aligned} \tag{6.4}$$

$$\overline{F} = \frac{2eV}{h}\mathrm{Tr}\left(M_{\rm L} + rr^\dagger M_{\rm L}^* + tt^\dagger M_{\rm R}^*\right). \tag{6.5}$$

In Eq. (6.5) we have not included the equilibrium contribution to the mean force (at $V = 0$). Electron-electron interactions (screening) are not accounted for, since we do not expect any appreciable charge accumulation in a ballistic system.

For a transverse vibration the blocks $M_{\rm L}, M_{\rm R}$ have elements

$$\begin{aligned} (M_{\rm L,R})_{nm} &= \frac{\hbar(k_n + k_m)}{2i|k_n k_m|^{1/2}}\int dy\,\Phi_n(y)\Phi'_m(y) \\ &\quad \times \int_{\rm L,R} dx\,u'(x)\exp[ix(k_m - k_n)]. \end{aligned} \tag{6.6}$$

The integral over x extends over the region $(-L', -\delta L/2)$ to the left of the constriction for $M_{\rm L}$ and over the region $(\delta L/2, L-L')$ to the right of the constriction for $M_{\rm R}$. We abbreviate $q_{nm} = k_m - k_n$. For $|n-m|$ of order unity one has q_{nm} of order $1/W$, so that the range of x that contributes to the integral is of order W. (Contributions from inside the constriction are smaller by a factor $\min(\delta W, \delta L)/W$.) Since W is much greater than the Fermi wave length λ_F, we are justified in using the asymptotic plane wave form of the scattering states to calculate $\mathcal{M}$.

We take hard-wall boundary conditions at $y = 0, W$, hence $\Phi_n(y) = (2/W)^{1/2} \sin(n\pi y/W)$, $E_n = (\hbar^2/2m^*)(n\pi/W)^2$, $N = [2W/\lambda_F]$, and $(k_n + k_m)q_{nm} = (\pi/W)^2(n^2 - m^2)$. The overlap $\int_0^W dy\, \Phi_n \Phi'_m$ is evaluated straightforwardly, but the integration over x requires more care. The derivative $u'(x)$ of the mode profile vanishes at the two clamped ends of the beam, as well as at its center. We assume that the constriction is off-center, therefore $u'(\pm\delta L/2) \approx u'(0) \neq 0$. We write $u'(0) = u_0/L$, with u_0 a number of order unity. Upon partial integration we find, to first order in W/L,

$$\begin{aligned}\int_{\rm L,R} dx\, u'(x) \exp(ixq_{nm}) = \;& \pm \;\frac{u_0}{iq_{nm}L} \exp(\mp iq_{nm}\delta L/2) \\ & + \;\mathcal{O}(W/L)^2. \end{aligned} \tag{6.7}$$

(The upper sign is for region L, the lower sign for region R.) We thus arrive for the transverse vibration at the result $M_L = -M_R \equiv M$, with

$$\begin{aligned} M_{nm} \;=\; & \frac{2\hbar W u_0}{\pi^2 L}(\sigma_{nm} - 1)\frac{nm(k_n + k_m)^2}{(n^2 - m^2)^2 |k_n k_m|^{1/2}} \\ & \times \exp\left[i\left(|k_n| - |k_m|\right)\delta L/2\right]. \end{aligned} \tag{6.8}$$

The symbol $\sigma_{nm} = \frac{1}{2}[1 + (-1)^{n+m}]$ selects indices of the same parity, so that $M_{nm} = 0$ if n and m are both even or both odd.

Our constriction has left-right symmetry, so $r = r'$ and $t = t'$. We contrast the case $W' = \frac{1}{2}W$ of axial symmetry with the case $W' \ll \frac{1}{2}W$ of a constriction placed highly off-axis. We also contrast the short-constriction case $\delta L \ll W$ (point contact geometry) with the long-constriction case $\delta L \gg W$ (microbridge geometry). The reflection and transmission matrices are calculated by matching wavefunction modes at $x = \pm\delta L/2$, cf. Ref. [9].

In Fig. 6.2 we show the dependence of the transverse noise power P [in units of $P_0 = (4eV/h)(Nu_0\hbar/L)^2$] on the width δW of the constriction, at fixed width W of the wide channel. (We choose $W = 49.9\lambda_F$, so $N = 99$.) The average transverse force $\overline{F}$ is shown in Fig. 6.3, normalized by $F_0 = (2eV/h)(Nu_0\hbar/L)$. (Note that $\overline{F} = 0$ for the axially symmetric case.) The conductance $G = (2e^2/h)\mathrm{Tr}\, tt^\dagger$

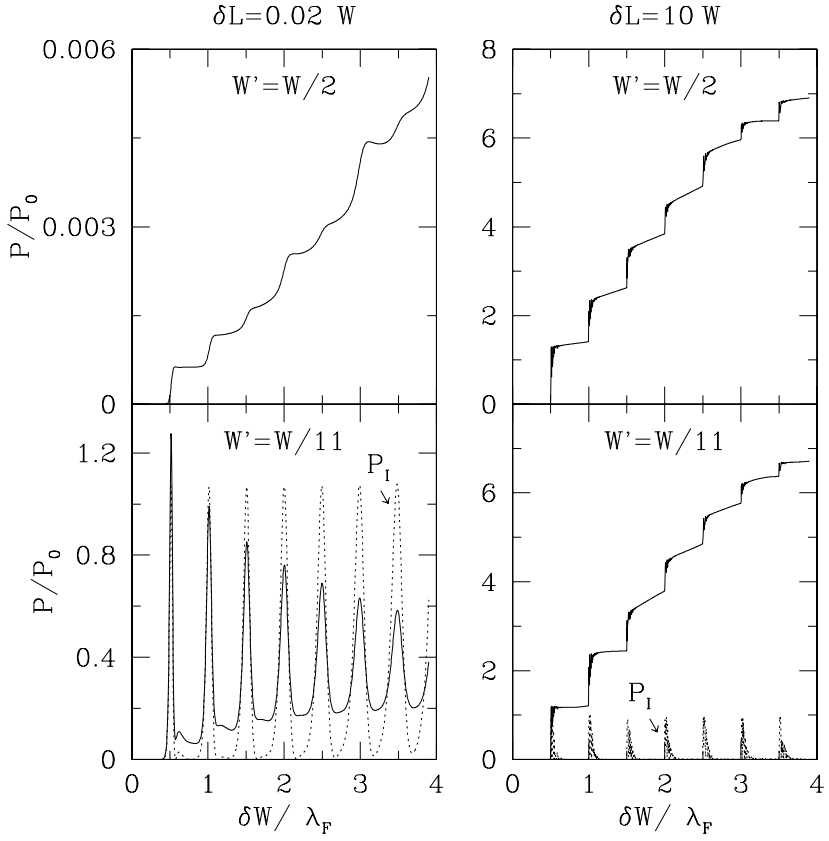

Figure 6.2: Solid lines: noise power P for transverse vibration versus width of constriction δW, at fixed width $W = 49.9\,\lambda_F$ of the wide channel. The left panels are for a short constriction with and without axial symmetry. The right panels are the corresponding results for a long constriction. The dotted line is the current noise P_I in units of e^3V/h (which is nearly the same with and without axial symmetry).

and the current noise $P_I = (4e^3V/h)\mathrm{Tr}\,tt^\dagger(1-tt^\dagger)$ are included in these plots for comparison.

The plots show a remarkably varied behavior: For the short constriction without axial symmetry the noise power P of the transverse force oscillates as a function of the constriction width δW, in much the same way as the current noise power P_I oscillates [2, 5]. However, the minima in P do not go to zero like

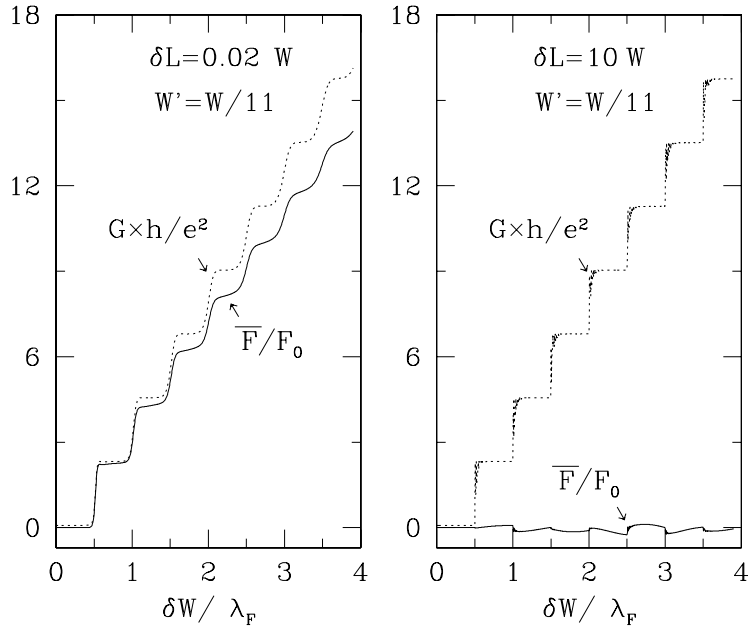

Figure 6.3: Solid lines: average transverse force as a function of constriction width, in the absence of axial symmetry (positive values point in the positive y-direction in the geometry of Fig. 6.1, for a current flowing in the positive x-direction). The left and right panels are for a short and long constriction, respectively. The conductance of the constriction is shown as a dotted line. The average transverse force is identically zero for the axially symmetric geometry ($W' = W/2$).

the minima in P_I, demonstrating non-zero momentum noise on the plateaus of quantized conductance. If the short constriction is precisely at the center of the channel, P increases nearly monotonically with δW. For a long constriction P increases nearly monotonically regardless of whether there is axial symmetry or not. The increase of the noise power is stepwise, reminiscent of the conductance. (The current noise in the long constriction remains oscillatory.) The mean transverse force behaves similarly to the conductance for the short constriction, but fluctuates around zero for the long constriction.

In order to explain the approximate quantization of momentum noise in analytical terms it is convenient to decompose the (symmetric) transmission matrix as $t_{nm} = \sum_{n'} U_{nn'} U_{mn'} \sqrt{T_{n'}}$, where U is an $N \times N$ unitary matrix and $T_n \in [0,1]$

is the transmission eigenvalue (eigenvalue of $tt^\dagger$). Similarly, the reflection matrix is decomposed as $r_{nm} = i\sum_{n'} U_{nn'}U_{mn'}\sqrt{1-T_{n'}}$. In this representation Eq. (6.4) takes the form

$$\begin{aligned} P &= \frac{8eV}{h}\sum_{n,m}|X_{nm}|^2\big[(1-T_n)T_m \\ &\quad + [T_n(1-T_n)T_m(1-T_m)]^{1/2}\big],\ X = U^\dagger M^* U. \end{aligned} \tag{6.9}$$

The matrix M couples only mode indices of different parity, cf. Eq. (6.8). The presence or absence of axial symmetry manifests itself in the matrix U, which couples only indices of the same parity if $W' = W/2$. In this axially symmetric case $X_{nm} = 0$ if n,m have the same parity.

In a simple model [10] of a long and narrow ballistic microbridge, U is a random matrix while the transmission eigenvalues take on only two values: $T_n = 1$ for $1 \le n \le \delta N$ and $T_n = 0$ for $\delta N < n \le N$. The number $\delta N = [2\delta W/\lambda_F]$ is the quantized conductance of the constriction (in units of $2e^2/h$). Averages of U over the unitary group introduce Kronecker delta's (cf. App. B in Ref. [10]). We need the average $\Omega_{pp'qq'nm} \equiv \langle U^*_{pn}U^*_{qm}U_{p'm}U_{q'n}\rangle$, given by

$$\Omega_{pp'qq'nm} = \frac{1}{N^2-1}\left(\delta_{pq'}\delta_{qp'} - \frac{1}{N}\delta_{pp'}\delta_{qq'}\right) \text{ if } n \ne m, \tag{6.10}$$

in the case of broken axial symmetry and

$$\Omega_{pp'qq'nm} = \frac{4}{N^2-\sigma_{N1}}\delta_{pq'}\delta_{qp'}\sigma_{pn}\sigma_{qm} \text{ if } \sigma_{nm} = 0, \tag{6.11}$$

in the axially symmetric case.

Substituting these values of T_n into Eq. (6.9) and averaging over U with the help of Eqs. (6.10) and (6.11), we find

$$\begin{aligned} P &= \frac{8eV}{h}\sum_{n=\delta N+1}^{N}\sum_{m=1}^{\delta N}\sum_{p,p',q,q'=1}^{N}\Omega_{pp'qq'nm}M^*_{pp'}M_{q'q} \\ &= \frac{8eV}{h}\frac{\delta N}{N}\left(1-\frac{\delta N}{N}\right)\mathrm{Tr}\,M^2 \\ &= \frac{\pi^2}{9}\delta N P_0,\ N \gg \delta N, \end{aligned} \tag{6.12}$$

regardless of whether axial symmetry is present or not. We thus obtain a stepwise increase of P as a function of δW with step height $\Delta P = (\pi^2/9)P_0$. The numerically obtained step height in Fig. 6.2 agrees within 10% with the analytical

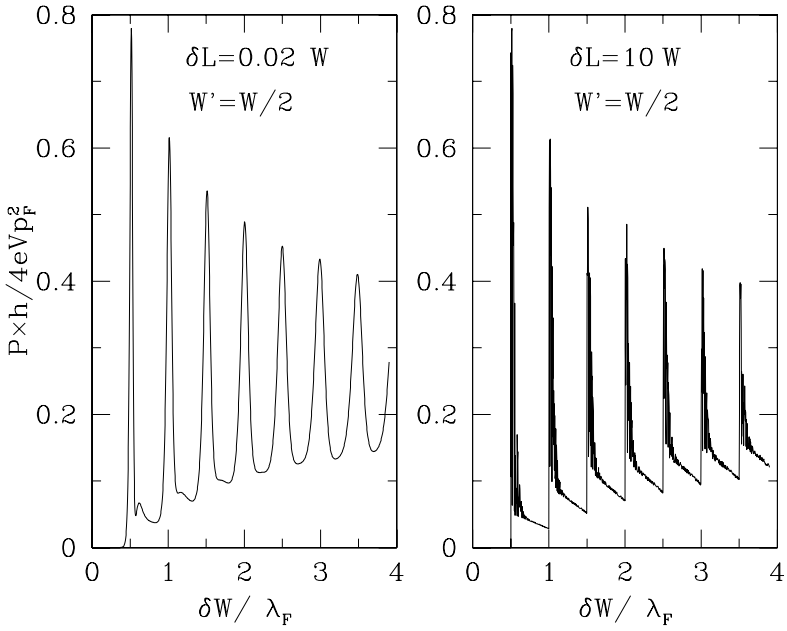

Figure 6.4: Noise power for longitudinal vibration of a short constriction (left panel) and a long constriction (right panel). These plots are for $W' = W/2$, but there is no noticeable dependence on the ratio W'/W. The mean longitudinal force (not shown) decreases stepwise as a function of δW in both the short and long constriction.

estimate for the first step. For subsequent steps the agreement becomes worse, presumably because the approximation of a uniform distribution of U breaks down as δW increases. We can also calculate the mean transverse force in the same way, starting from Eq. (6.5), and find $\overline{F} \propto \mathrm{Tr}\, M = 0$, in accordance with the numerical result that $\overline{F} \ll F_0$ for a long constriction.

In the short-constriction case $\delta L \ll W$ we may not treat U as uniformly distributed in the unitary group, and this has prevented us from finding a simple analytical representation of the numerical data.

This rich geometry dependence of the noise power is characteristic for a transverse vibration. For comparison we discuss the case of a longitudinal vibration, corresponding to a mode profile $\hat{x}\, u(x)$ oriented along the direction of the current through the constriction (instead of perpendicular to it). Such a longitudinal vibration corresponds to a compression mode of the beam, which is at a higher

frequency than the bending mode excited by a transverse vibration. For a longitudinal vibration the matrices M_L, M_R are diagonal: $(M_L)_{nm} = -(M_R)_{nm} = \delta_{nm}\hbar|k_n|u(0)$. We take $u(0) = 1$.

The noise power is plotted in Fig. 6.4 for both a long and a short constriction. It does not depend on the presence or absence of axial symmetry and is also rather insensitive to the length of the constriction. The order of magnitude of the longitudinal noise power is $(4eV/h)p_F^2$, with $p_F = \hbar k_F$ the Fermi momentum. This is larger than the typical transverse noise power P_0 by a factor of order $(k_F L/N)^2 \simeq (L/W)^2$. Inserting parameters $V = 1$ mV, $k_F = 10^8 m^{-1}$, typical for a two-dimensional electron gas, one estimates $(4eV/h)p_F^2 \simeq 10^{-40}$ N^2/Hz. This is below the force sensitivity of present day nanomechanical oscillators, but is hoped to be reached in future generations of these devices [11].

In summary, we have demonstrated that the momentum noise of ballistic electrons does not vanish on the plateaus of quantized conductance. Conductance quantization requires absence of backscattering in the constriction, but it does not preclude inter-mode scattering. Momentum noise makes this inter-mode scattering visible in a way that current noise can not. The dependence of the momentum noise on the constriction width was found to be remarkably varied, ranging from oscillatory to stepwise, depending on the direction of the vibration (longitudinal or transverse to the constriction), the presence or absence of axial symmetry, and the length of the constriction. The stepwise increase amounts to a quantum of momentum noise that might be observable with an ultrasensitive oscillator.

Bibliography

[1] B. J. van Wees, H. van Houten, C. W. J. Beenakker, J. G. Williamson, L. P. Kouwenhoven, D. van der Marel, and C. T. Foxton, Phys. Rev. Lett. **60**, 848 (1988); D. A. Wharam, T. J. Thornton, R. Newbury, M. Pepper, H. Ahmed, J. E. F. Frost, D. G. Hasko, D. C. Peacock, D. A. Ritchie, and G. A. C. Jones, J. Phys. C **21**, L209 (1988).

[2] G. B. Lesovik, JETP Lett. **49**, 592 (1989).

[3] M. I. Reznikov, M. Heiblum, H. Shtrikman, and D. Mahalu, Phys. Rev. Lett. **75**, 3340 (1995); A. Kumar, L. Saminadayar, D. C. Glattli, Y. Jin, and B. Etienne, Phys. Rev. Lett. **76**, 2778 (1996).

[4] Ya. M. Blanter and M. Büttiker, Phys. Rep. **336**, 1 (2000).

[5] M. Büttiker, Phys. Rev. Lett. **65**, 2901 (1990).

[6] M. F. Bocko, K. A. Stephenson, and R. H. Koch, Phys. Rev. Lett. **61**, 726 (1988); B. Yurke and G. P. Kochan- ski, Phys. Rev. B **41**, 8184 (1990).

[7] A. V. Shytov, L. S. Levitov, and C. W. J. Beenakker, Phys. Rev. Lett. **88**, 228303 (2002).

[8] M. Kindermann and C. W. J. Beenakker, Phys. Rev. B **66**, 224106 (2002).

[9] A. Szafer and A. D. Stone, Phys. Rev. Lett. **62**, 300 (1989).

[10] C. W. J. Beenakker, Rev. Mod. Phys. **69**, 731 (1997).

[11] M. Roukes, private communication.

Samenvatting

Volgens de klassieke mechanica bewegen deeltjes langs een welbepaalde baan, met een welbepaalde snelheid. Volgens de quantummechanica heeft deze baan een zekere onscherpte, die toeneemt naarmate de beweging langer voortduurt. Na een zekere tijd is de hele beweging dermate onscherp geworden dat we niet meer weten waar het deeltje zich in het systeem bevindt. Deze tijd heet de Ehrenfesttijd, genoemd naar de Leidse theoretisch natuurkundige Paul Ehrenfest. De Ehrenfesttijd τ_E wordt groter naarmate de quantummechanische golflengte λ van het deeltje kleiner wordt, maar de toename is heel langzaam, namelijk evenredig met de logaritme van de verhouding L/λ (waarbij L de afmeting is van het systeem). Dit maakt het bijzonder moeilijk om de overgang van de quantummechanica naar de klassieke mechanica te bestuderen in een computersimulatie. Om τ_E te verdubbelen is het nodig om het systeem tien keer zo groot te maken en nog een verdubbeling is dan nauwelijks haalbaar.

In dit proefschrift onderzoeken we een bijzonder efficiënte rekenmethode, die het mogelijk maakt om uitzonderlijk grote systemen te bestuderen. Het is een stroboscopische methode, hetgeen wil zeggen dat de beweging van het deeltje niet continu gevolgd wordt, maar slechts met tussenpozen van een bepaalde periode, zoals in een stroboscoop. We passen deze methode toe op elektronen in een "quantum dot". Dit systeem valt nog het best te vergelijken met een biljart. Het wordt gemaakt in een tweedimensionaal elektronengas, geheel zonder verontreinigingen, zodat de elektronen rechtlijnig bewegen en alleen botsen met de wanden van het biljart. De typische afmeting van zo'n quantum dot is 1 micrometer. De vorm van het biljart is onregelmatig, zodat de beweging chaotisch is. Dat wil zeggen, dat je na een aantal botsingen met de wand niet meer goed kunt voorspellen waar een elektron terecht zal komen. Daarom is het niet goed mogelijk om de beweging met pen en papier door te rekenen en biedt een computersimulatie uitkomst.

In het laboratorium wordt aan een quantum dot gemeten door er twee openingen in te maken en daar vervolgens een elektrische stroom doorheen te sturen.

Wij bootsen zulk een meting na op de computer door elektronen via de ene opening naar binnen te schieten en bij te houden welke fractie via de andere opening weer naar buiten komt. Deze fractie heet de transmissiekans. Zij is direkt gerelateerd aan het geleidingsvermogen G van de quantum dot (zijnde de verhouding van stroom en spanningsverschil). Volgens de klassieke mechanica zou die kans in een chaotisch biljart gelijk moeten zijn aan 1/2. Volgens de quantummechanica, echter, is de transmissiekans iets kleiner dan 1/2. Dit verschijnsel heet zwakke localisatie en de afwijking van 1/2 heet de zwakke localisatie correctie, aangeduid door δG. In de literatuur was voorspelt dat de zwakke localisatie correctie zou verdwijnen als de Ehrenfesttijd τ_E langer zou worden dan de gemiddelde verblijftijd τ_D van een elektron in de quantum dot, en wel op exponentiële wijze: $\delta G \propto \exp(-\tau_E/\tau_D)$. Onze computersimulaties hebben aangetoond dat deze voorspelling onjuist is: de zwakke localisatiecorrectie is zo goed als onafhankelijk van de verhouding τ_E/τ_D. Om dit te verklaren hebben we gebruik gemaakt van de toevalsmatrixtheorie die in de Leidse onderzoeksgroep is ontwikkeld.

De computersimulatie in zijn eenvoudigste vorm bootst een systeem na op het absolute nulpunt van temperatuur. Omdat experimenten natuurlijk nooit precies bij temperatuur nul worden uitgevoerd, is het belangrijk om dit in rekening te brengen. Het belangrijkste gevolg van de temperatuur is dat er een nieuwe tijdschaal een rol gaat spelen, de decoherentietijd τ_ϕ. De quantummechanische interferentie die verantwoordelijk is voor het zwakke localisatie-effect kan alleen optreden tussen paden die korter duren dan τ_ϕ. Door dit in rekening te brengen in onze computersimulatie, vinden we dat er nu wel degelijk een exponentiële afhankelijkheid van de Ehrenfesttijd optreedt, namelijk $\delta G \propto \exp(-\tau_E/\tau_\phi)$. Dezelfde toevalsmatrixtheorie kan beide resultaten van de simulaties verklaren: de onafhankelijkheid van τ_E/τ_D en de afhankelijkheid van τ_E/τ_ϕ. Daarom vormt zij een overtuigende theoretische beschrijving van de overgang van quantummechanica naar klassieke mechanica in een chaotisch systeem.

List of publications

- *Momentum noise in a quantum point contact*, A. Tajic, M. Kindermann, and C. W. J. Beenakker, Physical Review B **66**, 241301(R) (2002) [chapter 6].

- *Dynamical model for the quantum-to-classical crossover of shot noise*, J. Tworzydło, A. Tajic, H. Schomerus, and C. W. J. Beenakker, Physical Review B **68**, 115313 (2003) [chapter 2].

- *Quantum-to-classical crossover of mesoscopic conductance fluctuations*, J. Tworzydło, A. Tajic, and C. W. J. Beenakker, Physical Review B **69**, 165318 (2004) [chapter 3].

- *Weak localization of the open kicked rotator*, J. Tworzydło, A. Tajic, and C. W. J. Beenakker, Physical Review B **70**, 205324 (2004) [chapter 4].

- *Exponential sensitivity to dephasing of electrical conduction through a quantum dot*, J. Tworzydło, A. Tajic, H. Schomerus, P. W. Brouwer, and C. W. J. Beenakker, Physical Review Letters **93**, 186806 (2004) [chapter 5].

Curriculum Vitæ

I was born on the 7th of May 1975 in the old city of Tehran in the northern part of Iran. From 1982 to 1994, I did my primary and high school studies. In 1994, after taking the national entrance examination, I started my studies at Sharif University of Technology in Tehran, choosing the 4-year bachelor program in Applied Physics. As a part of my B.Sc. degree, I spent one year in the Laser Research Institute where I designed a CO_2 laser as my graduation project, under the supervision of Dr. A. Amjadi.

Graduating in 1998, I started my Master studies in Theoretical Condensed Matter Physics at Shahid Beheshti University in Tehran. My supervisor was Dr. F. Ebrahimi and the title of my thesis was "*Magnetic Properties of Carbon Nanotubes*". I obtained my Master's degree in 2001.

In October of that year I started my Ph.D. research in the Instituut-Lorentz of the Leiden Institute of Physics, employed by the Foundation for Fundamental Research on Matter (FOM). I did my research in the field of mesoscopic physics, under the supervision of Prof.dr. C.W.J. Beenakker. During this period I attended several national and international schools and conferences: The NATO Advanced Research Workshop on "*Quantum Noise in Mesoscopic Physics*" in Delft, The Netherlands (2002), the WE-Heraeus Seminar on "*Chaos and Quantum Transport* " in Bad Honnef, Germany (2003), and the NATO Advanced Study Institute on "*Nanoscopic Quantum Physics* " in Les Houches, France (2004). I was a teaching assistant for the advanced course on Electromagnetism in the Physics Department of Leiden University.